The Pennsylvania State University
The Graduate School

NONUNIFORM APERTURE SAMPLING AND CENTER FREQUENCY RANDOMIZATION FOR 3-DIMENSIONAL RADAR IMAGING WITH SPARSE APERTURES

A Dissertation in
Electrical Engineering
by
Colin D. Kelly

Submitted in Partial Fulfillment
of the Requirements
for the Degree of

Doctor of Philosophy

May 2024

The dissertation of Colin D. Kelly was reviewed and approved by the following:

Ram M. Narayanan
Professor of Electrical Engineering
Dissertation Advisor
Chair of Committee

Sven G. Bilén
Professor of Engineering Design, Electrical Engineering,
and Aerospace Engineering

Mehdi Kiani
Associate Professor of Electrical Engineering

Soundar Kumara
Allen E. Pearce and Allen M. Pearce Professor of Industrial Engineering

Traian V. Dogaru
DEVCOM Army Research Laboratory
Special Member

Brian R. Phelan
DEVCOM Army Research Laboratory
Special Member

Madhavan Swaminathan
William E. Leonhard Professor of Electrical Engineering
Department Head of Electrical Engineering

Abstract

Two important artifacts present in synthetic aperture radar (SAR) imagery are sidelobes and grating lobes. Sidelobes are present for any scatterer in resolution cells away from the target position due to the finite sampling interval of the target response. Uniform sampling creates well-conditioned sidelobes that can be suppressed by applying tapered windows across aperture and frequency samples. However, irregular sampling can cause sidelobes to become large and randomly patterned, which reduces the effectiveness of tapered windows. Grating lobes are regularly spaced replicas of a scatterer response that occur when uniformly spaced aperture samples have a spacing greater than a quarter of a wavelength.

When using a sparse aperture, either grating lobes or large sidelobes are created due to the increased sampling interval. A sparse, uniformly sampled aperture suffers from grating lobes. However, a sparse aperture with irregular sampling intervals generates large, random sidelobes rather than grating lobes. 3-dimensional (3-D) imagery with reduced sidelobes can be generated by applying the recursive sidelobe minimization (RSM) technique to an image formed using a sparse aperture with irregular sampling intervals. The RSM technique is an apodization method that is used to suppress sidelobes in radar images. However, it cannot remove grating lobes when coupled with a sparse, uniformly sampled aperture.

A method for suppressing the grating lobes associated with a uniformly sampled aperture is presented that applies the methodology of RSM randomization in the frequency domain. By using subbands with randomized center frequency during the RSM technique, grating lobes and sidelobes can both be suppressed.

A systematic subaperture selection method is used to improve the speed of the RSM in practical SAR imaging systems. Both approaches above are validated using computer simulations using both point targets and realistic target models. They are also applied to experimental data collected in a laboratory environment.

Table of Contents

List of Figures **vi**

List of Tables **xii**

List of Symbols **xiii**

List of Abbreviations **xvi**

Acknowledgments **xviii**

Chapter 1
Introduction **1**
1.1 Motivation 1
1.2 Related Works 3
1.3 Dissertation Contributions 7
1.4 Dissertation Overview 8

Chapter 2
Synthetic Aperture Radar **9**
2.1 SAR Configuration and Point Target Response 9
2.1.1 PTR Phase 11
2.2 Point Spread Function 14
2.2.1 Linear Aperture 21
2.2.2 Vertical Grid Aperture 22
2.3 Resolution and Ambiguity 23
2.4 Simulations 25
2.5 Experimentation 40

Chapter 3
Imaging Artifacts and the Recursive Sidelobe Minimization Technique **46**
3.1 Synthetic Aperture Radar Ambiguities 47
3.2 Recursive Sidelobe Minimization 49
3.2.1 RSM Subaperture Selection 52

3.2.2 Monte Carlo Simulation 59
3.3 Model Data 62
3.4 Experimentation 70

Chapter 4
Modified RSM: Center Frequency Randomization **77**
4.1 Point Target Simulations 77
4.2 Modeling 83
4.3 Experimentation 85

Chapter 5
Conclusion and Future Work **93**
5.1 Summary 93
5.2 Future Work 94
5.2.1 Aperture Design 95
5.2.2 Modeling 95
5.2.3 Experimental Data 95
5.2.4 UAV Platform 95
5.2.5 Distributed Radar 96

Appendix A
Derivation of the Range Approximation **98**

Bibliography **100**

List of Figures

2.1 Aperture, image area, and point-target, with angles defined to the aperture center. 10

2.2 Top view of scene showing position vectors referenced to the center of the aperture. 11

2.3 Real and imaginary components of the PTR for a simulated point-target. 12

2.4 Range to a point-target along a linear aperture. 13

2.5 Real and imaginary components of a PTR at a fixed frequency for a simulated point-target. 14

2.6 1-D PSF generated at a single aperture position 16

2.7 a) 3-D ambiguity of a single point and b) the 2-D ambiguity formed in the ground plane. 17

2.8 Diagram demonstrating the combination of data to generate backprojection imagery. 18

2.9 Image with cross-range resolution, but no vertical resolution. 19

2.10 Vertical grid aperture 19

2.11 3-D PSF resulting from the grid aperture. 20

2.12 Grid aperture samples. 23

2.13 Linear and grid apertures and a point-target. 26

2.14 Image of point-target at $(x_ø, y_ø, z_ø) = (-1, 0.5, 1.5)$ m created using a linear aperture with the image formation plane set to (a) $z = 1.5$ m and (b) $z = 0$ m. 27

2.15 Circle of ambiguity around a linear aperture at a fixed cross-range position. 28

2.16 Comparison plots of the simulated and analytic PSFs for the linear aperture in the (a) x and (b) y directions over the target peak. 29

2.17 Image of point-target at $(x_ø, y_ø, z_ø) = (-1, 0.5, 1.5)$ m created using a vertical grid aperture with the image formation plane set to (a) $z = 1.5$ m and (b) $z = 0$ m. 29

2.18 Image in the xz-plane at the cross-range position of a point-target using a vertical grid aperture. 30

2.19 Comparison plots of the simulated and analytic PSFs for the vertical grid aperture in the (a) x-, (b) y-, and (c) z-directions over the target peak. . 31

2.20 Linear aperture and point-target. 32

2.21 Image formed for aperture and point-target in Fig. 2.20. 32

2.22 Image of point-target formed using a linear aperture, annotated with curves containing artifacts of interest. 33

2.23 Undersampled linear aperture. 34

2.24 Image formed using undersampled linear aperture. 35

2.25 Comparison between an analytical and simulated PSF for an undersampled linear aperture in the cross-range direction. 36

2.26 Undersampled grid aperture and a point-target. 38

2.27 3-D image formed using an undersampled grid aperture. 38

2.28 A plot along the y-axis through a point-target. 39

2.29 A plot along the z-axis through a point-target. 39

2.30 a) Scanner at ARL facility capable of both vertical and horizontal scanning. b) Two landmines stacked vertically using styrofoam blocks. 41

2.31 Linear aperture, two landmines, and the image area. 42

2.32 Ground plane image of the test scene using data collected with a linear aperture. 42

2.33 Horizontal slices of 3-D image containing vertically displaced landmines at (a) $z = 0.7$ m and (b) $z = 1.4$ m. 43

2.34 Comparison of imagery in an across-track-vertical slice of the 3-D image at the along track position of the landmine targets between (a) experimental data and (b) modeling data. 44

2.35 3-D image of landmines. 45

3.1 Simulated point target for (a) a zig-zag aperture, (b) an irregularly sampled aperture, and (c) a uniformly sampled aperture. 47

3.2 Simulated PSFs for (a) a zig-zag aperture, (b) an irregularly sampled aperture, and (c) a uniformly sampled aperture. 48

3.3 Images formed using (a) a random subset of a linear aperture, (b) a different random subset of a linear aperture, and (c) the minimum between the two images. 50

3.4 PSFs after 2000 iterations of RSM for a) a zig-zag aperture, b) a random aperture, and c) a periodic aperture. 51

3.5 The MA plotted for the zig-zag aperture, the random aperture, and the periodic aperture. 53

3.6 The PA plotted for the zig-zag aperture, the random aperture, and the periodic aperture. 54

3.7 Ten-element random aperture. 55

3.8 Mean ambiguity plotted for each group of subapertures: (a) subaperture groups 1–5 (b) subaperture groups 6–9. 56

3.9 Peak ambiguity plotted for each group of subapertures: (a) subaperture groups 1–5 (b) subaperture groups 6–9. 57

3.10 Comparison of (a) MA and (b) PA using organized and random subaperture selection in the RSM algorithm. 58

3.11 A grid aperture of potential sample points, a randomly sampled, twenty-element aperture, and a point target. 59

3.12 (a) PA from 50 Monte Carlo simulations with twenty-element apertures. (b) Maximum, mean, and minimum PA for a Monte Carlo simulation using random twenty-element apertures. 61

3.13 Maximum, mean, and minimum PA for a Monte Carlo simulation using random fifteen-element apertures. 62

3.14 (a) Random aperture and (b) periodic aperture with target overlaid. . . . 63

3.15 Image of a short metal cylinder formed using a linear aperture. The target contour is represented by the green circle. 64

3.16 Images using standard SAR imaging with (a) a random aperture and (b) an undersampled periodic aperture. 64

3.17 Images of a metal cylinder in HH polarization after 2000 iterations of RSM generated using (a) a random aperture and (b) a periodic aperture. 65

3.18 Peak artifact plotted at each RSM iteration for the images of a metal cylinder formed using the random and periodic apertures. 66

3.19 B-scan from (a) a random aperture and (b) a periodic aperture. 67

3.20 Two random apertures for comparison. 68

3.21 B-scans of metal cylinder for (a) a narrow random aperture and (b) a wide random aperture. 69

3.22 Image of a metal cylinder formed using (a) a narrow and (b) a wide aperture. 69

3.23 (a) Trihedral on a styrofoam block. (b) Scanning platform with antennas mounted. 70

3.24 Bistatic phase centers from experimental data. 71

3.25 Grid aperture and measured trihedral. 71

3.26 3-D image of a trihedral formed using a grid aperture. 72

3.27 Random narrow aperture. 73

3.28 Image of a trihedral formed using a random aperture and the RSM algorithm. 73

3.29 PA for image formed using random aperture. 74

3.30 Wide random aperture. 74

3.31 Image of trihedral formed using a wide random aperture and the RSM technique. 75

3.32 PA from an image formed using a wide random aperture with the RSM technique. 76

4.1 Center frequency distribution using the new method of frequency selection. 79

4.2 (a) An aperture that satisfies that sampling requirement for removing grating lobes, and (b) an aperture that does not satisfy the sampling requirement for removing grating lobes. 81

4.3 Images formed with the aperture that (a) satisfies the sampling requirement to remove grating lobes and (b) does not satisfy the sampling requirement. 82

4.4 PA comparison between an aperture that satisfies the grating lobe condition and an aperture that does not satisfy the grating lobe condition. . . 83

4.5 Periodic aperture. 84

4.6 Image formed using (a) the RSM technique and (b) the RSM-AFC technique. 84

4.7 PA for images formed using the RSM technique and the RSM-AFC technique. 85

4.8 (a) Trihedral on a styrofoam block. (b) Scanning platform with antennas mounted. 86

4.9 Bistatic phase centers from experimental data. 86

4.10 Received spectrum at a single aperture position. 87

4.11 Periodic aperture and trihedral. 88

4.12 Image of trihedral after RSM-AFC algorithm. 89

4.13 Image of a trihedral after RSM-AFC algorithm with a minimum bandwidth at each iteration. 90

4.14 Undersampled aperture that does not satisfy the sampling conditions for grating lobe removal. 91

4.15 Image of a trihedral after RSM-AFC algorithm for an aperture that does not meet the sampling conditions to remove grating lobes. 92

List of Tables

2.1 Grating lobe position and position error for a simulated undersampled linear aperture. 36

2.2 SCR in imagery created using grid aperture and linear aperture. 37

2.3 SCR in imagery created using grid aperture and linear aperture. 43

List of Symbols

$\arg\{\cdot\}$	phase of the expression between the brackets
A_y	aperture length in the y direction
A_z	aperture length in the z direction
c	speed of light: 3×10^8 m/s
D_x^u	unambiguous image size in the x direction
D_y^u	unambiguous image size in the y direction
D_z^u	unambiguous image size in the z direction
f	frequency (Hz)
f_c	center frequency
f_l	frequency at index l
f_{max}	maximum operating frequency
f_{min}	minimum operating frequency
G_t	gain of transmit antenna
G_r	gain of receive antenna
I_q	intermediary image at recursive sidelobe minimization algorithm iteration q
$\mathrm{Im}(\tilde{\mathbf{r}})$	pixel value at position $\tilde{\mathbf{r}}$
Im_q	recursive sidelobe minimization image at iteration k
k	wavenumber, $k = \frac{2\pi}{\lambda}$
k_c	wavelength at center frequency f_c

k_l	wavenumber at index l
l	frequency sample index
L	number of frequency samples
m	aperture sample index
M	number of aperture samples
n	aperture row index for planar synthetic aperture
N	number of aperture rows in planar synthetic aperture
P_r	received power
P_t	transmitted power
$\mathrm{PTR}(\tilde{\mathbf{r}}_{\o}, \tilde{\mathbf{r}}_{\mathbf{m}}, f_l)$	point target response for a point target for aperture position m and frequency l
q	recursive sidelobe minimization algorithm iteration
Q	total number of recursive sidelobe minimization iterations
r	length of a position vector to a pixel
$\tilde{\mathbf{r}}$	position vector of a pixel
$\tilde{\mathbf{r}}_{\mathbf{m}}$	position vector of aperture sample m
$r_{\o}$	Length of the point target position vector
$\tilde{\mathbf{r}}_{\o}$	position vector of a point target
$\tilde{\mathbf{r}}_{\mathbf{m,n}}$	position vector of aperture sample (m, n) on a planar synthetic aperture
z_n	height of an aperture sample on row n
r_t	range from the target to the transmit antenna
r_r	range from the target to the receive antenna
(x, y, z)	Cartesian pixel coordinates
$(x_{\o}, y_{\o}, z_{\o})$	Cartesian point target coordinates
(x_m, y_m, z_m)	Cartesian position of aperture sample m
$(x_{tri}, y_{tri}, z_{tri})$	Cartesian position of a trihedral
x_a	x position of the aperture center

y_a	y position of the aperture center
z_a	z position of the aperture center
δ_r	Range resolution
δ_x	resolution in the x direction
δ_y	resolution in the y direction
δ_z	resolution in the z direction
Δf	frequency step size
Δy	aperture sample spacing in the y direction
Δz	aperture sample spacing in the z direction
θ	incident angle to a pixel from the aperture center
$\theta_{\o}$	incident angle to the point target from the center of the aperture
Θ	aspect angle from the center of the aperture to a pixel, (θ, ϕ)
λ	wavelength, $\lambda = \frac{c}{f}$
σ	radar cross-section
ϕ	azimuthal angle to a pixel from the aperture center
ϕ_s	imaging squint angle
$\Phi(\tilde{\mathbf{r}}_{\o}, \tilde{\mathbf{r}}_{\mathbf{m}}, f_l)$	Received signal phase of a point target for aperture position m and frequency l
$(\cdot)^*$	complex conjugate
$\frac{\partial \Phi(\tilde{\mathbf{r}}_{\mathbf{o}}, \tilde{\mathbf{r}}_{\mathbf{m}}, f_l)}{\partial f}$	partial derivative of the received signal phase with respect to frequency
$\binom{n}{k}$	binomial coefficient

List of Abbreviations

1-D	One-Dimensional
2-D	Two-Dimensional
3-D	Three-Dimensional
AFDTD	Army Finite-Difference Time-Domain
ARL	Army Research Laboratory
DL-SAR	Down-Looking Synthetic Aperture Radar
FL-SAR	Forward-Looking Synthetic Aperture Radar
GPR	Ground Penetrating Radar
IFP	Image Formation Plane
MA	Mean Artifact
PA	Peak Artifact
PSF	Point Spread Function
PTR	Point Target Response
RCS	Radar Cross Section
RF	Radio Frequency
RSM	Recursive Sidelobe Minimization
RSM-ACF	Recursive Sidelobe Minimization - Aperture and Center Frequency
SAR	Synthetic Aperture Radar
SCR	Signal-to-Clutter Ratio
SL-SAR	Side-Looking Synthetic Aperture Radar

sUAV	Small Unmanned Aerial Vehicle
SWAP	Size, Weight, and Power
UAV	Unmanned Aerial Vehicle

Acknowledgments

I met Dr. Ram Narayanan nine years ago, when I took my first course in electromagnetics. I can still remember him running around the lecture hall, gesticulating wildly and demonstrating electric and magnetic field polarizations with an eraser and a piece of chalk. I was enthralled, and I signed up for his next class the second it was available. Dr. Narayanan brought an enthusiasm to the subject that I didn't know could exist. In my years working in his lab, he has shown me the dedication, consistency, and, most importantly, energy that must go into graduate research. I'm sure that I've given him his fair share of gray hairs, but I'd like to thank Dr. Narayanan immensely for the support, motivation, and laughs over the years.

I would like to thank Dr. Kyle Gallagher for showing me what it means to be an engineer. Kyle brought me into the trenches working with hardware and processing data in the lab and in the field. Kyle has taught me the importance of taking things one step at a time and always asking why. He is a phenomenal mentor and an even better friend. I would also like to thank Dr. Traian Dogaru for the hours of lectures, novels worth of notes, and days of discussion that he has dedicated to making me a better researcher. Dr. Dogaru has helped me wade into the shallow end of theory, and has demonstrated the techniques necessary to start heading toward deeper water. Next, I would like to thank Dr. Brian Phelan for the guidance and support over years working with me at ARL. Dr. Phelan has gone above and beyond in mentoring me and helped me forge a path to where I am going. His friendship and mentorship have been invaluable in my time at ARL. I would also like to thank Dr. Bilén, Dr. Kiani, and Dr. Kumara for serving on my committee, and offering their insights, suggestions, and time to help further my research.

I would like to express gratitude to my coworkers at ARL. I would like to thank Kelly Sherbondy for his guidance both in my research and my life outside of work. I would also like to thank my coworkers at ARL, specifically Ken Ranney, Calvin Le, Lam Nguyen. Their experience and knowledge in the field never cease to amaze me. Khalid Salik has also helped immensely with my work, and I appreciate all that he does. I would also like to thank Dr. Benjamin Kirk and Daniel Galanos for their friendship and support throughout this process.

"GO GO GO!!!" - Dr. Narayanan

Chapter 1 Introduction

1.1 Motivation

Radar technology provides an effective method for detecting the presence of a wide variety of man-made objects, as well as a wealth of information about the natural environment. The contrast in dielectric properties between the target and the surrounding propagation medium creates electromagnetic wave reflections. The strength of these reflections typically increases with the target-medium dielectric contrast. In an active radar system, a waveform is generated in the transmitter, while the receiver measures the signal reflected by the target, which is a delayed and distorted replica of the original waveform. The received signals can be used to find the range, bearing (angle-of-arrival), and radial velocity (related to the Doppler shift) of the target. Since all modern radar systems employ coherent processing, both the phase and magnitude of the returned signals are measured. In particular, the progression of the signal phase over fast- and slow-time, contains important information about the target location and dynamics.

Synthetic aperture radar (SAR) is a method of coherently combining data collected at multiple aperture positions to generate radar imagery of a surveyed scene. In SAR, a radar passes over a scene of interest while collecting data. In unfocused radar data, targets are often recognizable by their hyperbolic response along a linear aperture, but in more challenging detection scenarios the data must be focused. SAR focusing integrates energy coherently at locations containing coherent scatterers and incoherently in regions of distributed clutter. This phenomenon is leveraged to improve the ratio of the peak target power to the average clutter power, or signal-to-clutter ratio (SCR). Imaging creates a reflectivity map of the scene that provides situational awareness of the surrounding environment and an accurate estimate of the target location.

Clutter is an environmental phenomenon that generates its own return that competes with the target response in many cases. Clutter can be caused by discrete scatterers, such as rocks and tree branches, which can have strong coherent responses. These types of scatterers often produce false alarms in radar detection applications, where they are mistakenly identified as a desired target. Clutter also results from distributed surfaces or regions of weaker scatterers, where the response obscures the target signature and presents its own noise-like response. Distributed clutter appears in myriad forms, from foliage for surface target detection to the ground surface in ground penetrating radar applications. One of the ever-present challenges in radar imaging is target detection despite strong clutter interference.

This dissertation aims to contribute to the enhancement of technology employed in humanitarian demining, focusing on the detection of explosive ordnances such as mines, explosive remnants of war, and improvised explosive devices. According to data from the United Nations in 2022, there were 9,198 casualties attributed to explosive ordnances, disproportionately impacting civilians [1]. The global community is actively engaged in detecting and removing these threats in both past and current conflict zones.

SAR emerges as a valuable tool for scanning extensive areas to identify potential explosive targets. However, the efficacy of SAR is hindered by challenges posed by distributed clutter and competing interference, creating obstacles in target detection. This dissertation proposes methodologies to enhance target detection in the presence of distributed clutter.

SAR systems have been employed in a wide variety of modalities, each optimized for a specific application. Down-looking radar is used for ground penetrating radar (GPR) because it effectively couples energy into the ground. On ground-based vehicles, these systems generally consist of bumper-mounted arrays [2–5]. Forward-looking systems can also be used for GPR applications [6–13]. This modality sacrifices the coupling of energy into the ground for stand-off from its search area. Side-looking radar is used in a variety of remote sensing applications. Side-looking systems are typically mounted on large aerial platforms to scan wide areas searching for surface targets or shallow buried targets [14–17].

Experimental demonstrations have confirmed the efficacy of low-frequency signals in effectively penetrating dielectric media that are opaque to frequencies in the visual spectrum [18, 19]. The systems in this domain have primarily functioned within the frequency band spanning from 200 MHz to 4000 MHz. The utilization of low frequencies has proven instrumental in facilitating target detection through obscuration, complemented by ultra-wide bandwidths that contribute to enhanced resolution. Notably, the size of radio frequency (RF) components and antennas exhibits an inverse relationship with the operating frequency. Therefore, such systems are better suited for mounting on larger platforms.

The newest radio frequency electronics componentry has allowed for the reduction in system size, weight, and power (SWAP) of radar systems, which has enabled the use of small unmanned aerial vehicle (sUAV) platforms. Both side-looking and down-looking modalities can be used, and switching modalities can be achieved by a change in antenna orientation. The sUAV platform provides an advantage over ground-based and fixed-wing platforms due to its maneuverability. The ability to implement unconventional flight paths, including circular and 2-dimensional (2-D) raster scans, enables three-dimensional (3-D) image formation. Some UAV mounted systems described in the literature are designed to detect buried targets using a down-looking configuration, [20–22] while others are configured as side-looking systems for surface target detection [23, 24]. To date, the mobility of sUAVs has not been leveraged to fly custom flight paths to generate 3-D imagery. This dissertation explores the design of apertures enabled by the new era of sUAV-based SAR systems.

The operation of sUAV platforms imposes constraints on SWAP, which, in turn, limits the operational frequencies of these systems. In the context of the systems discussed in the preceding paragraph, their frequency range extended from 500 to 4600 MHz. For applications requiring penetration of lossy media, lower radar frequencies, from 300 to 500 MHz, could increase the system's effectiveness. However, due to their limited SWAP capabilities, sUAV-mounted systems do not typically operate below 500 MHz. This limitation somewhat reduces these sensor's effectiveness in detecting obscured targets. In the case of the system examined in this dissertation, which is designed to detect targets placed above the ground, the operational frequencies range from 2.2 to 3.7 GHz. This sacrifice in penetrative capabilities is compensated by achieving improved imaging resolution

1.2 Related Works

In most radar imaging applications, the goal is to detect a target obscured by clutter. Traditionally, radar imagery is formed in two dimensions using a linear aperture. However, there are many shortcomings associated with 2-D imaging. In Reference [25], different radar modalities are compared for target detection in ground-penetrating radar. A calibrated point target response is compared with clutter generated by rough ground surface and soil permittivity fluctuation. Target-to-clutter ratio (TCR) is evaluated as a function of depth, with a 2-D down-looking planar aperture greatly outperforming down-looking and side-looking linear apertures for targets buried deeper than 0.1 m. One major advantage of a 3-D imaging system is the fact that each scatterer is imaged at its true location in the 3-D space. By contrast, 2-D imaging systems are typically affected by the projection of out-of-plane scatterer responses into the image plane, due to the lack of resolution in the third dimension. Furthermore, in a 3-D image, distributed clutter is separated into more resolution cells, lowering the average clutter power in each cell. This principle equally applies to different modalities and, in this dissertation, it is demonstrated in a near-field, side-looking geometry.

To generate 3-D imagery, a 2-D planar aperture must be used. In side-looking SAR this can be accomplished using either a vertical, real aperture scanning along a horizontal linear track, or a quasi-monostatic system sampling on a 2-D uniform grid [26]. A vertical linear aperture implemented as an antenna array requires a complex radar architecture to operate on multiple channels simultaneously. This configuration would be susceptible to self-interference, and would require a high SWAP, unsuited for sUAV platforms at S- and L-band frequencies. This dissertation is concerned with quasi-monostatic radar systems, where a transmit and receive antenna are co-located on the same platform. This configuration would require a large amount of time to sample the aperture space at a sufficiently fine rate in each dimension. Completion of data collections over useful imaging areas would place a heavy strain on UAV battery life and would be difficult to implement in practice. Sparse apertures are investigated as a potential solution to the challenging quasi-monostatic case.

Publications from the field of radio astronomy provide valuable insight into the techniques presented in this dissertation. In radio astronomy extremely large arrays are used to yield the narrow beamwidths necessary to resolve various cosmic electromagnetic sources [27]. To avoid large secondary lobes the arrays must be sampled at less than one-half wavelength separation. Many elements are required to satisfy this sampling constraint, which makes these arrays extremely costly. Furthermore, element spacings less than one-half wavelength are impractical due to increased coupling between elements [28]. Research sought to reduce the number of necessary elements without reducing the performance of the arrays. One method of reducing elements is to increase the spacing between uniformly spaced elements; however, this introduces large secondary beams into the array pattern, called grating lobes. One method of reducing sidelobes applied an amplitude taper across the array, but this required a complicated feed system and increased the mainlobe width [29]. It was found in Reference [30] that arrays with arbitrarily distributed elements have more degrees of freedom than arrays with equally spaced elements, implying that they require fewer elements and have lower sidelobes than arrays with equally spaced elements.

The research that followed used different methods of investigating and synthesizing nonuniformly distributed arrays to suppress sidelobes and grating lobes without greatly affecting the mainlobe width. Reference [31] provides preliminary calculations for several arrays of unequally spaced elements and computes universal pattern factors for different sets of spacings. In this study, it was noted that certain patterns had sidelobes below those for uniform arrays, implying that nonuniform element spacing can be used to reduce sidelobes. Reference [29] presented a perturbation method that reduced the sidelobes of an array with constant excitations. It was shown that this technique had no effect on the beamwidth. However, this technique was only effective when the average element spacing was less than one-half of a wavelength. In Reference [27], nonuniform arrays were used to design a large 2-D array with reduced elements. In this study, it was shown that nonuniform element spacing eliminates grating lobes. It was found that the average minor lobe level increased as the observation angle increased. It was also confirmed that nonuniform sampling reduced the sidelobe level beyond that of a uniformly spaced array. Reference [28] showed that for moderate sidelobe levels, nonuniform arrays can be designed using many fewer elements than Dolph-Chebyshev arrays for the same beamwidth and sidelobe levels. It presented a lower limit to the sidelobe level, which depends primarily on the number of elements. This paper confirmed that grating lobes can be suppressed by suitably arranging an arbitrary set of elements. Furthermore, it was shown that, for a nonuniform array, the 3-dB beamwidth is primarily determined by the aperture length, as in the case of a uniformly distributed array. Reference [32] first developed a theory which made it possible to express the radiation pattern as an analytical expression using Poisson's sum formula. This theory is used to predict the behavior of sidelobes and yield a method of designing an array to produce a desired beamwidth and sidelobe level with a reduced number of elements [33].

Reference [34] took a probabilistic approach to characterize antenna arrays with elements placed at random according to a given distribution. It was found that the pattern was independent of the distribution function for all investigated cases, and it was shown that the probability of the sidelobes exceeding a certain level is the same at all angles. For a given probability, the required number of elements is directly related to the sidelobe level. In the probabilistic sense, the sidelobes are all equal and the pattern is analogous to the Dolph-Chebyshev array with uniformly spaced elements. This mirrors the result in Reference [28]. This work treated probabilistic array patterns; however, it was shown that individual realizations could have both higher and lower sidelobe levels through a systematic design procedure. Reference [35] demonstrated that for uniformly excited elements, the envelope of the grating lobes is flat if the element spacing increases exponentially. Although the presented arrays were optimized to have flat grating lobes, their main lobes were comparable to that of a uniformly spaced array of the same length.

The results from these publications have important implications in radar imaging. Nonuniform sampling in antenna arrays has been used to effectively reduce grating lobes from antenna patterns. Another critical result from these studies on nonuniform array sampling is that the antenna pattern main beam width is preserved. Array pattern main beam width is realized in radar imaging as resolution. These two principles are analogous, as both are tied to the length of the antenna aperture. This implies that nonuniform array distributions can be used without sacrificing resolution in the resulting images. This will be demonstrated in this dissertation as well.

Nonuniform sampling is detrimental to radar imaging because it leads to increased sidelobes. In the case of randomly distributed elements, the sidelobe power is increased throughout the image. The recursive sidelobe minimization (RSM) algorithm, which was developed to reduce multiplicative noise in radar imagery, is applied in this dissertation [36]. This algorithm has been implemented for both forward-looking and side-looking SAR modalities. The synchronous impulse reconstruction radar [12], for which the RSM algorithm was originally designed, had relatively narrow observation angles. However, in circular SAR targets are observed from a wide variety of angles. Reference [37] modified the RSM to be more robust over a wide set of observation angles. The targets were assumed to be anisotropic, so the application of the RSM algorithm over a circular aperture resulted in a loss of scattering center information. An aperture selection method was presented to avoid the loss of this information. Also, the aperture selection method was modified to prevent the use of redundant aperture samples. The consideration for the loss of scattering center information is important for observing targets over wide angles. In this dissertation, the modeled and experimental targets have similar responses to point targets, so the impact of using wide angles is less pronounced. Narrow apertures are used, as well, so that information is not lost.

One should note that similar objectives of creating SAR images with sparsely sampled radar data have been tackled using entirely different approaches under the category of sparse reconstruction methods, which are part of the compressive sensing area of research and have been under investigation for the last decade [38]. The methodology employed in sparse reconstruction algorithms is entirely different from the one presented in this dissertation, and a direct comparison in performance between the two would not be meaningful. The image reconstruction techniques used in this dissertation are based on the classical matched filter theory, coupled with the RSM apodization scheme.

1.3 Dissertation Contributions

Sidelobes and grating lobes represent two types of SAR imaging artifacts that are part of the wider category of multiplicative noise [39]. Any scatterer produces sidelobes in resolution cells positioned away from its physical location, due to finite sampling extent. When the aperture is sampled uniformly, these sidelobes are predictable and can be mitigated by applying a tapered amplitude window across the aperture samples. However, when the aperture is sampled at irregular intervals, the sidelobe spatial distribution is random and can have very large peaks.

Grating lobes are replicas of a scatterer response that occur in the image at regular intervals away from the scatterer's physical location. They are typically a result of regularly sampled apertures when the sampling interval exceeds a quarter of a wavelength for monostatic radar systems. Eliminating the grating lobes with uniformly sampled apertures imposes very stringent limits on the radar parameters. However, it is shown that the aperture sampling rates can be reduced without introducing grating lobes if the samples are collected at irregular intervals.

Based on the discussion in the previous paragraphs, the following challenge emerges: design a SAR system that utilizes sparse aperture samples, while avoiding both large sidelobes and grating lobes. To solve this problem, one can use a sparse, irregularly sampled aperture, coupled with the recursive sidelobe minimization (RSM) technique, which is an apodization method for sidelobe reduction in radar images [36]. One should note that the RSM technique by itself does not remove the grating lobes when applied to a uniformly sampled aperture; however, as shown herein, when RSM is combined with an irregularly sampled aperture, it can effectively suppress both types of image artifacts.

Another approach to sidelobe and grating lobe suppression considers uniform, undersampled apertures and applies the RSM methodology in the frequency dimension of the radar data. By processing the data in sub-bands with randomly selected center frequencies at each RSM iteration, one can again achieve the simultaneous reduction in both types of image artifacts.

Both approaches considered in this dissertation are analyzed in a quantitative, systematic manner, with the goal to formulate the most efficient way to apply them to practical SAR imaging systems. The approaches are also validated using computer simulations that employ both point targets and realistic target models, as well as experimental data collected in a laboratory setting.

1.4 Dissertation Overview

Chapter 2 is focused on general SAR. The near-field, side-looking SAR problem is introduced, and a simplified point target response (PTR) is presented. The point spread function (PSF) is derived for a linear and vertical 2-D grid aperture using the matched-filter algorithm. Then, the principles of resolution and ambiguity are presented. Simulations are used to validate the use of a generalized analytical PSF in the near-field. Experimental data demonstrate the value of 3-D resolution in clutter reduction.

In Chapter 3, a set of sparse apertures and their simulated PSFs are presented. The RSM algorithm is introduced and it is shown that the RSM technique can be paired with a random aperture to generate ambiguity-free imagery. A systematic method of subaperture selection is applied to the RSM algorithm to improve convergence speed. Model data and experimental data are used to demonstrate the use of this technique in practical scenarios.

Chapter 4 presents a modification to the RSM algorithm that removes both grating lobes and sidelobes in imaging scenarios involving uniformly and sparsely sampled apertures. A condition on the SAR parameters for grating lobe removal is derived. Both the algorithm and the necessary condition for grating lobe removal are validated with simulated, modeled, and experimental data.

Chapter 5 provides concluding remarks and discusses future work.

Chapter 2
Synthetic Aperture Radar

2.1 SAR Configuration and Point Target Response

The analysis in this chapter assumes a radar system that operates using a stepped-frequency waveform. In this approach, sinusoidal signals are transmitted at discrete frequencies f_l ranging from $f_c - \frac{B}{2}$ to $f_c + \frac{B}{2}$ (where B is the system's bandwidth and f_c is the center frequency), in Δf increments, and phase and magnitude information from the scattered signals is collected at each frequency step. To obtain a 2-D or 3-D radar image, the radar transmitter and receiver are moved across a synthetic aperture and the frequency stepping procedure is repeated at each sampling position along the aperture. A monostatic configuration is considered in this chapter, with propagation taking place in free-space. The coordinate system is chosen such that the image is centered at the origin, while the radar is placed at some range from the origin, as shown in Fig. 2.1.

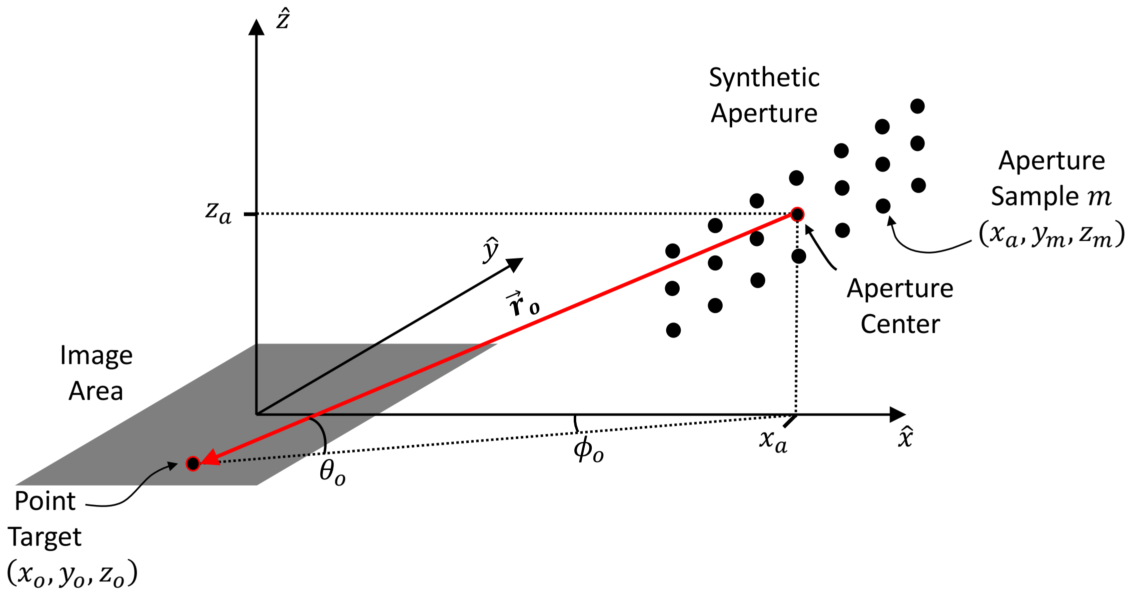

Figure 2.1. Aperture, image area, and point-target, with angles defined to the aperture center.

The SAR system considered here operates with a fixed aperture length and all aperture samples are used in focusing each image pixel/voxel, similar to a SAR system operating in spotlight mode. This is different from strip-map operation, where only a portion of the synthetic aperture is used in the image formation of each pixel/voxel.

Position vectors are referenced to the center of the aperture, as shown in Fig. 2.2. A point-target at the Cartesian position $(x_{\o}, y_{\o}, z_{\o})$ is characterized by the position vector $\vec{\boldsymbol{r}}_{\o} = \begin{bmatrix} x_{\o} - x_a & y_{\o} & z_{\o} - z_a \end{bmatrix}^T$. Furthermore, the length of $\vec{\boldsymbol{r}}_{\o}$ is denoted by $r_{\o} = |\vec{\boldsymbol{r}}_{\o}|$.

The complex voltage signal received by the radar at aperture sample $\vec{\boldsymbol{r}}_m = \begin{bmatrix} 0 & y_m & z_m - z_a \end{bmatrix}^T$ and frequency f_l depends on the transmit and receive antenna gains, the target scattering characteristics, and the radar-target propagation path [39]. Accounting for all of these factors requires knowledge of each factor, and modeling them requires full-wave, computationally-intensive electromagnetic-wave solvers. It is assumed that the antennas have frequency-independent gains and omnidirectional patterns within the SAR system's integration angle. The wavelength factor relating effective area and gain is ignored as well. It is also assumed that the scattering from the point-target is frequency- and angle-independent. Finally, path loss is ignored.

These simplifications result in the following expression for the point target response (PTR):

$$\text{PTR}(\vec{\boldsymbol{r}}_\o, \vec{\boldsymbol{r}}_{\boldsymbol{m}}, f_l) = A \exp\left(-j2k_l|\vec{\boldsymbol{r}}_\o - \vec{\boldsymbol{r}}_{\boldsymbol{m}}|\right), \tag{2.1}$$

where $k_l = \frac{2\pi f_l}{c}$ is the wavenumber characterizing the radar wave propagation and A is a constant amplitude factor.

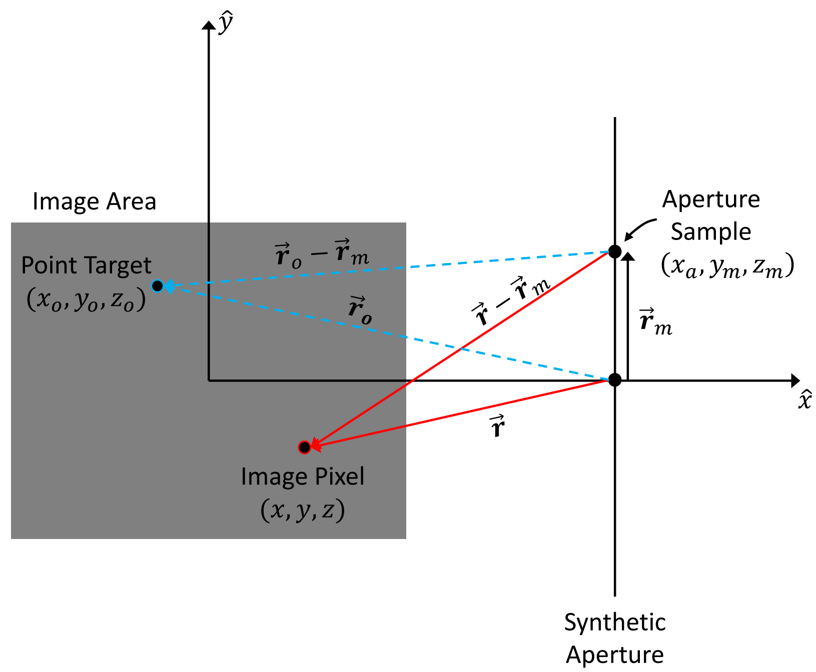

Figure 2.2. Top view of scene showing position vectors referenced to the center of the aperture.

2.1.1 PTR Phase

The PTR in Eq. (2.1) represents the received signal at aperture position m using frequency l. A single aperture position and a single frequency yields a single phase value. These parameters take a range of values throughout this chapter, and simulations are used to demonstrate their effects.

A point-target is simulated at the origin. The SAR parameters are derived from an experimental testbed introduced in Section 2.5. The radar testbed operates over the band from 2.2 to 3.7 GHz, with a 1.5-MHz sampling step size. The aperture center is fixed at the point $\vec{\boldsymbol{r}}_{\boldsymbol{m}} = \begin{bmatrix} 4 & 0 & 2 \end{bmatrix}^{\mathrm{T}}$ m. Since the aperture position is fixed, $|\vec{\boldsymbol{r}}_\o - \vec{\boldsymbol{r}}_{\boldsymbol{m}}|$ is a constant. The phase of the received signal, $\Phi(\vec{\boldsymbol{r}}_\o, \vec{\boldsymbol{r}}_{\boldsymbol{m}}, f_l)$, linearly increases with frequency. Taking the derivative of the phase function yields the slope:

$$\frac{\partial \Phi}{\partial f} = \frac{4\pi}{c}|\vec{\boldsymbol{r}}_{\o} - \vec{\boldsymbol{r}}_{\boldsymbol{m}}|. \tag{2.2}$$

The slope of the PTR is a function of the range to the target. The received signal is a sinusoid whose frequency increases with the range to the target. A PTR is simulated using the point-target described above and a frequency band from 2.2 GHz to 2.6 GHz. The signal is oversampled so that the shape of the sinusoid is clear to the reader. The simulated PTR is plotted with respect to frequency in Fig. 2.3. As the range (slope of the phase in Eq. (2.2)) increases, the frequency of the sinusoid increases.

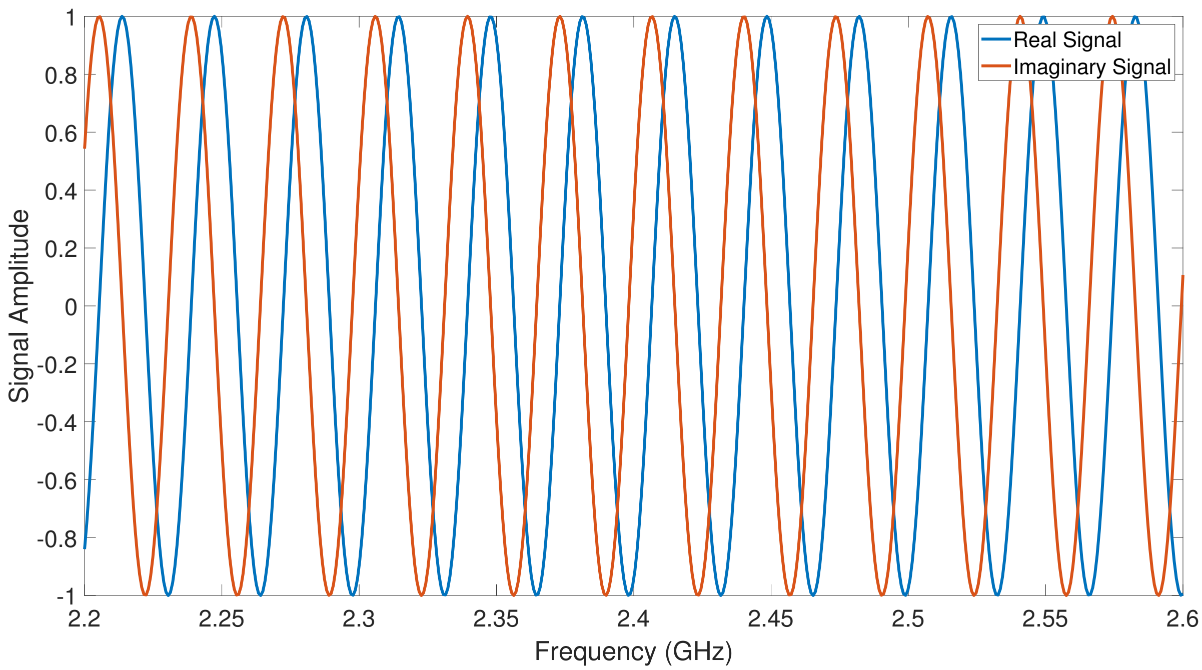

Figure 2.3. Real and imaginary components of the PTR for a simulated point-target.

In traditional stripmap SAR, the platform moves along a linear path past a scene of interest. For a fixed frequency, the phase of the received signal is proportional to the range from the radar to the target. This is demonstrated in the following simulation. A linear flight path at a height of $z = 2$ m and with length $D_y = 5$ m is considered. The range from each aperture position to the point-target is plotted in Fig. 2.4. As aperture position is changed linearly, the range changes approximately quadratically, with a minimum occurring at the cross-range position of the target.

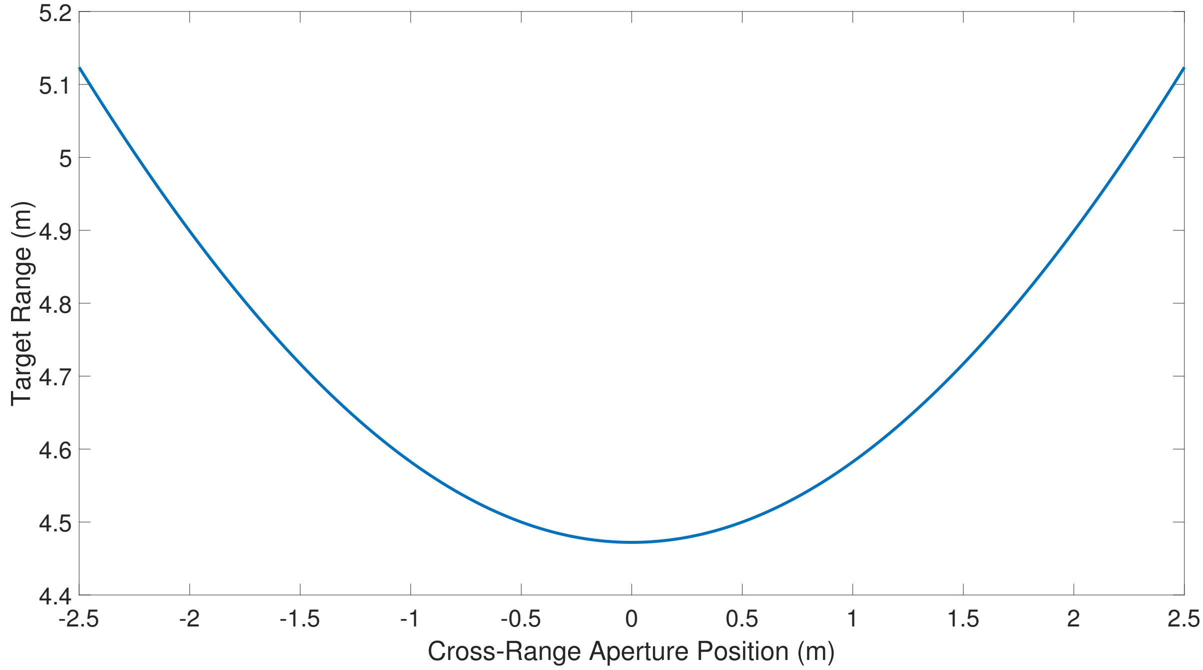

Figure 2.4. Range to a point-target along a linear aperture.

The real and imaginary components of the PTR are plotted with $f_l = 3$ GHz in Fig. 2.5. As frequency increases, the rate of oscillation increases. The rate of these oscillations determines how quickly a target response becomes incoherent at pixels other than the target pixel. This is the principle underlying cross-range resolution and cross-range ambiguity.

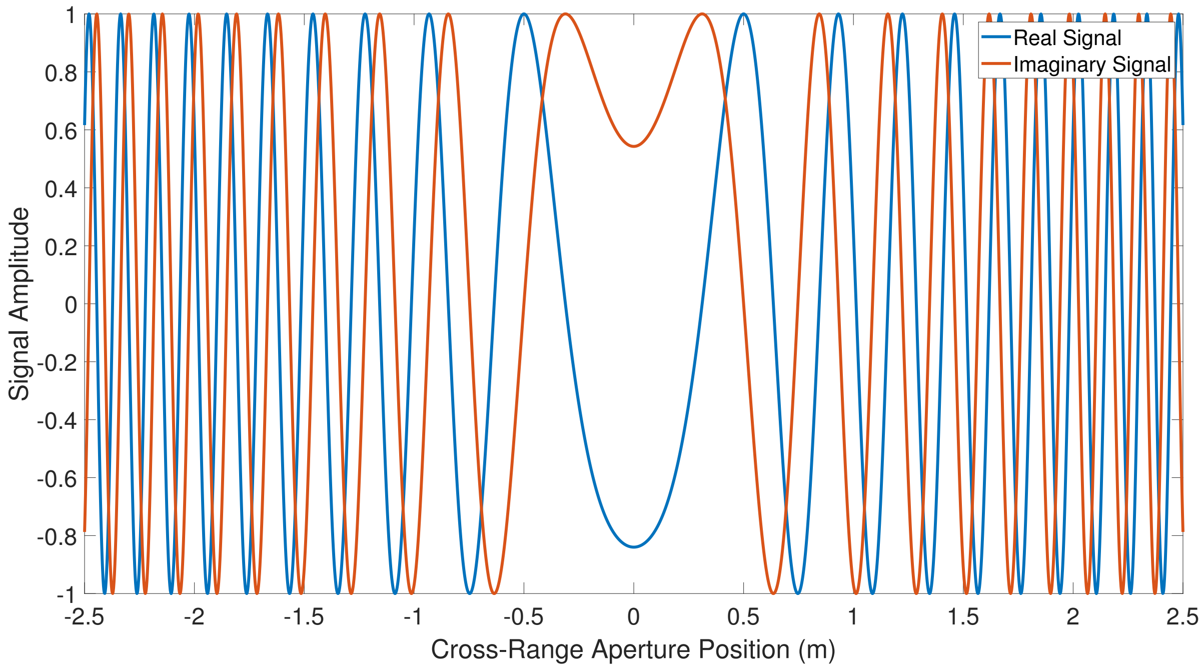

Figure 2.5. Real and imaginary components of a PTR at a fixed frequency for a simulated point-target.

2.2 Point Spread Function

The imaging process maps reflectivity values to pixel/voxel locations. Data are collected in the frequency domain at a single aperture position m, creating a point-target response whose phase slope is a function of the range to the target. The frequency samples are collected at $f_l = f_c + l\Delta f$ where $l = -\frac{L}{2}, ..., \frac{L}{2} - 1$. Since the signal is sampled in the frequency domain, an inverse discrete Fourier transform (IDFT) is used to compute the time-domain response of the point-target, also known as the point spread function (PSF). An P-point IDFT operation is given by [40],

$$x(p) = \frac{1}{L} \sum_{l=-\frac{L}{2}}^{\frac{L}{2}-1} X(k) \exp\left(j2\pi \frac{kp}{P}\right), \tag{2.3}$$

where $x(p)$ is the time-indexed variable with index $p = \frac{P}{2} - 1, ..., \frac{P}{2} - 1$, $X(l)$ is the frequency indexed variable with index $l = -\frac{L}{2}, ..., \frac{L}{2} - 1$, and $L \leq P$. The frequency domain is incremented by Δf and the range domain is incremented by Δr. The size of the DFT is related to the incrementing variables by $P = \frac{c}{2\Delta f \Delta r}$. Substituting for P, the following analysis determines the PSF. Throughout the analysis, constant phase terms are removed.

$$
\begin{aligned}
\mathrm{PSF}(p) &= \frac{1}{L}\sum_{l=-\frac{L}{2}}^{\frac{L}{2}-1} \mathrm{PTR}(\vec{\boldsymbol{r}}_{\o}, \vec{\boldsymbol{r}}_{\boldsymbol{m}}, l)\exp\left(j2\pi\frac{2l\Delta f p\Delta r}{c}\right) \\
&= \frac{1}{L}\sum_{l=-\frac{L}{2}}^{\frac{L}{2}-1} \exp\left(-j\frac{2\pi(f_c+l\Delta f)}{c}2|\vec{\boldsymbol{r}}_{\o}-\vec{\boldsymbol{r}}_{\boldsymbol{m}}|\right)\exp\left(j2\pi\frac{2l\Delta f p\Delta r}{c}\right) \\
&= \frac{1}{L}\sum_{l=-\frac{L}{2}}^{\frac{L}{2}-1} \exp\left(-j\frac{4\pi l\Delta f}{c}|\vec{\boldsymbol{r}}_{\o}-\vec{\boldsymbol{r}}_{\boldsymbol{m}}|\right)\exp\left(j4\pi\frac{l\Delta f p\Delta r}{c}\right) \\
&= \frac{1}{L}\sum_{l=-\frac{L}{2}}^{\frac{L}{2}-1} \exp\left(j\frac{4\pi l\Delta f}{c}\left(p\Delta r-|\vec{\boldsymbol{r}}_{\o}-\vec{\boldsymbol{r}}_{\boldsymbol{m}}|\right)\right) \\
&= \frac{\sin\left(\frac{2\pi L\Delta f\Delta r}{c}\left(p-\frac{|\vec{\boldsymbol{r}}_{\o}-\vec{\boldsymbol{r}}_{\boldsymbol{m}}|}{\Delta r}\right)\right)}{L\sin\left(\frac{2\pi\Delta f\Delta r}{c}\left(p-\frac{|\vec{\boldsymbol{r}}_{\o}-\vec{\boldsymbol{r}}_{\boldsymbol{m}}|}{\Delta r}\right)\right)}.
\end{aligned}
\tag{2.4}
$$

The final step in Eq. (2.4) is performed using the geometric series formula:

$$
\sum_{p=-\frac{P}{2}}^{\frac{P}{2}-1} \exp\left(jpu\right) = \exp\left(-j\frac{u(P-1)}{2}\right)\frac{\sin\left(\frac{uP}{2}\right)}{P\sin\left(\frac{u}{2}\right)}. \tag{2.5}
$$

The resulting PSF is an aliased sinc function [39]. An example is simulated in Fig. 2.6, using a frequency band from 2.2 to 3.7 GHz with a 5–MHz frequency step size. The PSF is plotted with respect to the range vector, $r_p = p\Delta r$, for $p = 0, ..., P-1$. The range of the target is 4.472 m.

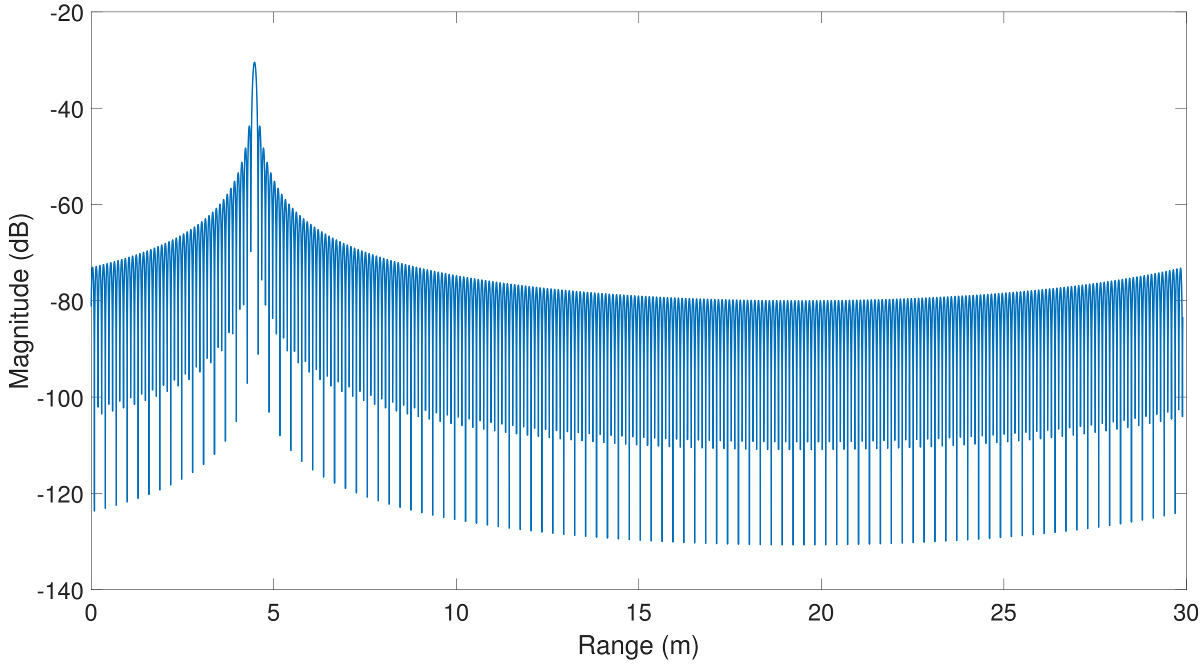

Figure 2.6. 1-D PSF generated at a single aperture position

An important property for an imaging radar is its resolution, which is the ability to separate closely spaced targets. According to the Rayleigh Criterion, the resolution of the signal is given by half the mainlobe width [39]. The radial resolution, or range resolution, is found by setting the numerator of the digital sinc equal to zero. Equivalently, this is found by setting the argument of the sine function in the numerator equal to π. The resolution is solved as

$$\begin{aligned} \frac{2\pi L\Delta f\Delta r}{c}\left(p-\frac{|\vec{\boldsymbol{r}}_{\o}-\vec{\boldsymbol{r}}_{\boldsymbol{m}}|}{\Delta r}\right)&=\pi\\ \frac{2B}{c}\left(p\Delta r-\frac{|\vec{\boldsymbol{r}}_{\o}-\vec{\boldsymbol{r}}_{\boldsymbol{m}}|}{\Delta r}\right)&=1\\ \frac{2B}{c}\left(r_p-|\vec{\boldsymbol{r}}_{\o}-\vec{\boldsymbol{r}}_{\boldsymbol{m}}|\right)&=1\\ \delta_r&=\frac{c}{2B}, \end{aligned} \tag{2.6}$$

where $B = L\Delta f$ is the bandwidth of the signal, $r_p = p\Delta r$ is the range vector, and $\delta_r = r_p - |\vec{\boldsymbol{r}}_{\o} - \vec{\boldsymbol{r}}_{\boldsymbol{m}}|$ is the change in range. The resolution for the PSF above is 0.1 m.

Resolution is determined by the mainlobe width of the time-domain signal. At a single aperture position, only the range to the observed target can be determined; no other position information is available. From a 3-D imaging perspective, the target response is a sphere of radius $|\vec{\boldsymbol{r}}_{\o} - \vec{\boldsymbol{r}}_{\boldsymbol{m}}|$ centered around the aperture position. This is simulated for the single-point aperture case, with a frequency band from 2.2 to 3.7 GHz. The resulting 3-D image is shown in Fig. 2.7. The ambiguity sphere is centered around the aperture, and intersects the target's position at the origin. A 2-D image is formed by the intersection of the ambiguity sphere with the image formation plane (IFP) [41]. In this case, the IFP is the ground plane. The response in the ground plane is a circle, centered in x and y around the center of the aperture.

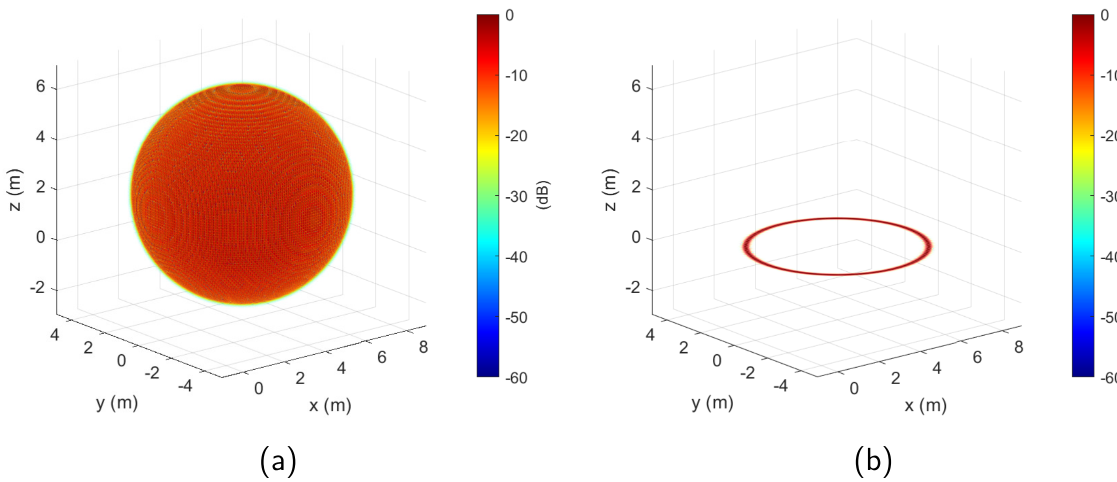

Figure 2.7. a) 3-D ambiguity of a single point and b) the 2-D ambiguity formed in the ground plane.

A pixel at the cartesion position (x, y, z) is characterized by the position vector $\vec{\boldsymbol{r}} = \begin{bmatrix} x - x_a & y & z - z_a \end{bmatrix}^{\mathrm{T}}$. The range from aperture sample m to the pixel at $\vec{\boldsymbol{r}}$ is given by $|\vec{\boldsymbol{r}} - \vec{\boldsymbol{r}}_{\boldsymbol{m}}|$. Next, the index, p, that yields $\min\limits_{p} r_p - |\vec{\boldsymbol{r}} - \vec{\boldsymbol{r}}_{\boldsymbol{m}}|$ is found. The value of the pixel at $\vec{\boldsymbol{r}}_{\o}$ is the complex value of the range profile at index p. This process is repeated for each pixel within the imaged area. The value of the pixel at $\vec{\boldsymbol{r}}$ using aperture position m is $I_m(\vec{\boldsymbol{r}}) = \mathrm{PSF}_r(p)$. This is repeated at each aperture position, and the resulting images are summed to generate the final complex image. This process is known as time-domain backprojection or the delay-and-sum algorithm.

Backprojection is simulated below. An aperture of 333 elements with a separation of 0.006 m is used. The total aperture length D_y is 2 m. The target is at the origin, and the frequency band from 2.2 to 3.7 GHz is used. The frequency step size is 5 MHz. At each aperture position below, there is a circle of ambiguity centered around the aperture element. Each of the circles contains the origin at its peak, but the radius of the circle changes as the range from the aperture element to the target changes. This causes energy to add coherently at the origin and destructively interfere at other points. This is demonstrated in Fig. 2.8 The target response is resolved along the circle around the center of the aperture. Energy also focuses at a mirrored point on the other side of the aperture. In practice, antennas are directional and imagery is only formed close to the antenna line-of-sight, so this ambiguity can be ignored.

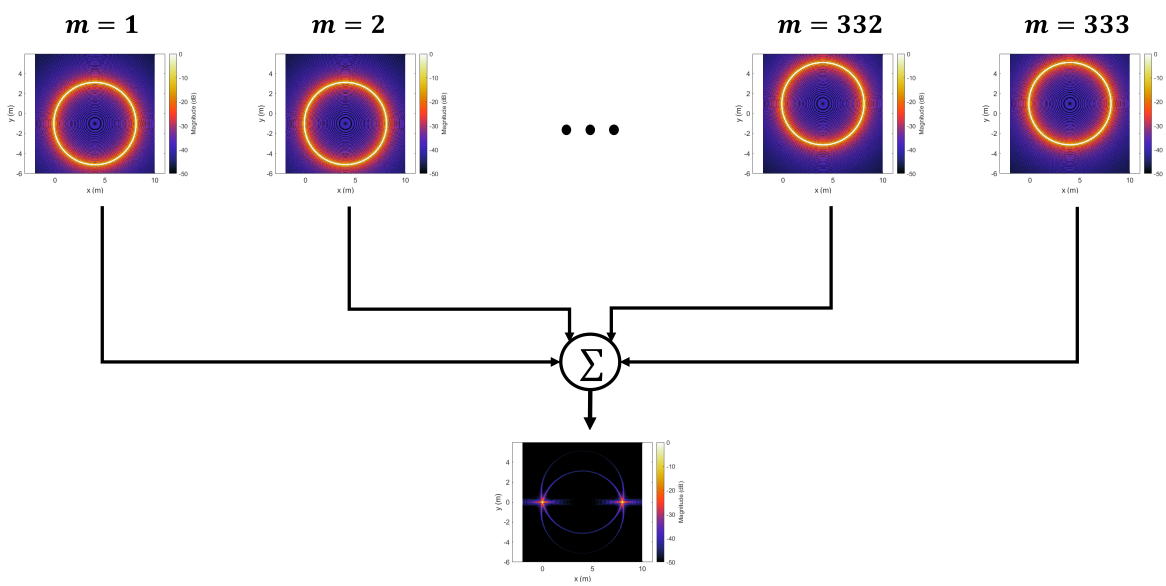

Figure 2.8. Diagram demonstrating the combination of data to generate backprojection imagery.

As shown in Fig. 2.8, adding aperture elements in the horizontal direction resolves the image in the azimuthal direction. The aperture domain can be considered as the inverse of the image domain, so a wide aperture results in narrow resolution. The aperture above provides no vertical resolution because it has no vertical extent. The 3-D image resulting from the above aperture is shown in Fig. 2.9. The resulting ambiguity is a ring of radius, $\left|\vec{\boldsymbol{r}}_{\varnothing} - \begin{bmatrix}0 & y_{\varnothing} & 0\end{bmatrix}^{\mathrm{T}}\right|$ centered around the aperture at the cross-range position of the target. The strongest 20 dB of the response is plotted.

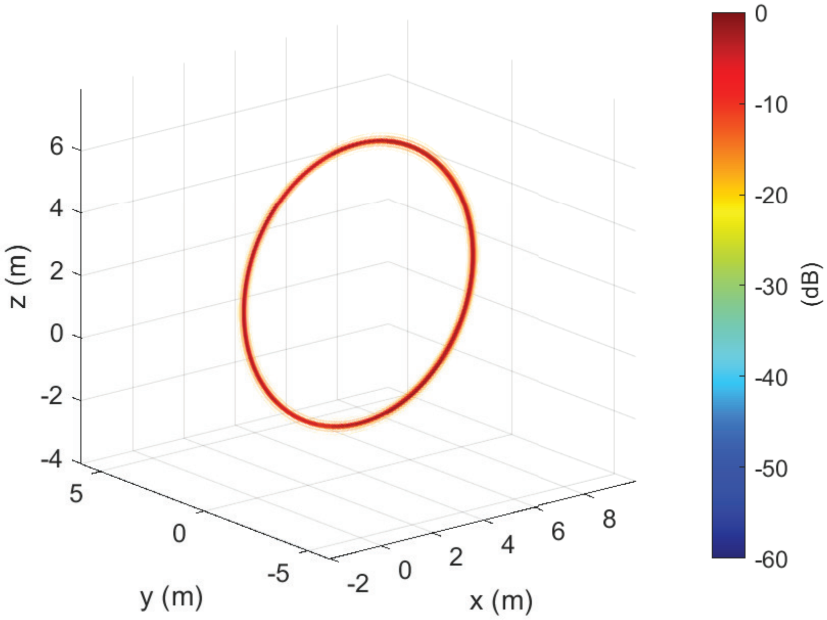

Figure 2.9. Image with cross-range resolution, but no vertical resolution.

Next, a grid of 2-D aperture points is simulated to show the resulting vertical resolution. The aperture is a square grid, shown in Fig. 2.10, with 0.05-m spacing in both the horizontal and vertical directions.

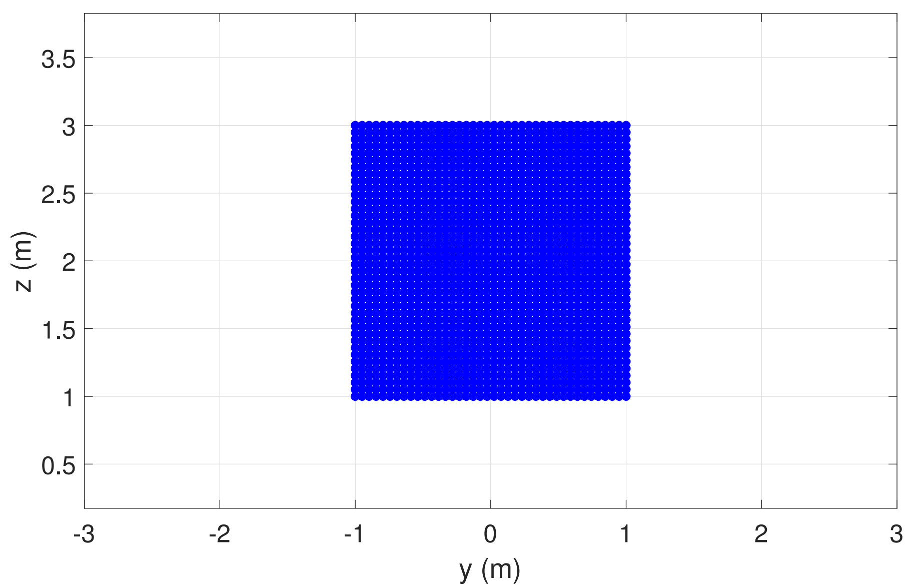

Figure 2.10. Vertical grid aperture

The resulting PSF is shown in Figure. 2.11. The added vertical dimension on the aperture results in vertical resolution.

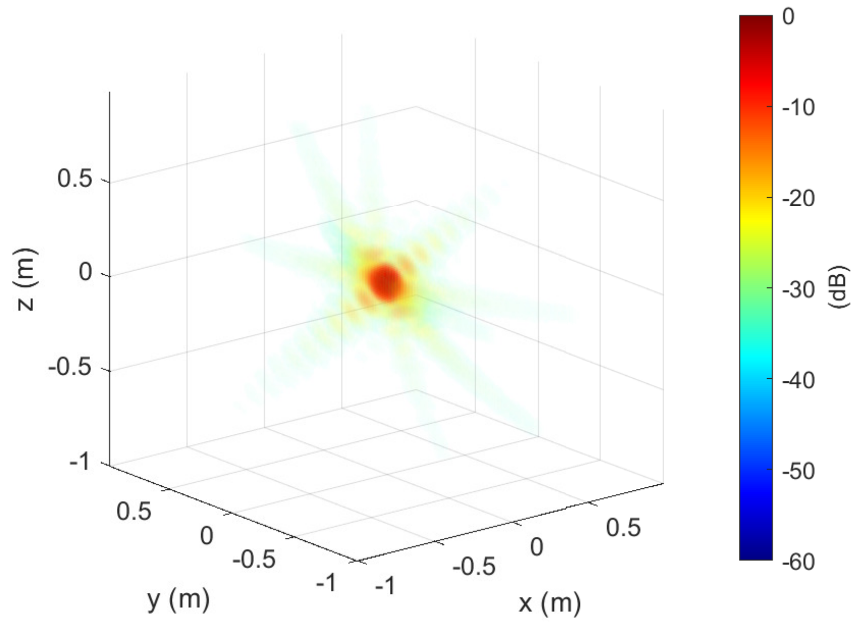

Figure 2.11. 3-D PSF resulting from the grid aperture.

Closed-form analytic expressions for the PSF are derived using the matched filter algorithm [39], which is equivalent to the backprojection algorithm described above. In this approach, the radar received signal is correlated with the PTR of a hypothetical point-target at an image cell located at $\vec{\boldsymbol{r}}$ to estimate the reflectivity at that image cell. In practice, only the conjugate phase of the PTR is used in the matched filter's transfer function. The PSF can be expressed as

$$\begin{aligned}\mathrm{PSF}\left(\vec{\boldsymbol{r}}, \vec{\boldsymbol{r}}_{\o}\right) &= \sum_{l=-\frac{L}{2}}^{\frac{L}{2}-1} \sum_{m=-\frac{M}{2}}^{\frac{M}{2}-1} \mathrm{PTR}\left(\vec{\boldsymbol{r}}_{\o}, \vec{\boldsymbol{r}}_{\boldsymbol{m}}, f_l\right) \exp\left(j \arg\{\mathrm{PTR}^*\left(\vec{\boldsymbol{r}}, \vec{\boldsymbol{r}}_{\boldsymbol{m}}, f_l\right)\}\right), \\ &= \sum_{l=-\frac{L}{2}}^{\frac{L}{2}-1} \sum_{m=-\frac{M}{2}}^{\frac{M}{2}-1} \exp\left(-j2k_l\left(\left|\vec{\boldsymbol{r}}_{\o} - \vec{\boldsymbol{r}}_{\boldsymbol{m}}\right| - \left|\vec{\boldsymbol{r}} - \vec{\boldsymbol{r}}_{\boldsymbol{m}}\right|\right)\right),\end{aligned} \tag{2.7}$$

where L is the number of frequency steps, M is the number of aperture samples, and $\arg\{\cdot\}$ is the phase of the expression between the brackets.

In the most general case, the expression in Eq. (2.7) cannot be further simplified, so the only way to rigorously determine the imgaing system's resolution would require numeric simulations. However, analytic expressions for the resolution can be established if certain simplifying assumptions are made.

First, the aperture vector length $|\vec{\boldsymbol{r}}_{\boldsymbol{m}}|$ is assumed to be much smaller than the pixel and target vector lengths, $|\vec{\boldsymbol{r}}|$ and $|\vec{\boldsymbol{r}}_{\o}|$, respectively. This is equivalent to assuming a narrow aperture. Making use of this assumption, the range to a pixel from aperture sample m is approximated:

$$|\vec{\boldsymbol{r}} - \vec{\boldsymbol{r}}_{\boldsymbol{m}}| \approx r - \frac{yy_m + zz_m}{r}. \tag{2.8}$$

A derivation of this approximation is available in Appendix A. A similar approximation can be established for the range $|\vec{\boldsymbol{r}}_{\o} - \vec{\boldsymbol{r}}_{\boldsymbol{m}}|$ to obtain

$$|\vec{\boldsymbol{r}}_{\o} - \vec{\boldsymbol{r}}_{\boldsymbol{m}}| - |\vec{\boldsymbol{r}} - \vec{\boldsymbol{r}}_{\boldsymbol{m}}| \approx r_{\o} - r - \frac{y_{\o}y_m + z_{\o}z_m}{r_{\o}} + \frac{yy_m + zz_m}{r}. \tag{2.9}$$

Furthermore, the approximation $r \approx r_{\o}$ is applied in the denominators in Eq. (2.9). This assumption implies that the investigated pixel is relatively close to the point-target. Finally, it is assumed that $k_l \approx k_c$ in the exponentials concerning y and z, implying a narrow bandwidth. These assumptions allow the double sum to be separated. The resulting PSF is approximated by the following expression:

$$\begin{aligned} PSF\left(\vec{\boldsymbol{r}}, \vec{\boldsymbol{r}}_{\o}\right) = & \sum_{l=-\frac{L}{2}}^{\frac{L}{2}-1} \exp\left(-j2k_l\left(r_{\o} - r\right)\right) \\ & \sum_{m=-\frac{M}{2}}^{\frac{M}{2}-1} \exp\left(-j2k_c \frac{y_m\left(y - y_{\o}\right)}{r_{\o}}\right) \exp\left(-j2k_c \frac{z_m\left(z - z_{\o}\right)}{r_{\o}}\right) \end{aligned} \tag{2.10}$$

In the following two subsections, a linear horizontal aperture and a grid like 2-D vertical aperture are considered.

2.2.1 Linear Aperture

A linear synthetic aperture oriented along the y axis is considered first, as shown in Fig. 2.1. The aperture is centered at $y = 0$ m and sampled at coordinates y_m in Δy increments, with $m = -\frac{M}{2}, ..., \frac{M}{2} - 1$, while x_a and z_a are the other two (fixed) aperture sample coordinates. The image is created in the ground plane ($z = 0$ m) and we consider a target placed in the ground plane as well ($z_{\o} = 0$ m).

For that configuration, the resulting PSF is:

$$\mathrm{PSF}\left(\vec{\boldsymbol{r}},\vec{\boldsymbol{r}}_{\o}\right)=\sum_{l=-\frac{L}{2}}^{\frac{L}{2}-1}\exp\left(-j2k_l\left(r_{\o}-r\right)\right)\sum_{m=-\frac{M}{2}}^{\frac{M}{2}-1}\exp\left(-j2k_c\frac{y_m\left(y-y_{\o}\right)}{r_{\o}}\right). \tag{2.11}$$

Each of the separate factors is computed based on the geometric series formula. The resulting PSF is

$$\mathrm{PSF}\left(\vec{\boldsymbol{r}},\vec{\boldsymbol{r}}_{\o}\right)\approx\frac{\sin\left(\frac{2\pi B}{c}\left(r_{\o}-r\right)\right)}{\sin\left(\frac{2\pi\Delta f}{c}\left(r_{\o}-r\right)\right)}\times\frac{\sin\left(\frac{2\pi A_y}{r_{\o}\lambda_c}\left(y-y_{\o}\right)\right)}{\sin\left(\frac{2\pi\Delta y}{r_{\o}\lambda_c}\left(y-y_{\o}\right)\right)}, \tag{2.12}$$

where $B = L\Delta f$ is the system bandwidth and $A_y = M\Delta y$ is the aperture length.

2.2.2 Vertical Grid Aperture

Next, the grid-like vertical aperture shown in Fig. 2.12 is analyzed. The grid is centered at $(x_a, 0, z_a)$ and treated as a set of N horizontal apertures, each containing M samples. Samples are uniformly spaced in y and z directions with a spacing of Δy and Δz, respectively. The image is now created in a 3-D cube, and the target is placed at an arbitrary position within the cube.

The analysis begins with Eq. (2.11); however, there are now N linear apertures, so a summation is added over $n \in \{-\frac{N}{2}, ..., \frac{N}{2}-1\}$. Aperture sample height is now a function of z_n and the resulting PSF contains three separable summations:

$$\begin{aligned}\mathrm{PSF}\left(\vec{\boldsymbol{r}},\vec{\boldsymbol{r}}_{\o}\right)=&\sum_{l=-\frac{L}{2}}^{\frac{L}{2}-1}\exp\left(-j2k_l\left(r_{\o}-r\right)\right)\sum_{m=-\frac{M}{2}}^{\frac{M}{2}-1}\exp\left(-j2k_c\frac{y_m\left(y-y_{\o}\right)}{r_{\o}}\right)\\&\sum_{n=-\frac{N}{2}}^{\frac{N}{2}-1}\exp\left(-j2k_c\frac{z_n\left(z-z_{\o}\right)}{r_{\o}}\right)\end{aligned} \tag{2.13}$$

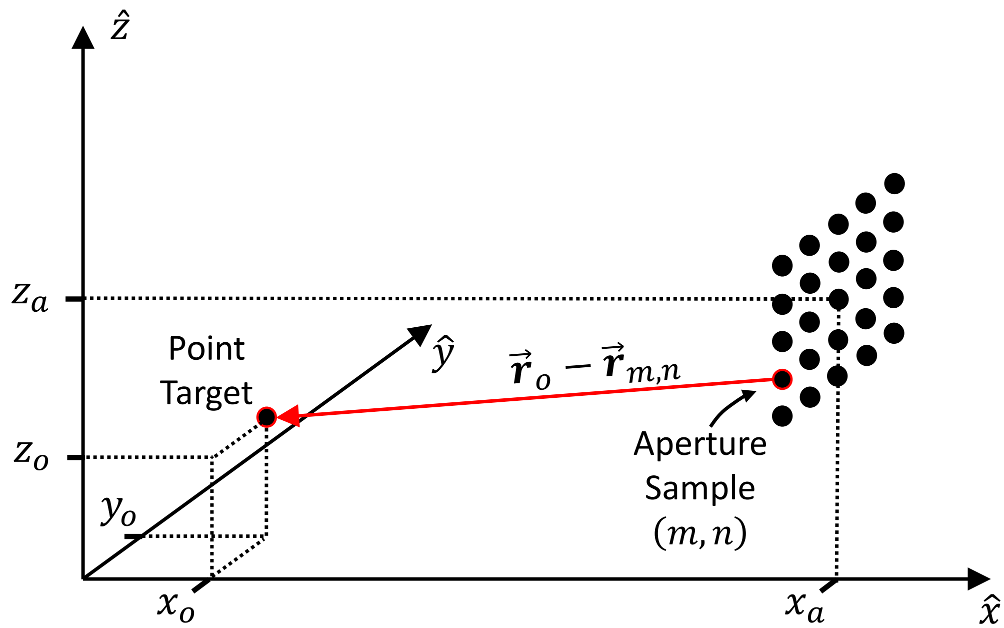

Figure 2.12. Grid aperture samples.

The resulting approximate PSF is:

$$\mathrm{PSF}(\vec{\boldsymbol{r}}, \vec{\boldsymbol{r}}_{\o}) \approx \frac{\sin\left(\frac{2\pi B}{c}(r_{\o} - r)\right)}{\sin\left(\frac{2\pi \Delta f}{c}(r_{\o} - r)\right)} \times \frac{\sin\left(\frac{2\pi A_y}{r_{\o}\lambda_c}(y - y_{\o})\right)}{\sin\left(\frac{2\pi \Delta y}{r_{\o}\lambda_c}(y - y_{\o})\right)} \times \frac{\sin\left(\frac{2\pi A_z}{r_{\o}\lambda_c}(z - z_{\o})\right)}{\sin\left(\frac{2\pi \Delta z}{r_{\o}\lambda_c}(z - z_{\o})\right)}. \tag{2.14}$$

2.3 Resolution and Ambiguity

According to the Rayleigh Criterion, the system's resolution is taken as half the mainlobe width in each direction [39]. The PSF expressions derived for the linear and grid apertures are identical in the radial and y directions. The radial terms in each PSF can be expanded in terms of x, y, and z using the following relations:

$$\begin{aligned} r &= x\cos\theta\cos\phi + y\cos\theta\sin\phi + z\sin\theta \\ r_{\o} &= x_{\o}\cos\theta_{\o}\cos\phi_{\o} + y_{\o}\cos\theta_{\o}\sin\phi_{\o} + z_{\o}\sin\theta_{\o}. \end{aligned} \tag{2.15}$$

where $z = z_\varnothing = 0$ m for the linear aperture. Again, we assume that the pixel is close to the target, so that $\theta \approx \theta_\varnothing$ and $\phi \approx \phi_\varnothing$. The range vector difference is given by

$$\begin{aligned} r_\varnothing - r &\approx (x_\varnothing - x)\cos\theta_\varnothing \cos\phi_\varnothing + (y_\varnothing - y)\cos\theta_\varnothing \sin\phi_\varnothing + (z_\varnothing - z)\sin\theta_\varnothing \\ &= \frac{(x_\varnothing - x)(x_\varnothing - x_a)}{r_\varnothing} + \frac{(y - y_\varnothing)\, y_\varnothing}{r_\varnothing} + \frac{(z_\varnothing - z)(z_\varnothing - z_a)}{r_\varnothing} \end{aligned} \tag{2.16}$$

This shows that the first sinc expression in Eq. (2.14) can determine resolution in both the x, y, and z directions. The resolution in each dimension is related to the radial resolution from Eq. (2.6) by

$$\begin{aligned} \delta_x &= \frac{\delta_r r_\varnothing}{|x_\varnothing - x_a|}, \\ \delta_y &= \frac{\delta_r r_\varnothing}{|y_\varnothing|}, \\ \delta_z &= \frac{\delta_r r_\varnothing}{|z_\varnothing - z_a|}. \end{aligned} \tag{2.17}$$

where $r_\varnothing = \sqrt{(x_\varnothing - x_a)^2 + y_\varnothing^2 + (z_\varnothing - z_a)^2}$. The resolution in each dimension is determined by the minimum between the contributing expressions.

$$\begin{aligned} \delta_x &= \frac{c}{2B}\frac{r_\varnothing}{|x_\varnothing - x_a|} \\ \delta_y &= \min\left(\frac{\lambda_c r_\varnothing}{2A_y}, \frac{c}{2B}\frac{r_\varnothing}{|y_\varnothing|}\right) \\ \delta_z &= \min\left(\frac{\lambda_c r_\varnothing}{2A_z}, \frac{c}{2B}\frac{r_\varnothing}{|z_\varnothing - z_a|}\right). \end{aligned} \tag{2.18}$$

It is assumed that the squint angle ϕ_s is small. Typically, the radial component of the resolution, relating to the bandwidth, determines the down-range resolution, δ_x. In the y and z dimensions, the size of the aperture in that dimension determines resolution. These expressions demonstrate the dependence that resolution has on target position. The resolution in the downrange dimension is degraded as $|y_\varnothing|$ increases but is improved as the height of the target approaches z_a. The cross-range resolution of the target improves as the down-range position of the target approaches x_a and as the height of the target approaches z_a. Vertical resolution improves as the down-range position of the target approaches x_a and degrades as $|y_\emptyset|$ increases. For the linear aperture, there is no vertical extent ($A_z = 0$ m) and $r_\emptyset \gg |z_\emptyset - z_a|$, so there is no vertical resolution.

The nulls of the denominators in the PSFs determine the locations of the image grating lobes. It is of interest to determine the distances from the mainlobe to the first grating lobe in each dimension. This is known as the unambiguous image size. These are

$$\begin{aligned} D_x^u &= \frac{c}{2\Delta f}\frac{r_\emptyset}{|x_\emptyset - x_a|}, \\ D_y^u &= \min\left(\frac{\lambda_c r_\emptyset}{2\Delta y}, \frac{c}{2B}\frac{r_\emptyset}{|y_\emptyset|}\right), \\ D_z^u &= \min\left(\frac{\lambda_c r_\emptyset}{2\Delta z}, \frac{c}{2B}\frac{r_\emptyset}{|z_\emptyset - z_a|}\right). \end{aligned} \tag{2.19}$$

The analysis from this section indicates the parameters in the system design that can be used to set the resolution and unambiguous ranges. For improved down-range resolution (small δ_x), a wide frequency bandwidth is necessary, as well as a small slant angle. To improve the cross-range resolution (decrease δ_y), a wide aperture, higher frequencies, and a short radar-image range should be used. The unambiguous ranges can be increased by reducing the sampling step size in frequency and aperture position, respectively. Cross-range resolution is dependent on squint angle, which is defined as the angle between antenna boresight and a vector perpendicular to the direction of travel. To improve resolution (decrease δ_y) under this condition, a wide aperture, higher frequencies, and a short radar-image range should be used. At large squint angles, cross-range resolution is improved by increasing signal bandwidth. This dissertation examines geometries with a small squint angle. Unambiguous range is determined by sampling step size in frequency and aperture.

It should be noted that the radar sensing configurations addressed in this dissertation do not satisfy the narrow bandwidth and narrow aperture assumptions made in this chapter. Particularly, the experimental setup described in Section 2.5 involves a wide frequency band and a wide angle aperture. Nevertheless, the formulas established in Section 2.2 are still useful in characterizing an imaging system.

2.4 Simulations

The expressions derived in Section 2.2 are verified herein using simulated PSFs. Any amplitude factors are ignored, such that all PSFs are normalized to their peak magnitudes.

The matched filter method from Eq. (2.7) is used to form simulated PSFs. The analytical PSFs derived in Section 2.2 are compared with the simulated PSFs to determine their validity. A target is simulated at $(x_{\o}, y_{\o}, z_{\o}) = (-1, 0.5, 1.5)$ m using the two types of apertures referenced in Section 2.2. This position is used to demonstrate that the derived PSF expressions are valid at any target position. As in the previous derivations, the aperture is set at a fixed across-track position, $x_a = 4$ m. Both the linear aperture and the vertical grid aperture have horizontal extents of $D_y = 5$ m. The spacing between samples is $\Delta y = 0.006$ m. For the grid aperture, the vertical extent is $D_z = 1.4$ m, and the vertical spacing between samples is $\Delta z = 0.05$ m. The frequency band of the simulation spans from 2.2 to 3.7 GHz with a 1.5-MHz sampling step size.

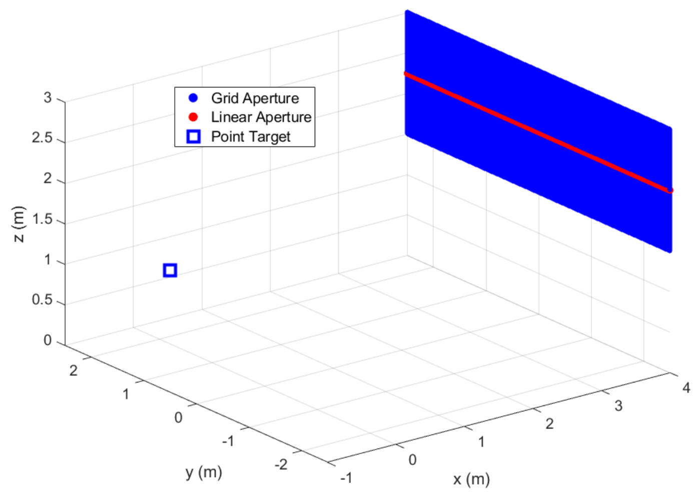

Figure 2.13. Linear and grid apertures and a point-target.

The simulated apertures and point-target are shown in Fig. 2.13. Typically, images formed using a linear aperture are created in the ground plane. The images in Fig. 2.14 are formed in two horizontal planes. A Hanning window was applied in both range and aperture dimensions in these images for sidelobe control. The first image is formed at the height of the target (1.5 m), and the second image was formed in the ground plane. Since there is no vertical resolution, the target response strength is the same at both heights. The image created at the target height shows the target at the correct (x, y) position and maintains the resolution dictated by the SAR parameters. The target response in the ground plane is shifted in across-track position.

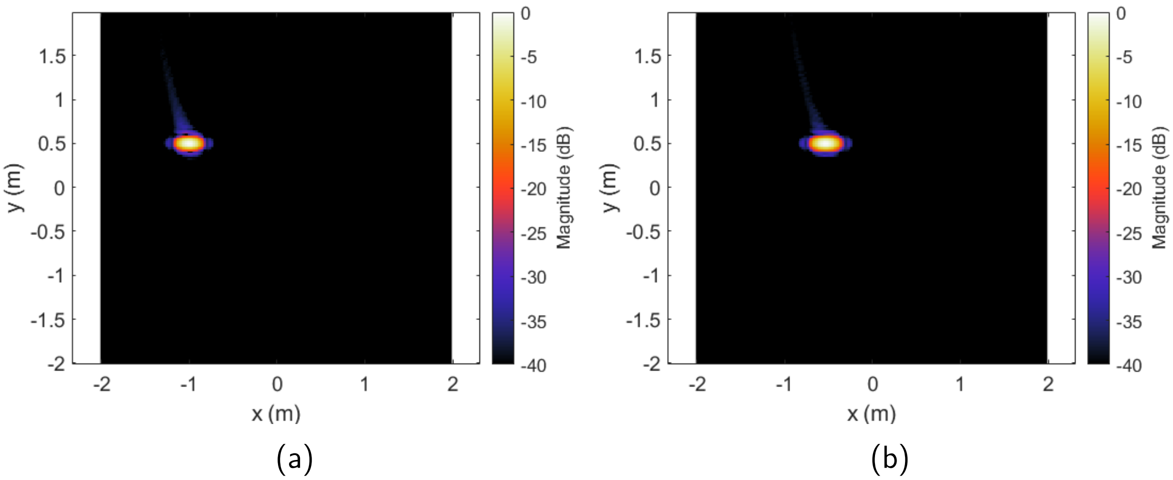

Figure 2.14. Image of point-target at $(x_\varnothing, y_\varnothing, z_\varnothing) = (-1, 0.5, 1.5)$ m created using a linear aperture with the image formation plane set to (a) $z = 1.5$ m and (b) $z = 0$ m.

The shift in across-track position is due to the nature of the vertical ambiguity of the radar image. Resolution is achieved on a sphere whose radius is the range from the center of the aperture to the target. Due to the lack of vertical resolution, a circle of ambiguity appears in the vertical plane perpendicular to the antenna's direction of travel. This circle, shown in Fig. 2.15, occurs at the cross-range position of the target. Vertical resolution resolves the ambiguity along this circle. The lack of vertical resolution results in out-of-plane scatterers and clutter projecting onto the image plane, degrading the target detection performance [42].

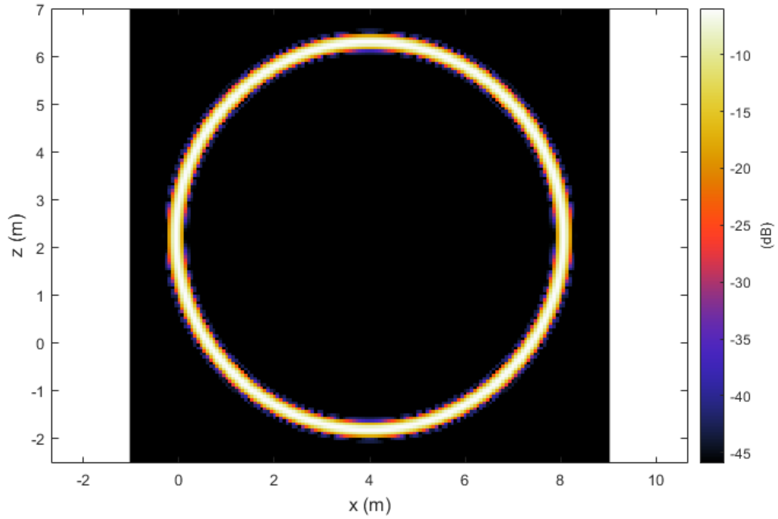

Figure 2.15. Circle of ambiguity around a linear aperture at a fixed cross-range position.

The expected resolution in each dimension at the height of the target is $\delta_x = 0.101$ m and $\delta_y = 0.051$ m. 1-D slices of the image created at $z = 1.5$ m are shown in the x and y dimensions below. These slices are compared with the formulas in Eq. (2.12). From Fig. 2.16, it is clear that the analytic PSF follows the simulation closely. The simulated resolution in the x-direction was 0.104 m, which is a slight deviation from the derived resolution. In the y-direction, the simulated resolution is 0.06 m, which is 4 mm larger than the analytical resolution. The simulated and analytical PSFs increasingly diverge as a function of distance from the mainlobe. This occurs because the narrow band, narrow aperture and small image assumptions used in the PSF derivation are not satisfied. For the set of SAR parameters considered here, the wavefront curvature is large, so coherence is lost quickly away from the target. However, these differences in side-lobe magnitude do not detract from the utility of the PSF analysis. The resolution formulas derived for an image formed in the xy-plane using a linear aperture are adequately accurate for the purpose of determining the properties of an image given a set of radar parameters.

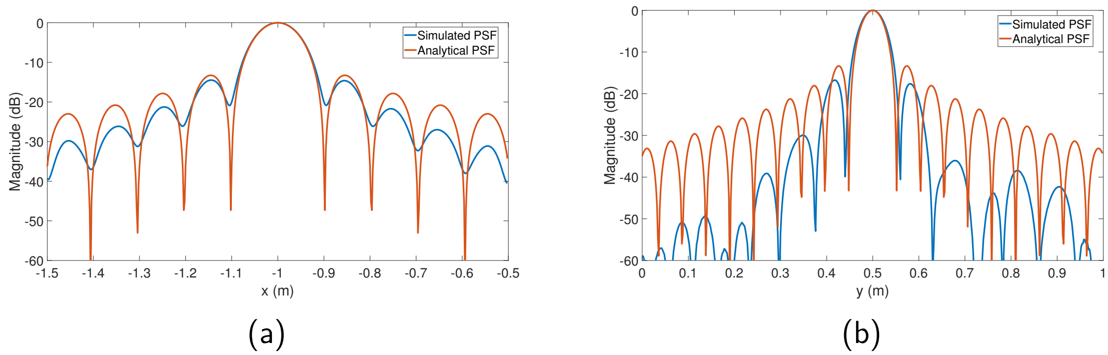

Figure 2.16. Comparison plots of the simulated and analytic PSFs for the linear aperture in the (a) x and (b) y directions over the target peak.

Next, the derived PSF for a vertical grid is compared with simulated data. Figure 2.17 shows images formed in horizontal planes placed at z = 1.5 m and $z = 0$ m for the vertical grid aperture and target shown in Fig. 2.13. These images were formed using a Hanning window in both the range and aperture dimensions. The dynamic range is increased from 40 dB to 50 dB so that the artifacts in the ground plane image are visible. The target is only present in the image formed at 1.5 m, which is the height of the target. Vertical resolution has removed the ambiguity between those two images. The image formed at the ground plane shows sidelobes from the target PSF. The strongest response of these sidelobes is about 35 dB weaker than the peak of the target response.

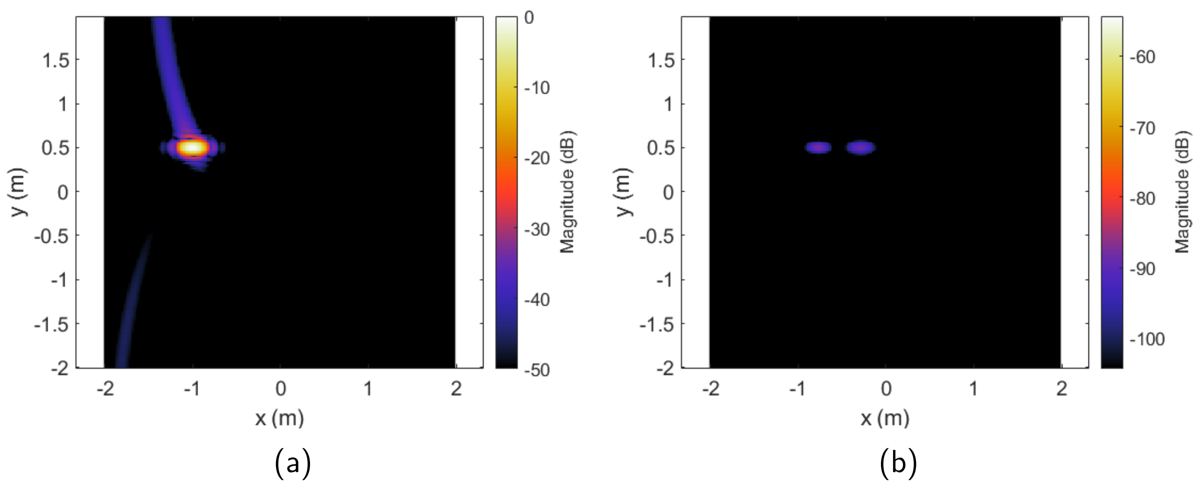

Figure 2.17. Image of point-target at $(x_\emptyset, y_\emptyset, z_\emptyset) = (-1, 0.5, 1.5)$ m created using a vertical grid aperture with the image formation plane set to (a) $z = 1.5$ m and (b) $z = 0$ m.

Fig. 2.18 shows an image in the xz-plane at the cross-range position of the point-target. Vertical resolution is realized in the circle of ambiguity around the aperture whose radius is equal to the range from the center of the aperture to the target. With vertical resolution, a target is imaged at the true height and is not projected into any 2-D image plane. This is true for any scattered response, including clutter.

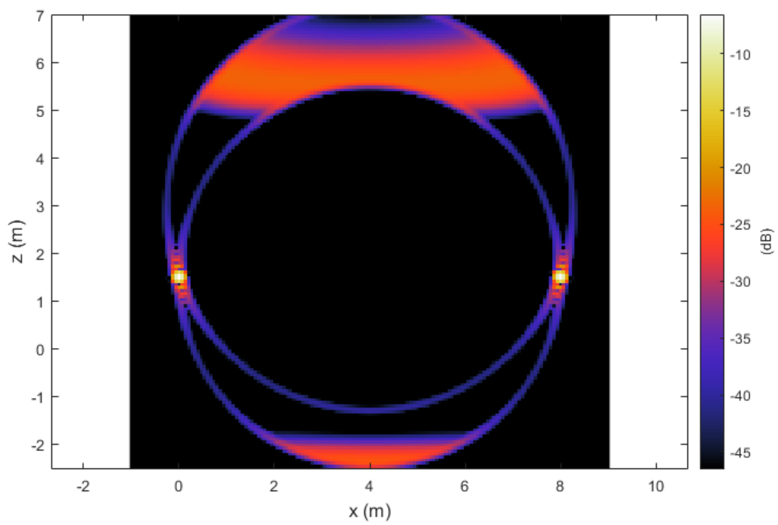

Figure 2.18. Image in the xz-plane at the cross-range position of a point-target using a vertical grid aperture.

Next, the resolution of the analytic PSF is compared with that of the simulated PSF. According to Eq. (2.18), the resolution in the x-, y-, and z-directions are, respectively, given as $\delta_x = 0.101$ m, $\delta_y = 0.051$ m, and $\delta_z = 0.185$ m. Amplitude values through the center of the target are shown in the x, y, and z directions for both the analytical and simulated PSF in Fig. 2.19. In both the x-and y-directions, the simulated PSFs showed the same results as in the case of the linear aperture. In the z-direction, the simulated PSF had a resolution of 0.198 m, which is 7 mm coarser than that of the analytical PSF. Thus, in the vertical dimension, the analytical expression is also valid.

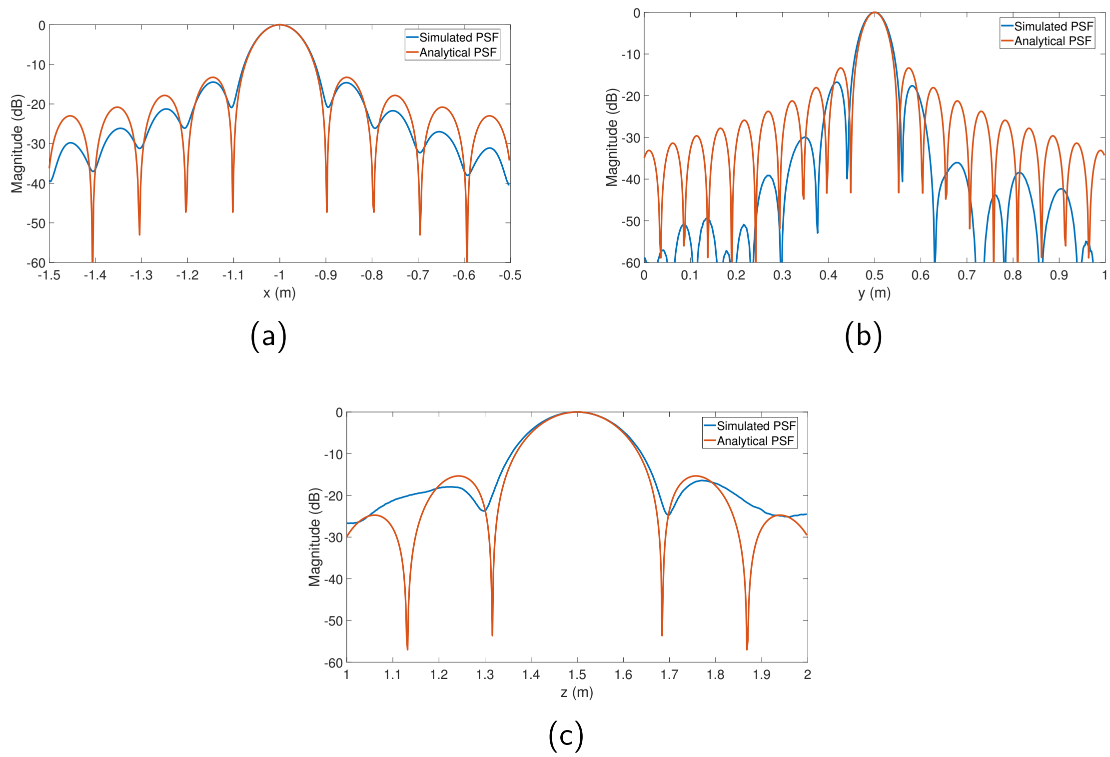

Figure 2.19. Comparison plots of the simulated and analytic PSFs for the vertical grid aperture in the (a) x-, (b) y-, and (c) z-directions over the target peak.

These PSF simulations agree well with the analytical expressions derived in Sec. 2.2 despite the approximations applied in those derivations. This is particularly true with regard to the PSF's mainlobe, which determines the imaging system's resolution. The resolution is the most important performance metric of the imaging system, indicating the system's ability to accurately represent the scene under investigation.

Next, the effects of aperture sampling on grating lobe spacing are investigated. Data are simulated for a point-target using an undersampled linear aperture and a vertical grid aperture that is undersampled in both the vertical and horizontal directions. The expressions in Eqs. 2.12 and 2.14 are compared with the simulated results to determine their validity in estimating grating lobe position, magnitude, and shape.

First, a linear aperture is considered, with $A_y = 2$ m, $x_a = 4$ m and $z_a = 2.0660$ m. The aperture is sufficiently sampled, so grating lobes are not present in the image. Data are simulated for a point-target at $(x_ø, y_ø, z_ø) = (0, 0, 1.5)$ m. The aperture and point-target are shown in Fig. 2.20.

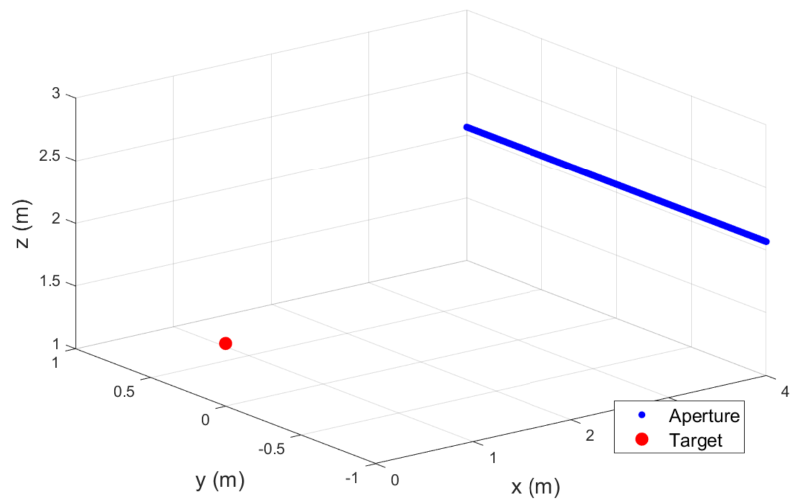

Figure 2.20. Linear aperture and point-target.

The resulting image in xy-plane at $z = 1.5$ m is shown in Fig. 2.21. A window is applied in the frequency domain for range sidelobe suppression. A window is not applied in the aperture domain to preserve sidelobes for analysis.

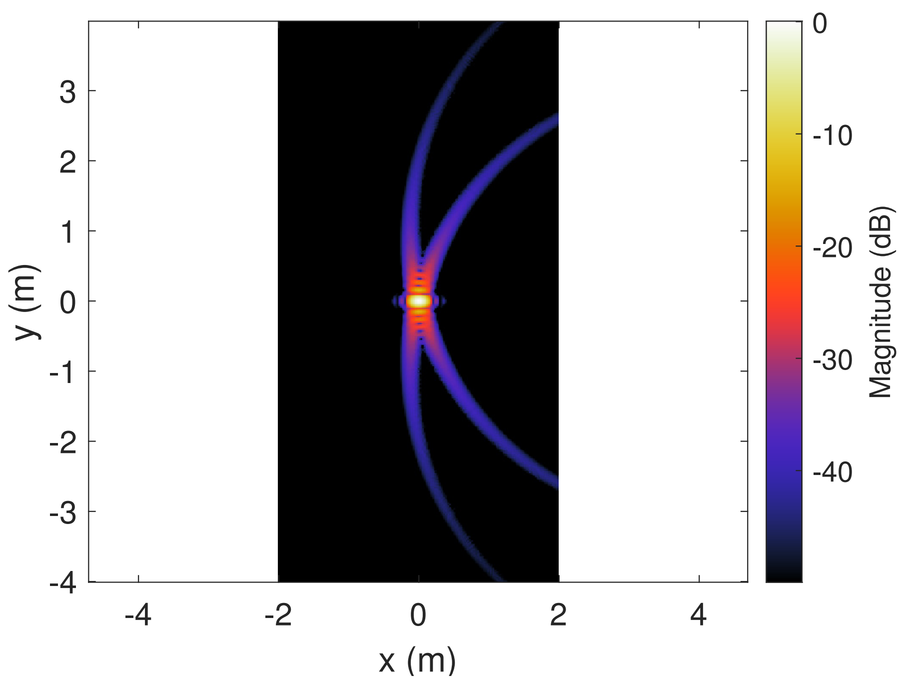

Figure 2.21. Image formed for aperture and point-target in Fig. 2.20.

The position of these artifacts can be described using ambiguity spheres around specific aperture points. First, the sidelobes are distributed on the intersection of the image formation plane with the sphere of ambiguity around the aperture position at the same cross-range position as the target. In this case, this is the central sample on the aperture. This aperture sample position is $(x_c, y_c, z_c) = (4, 0, 2.0660)$ m. The intersection of a plane and a sphere is a circle in that plane. The radius of this circle is the ground range from the aperture sample to the target, $r_{g,c} = \sqrt{(x_c - x_ø)^2 + (y_c - y_ø)^2}$. The image formation plane is at the height of the target $z_ø$. The equation of the circle is given by

$$\frac{(x - x_c)^2}{r_{g,c}^2} + \frac{(y - y_c)^2}{r_{g,c}^2} = 1. \tag{2.20}$$

Next, the cat whiskers are distributed along the intersections of the IFP with ambiguity spheres centered around the two ends of the aperture. The positions of the ends of the aperture are given by $(x_1, y_1, z_1) = (4, -1, 2.0660)$ m and $(x_2, y_2, z_2) = (4, 1, 2.0660)$ m. Circles describing the intersections of IFPs and ambiguity spheres follow the formula in Eq. (2.20). Fig. 2.22 shows the circles discussed above. The image of the point-target is plotted below with the aperture for reference. The circle around the center of the aperture is plotted in green. The circle containing the cat whisker sidelobes are plotted in red. These are labeled as bounding circles.

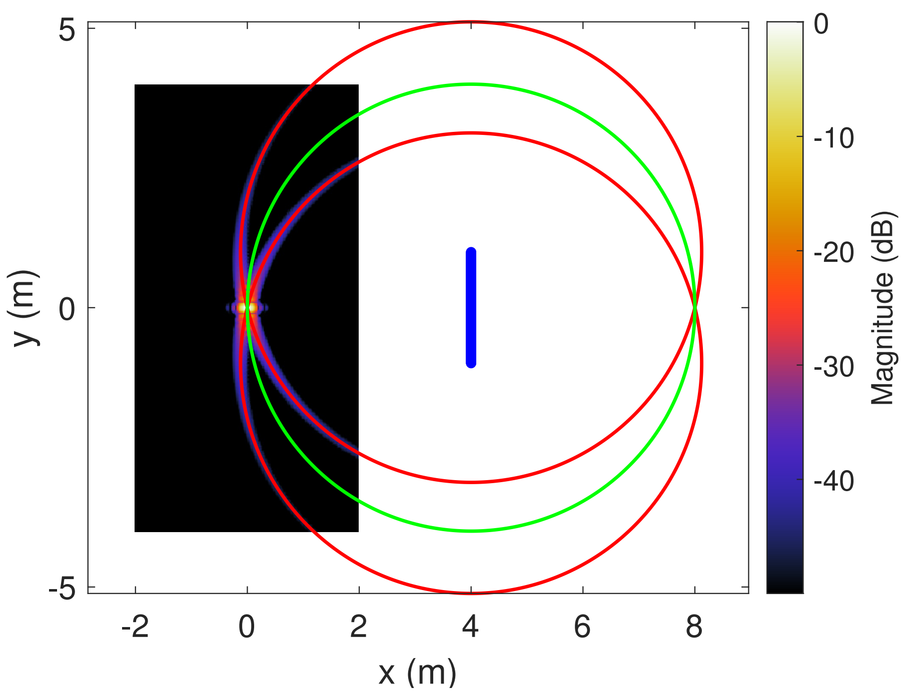

Figure 2.22. Image of point-target formed using a linear aperture, annotated with curves containing artifacts of interest.

These circles are important in determining the distribution of grating lobes in undersampled apertures. Close to the target, the assumptions used to derive Eq. (2.12) are valid. At these points, the grating lobes are distributed along the circle around the center of the aperture. Furthermore, it can be assumed that they are displaced in the y-direction only. As the grating lobes occur further from the target, they appear diffused and do not match the analytical expression as well, with the energy dispersed between the inner and outer bounding circle. This is demonstrated using the sparse aperture in Fig. 2.23.

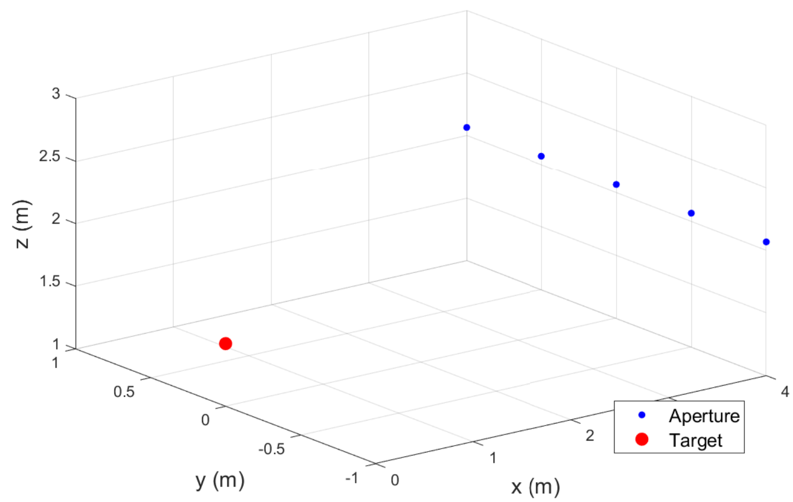

Figure 2.23. Undersampled linear aperture.

The resulting image is shown in Fig. 2.24. As discussed before, the grating lobes close to the target are similar in shape to the primary target response. Further from the target, the energy is more dispersed.

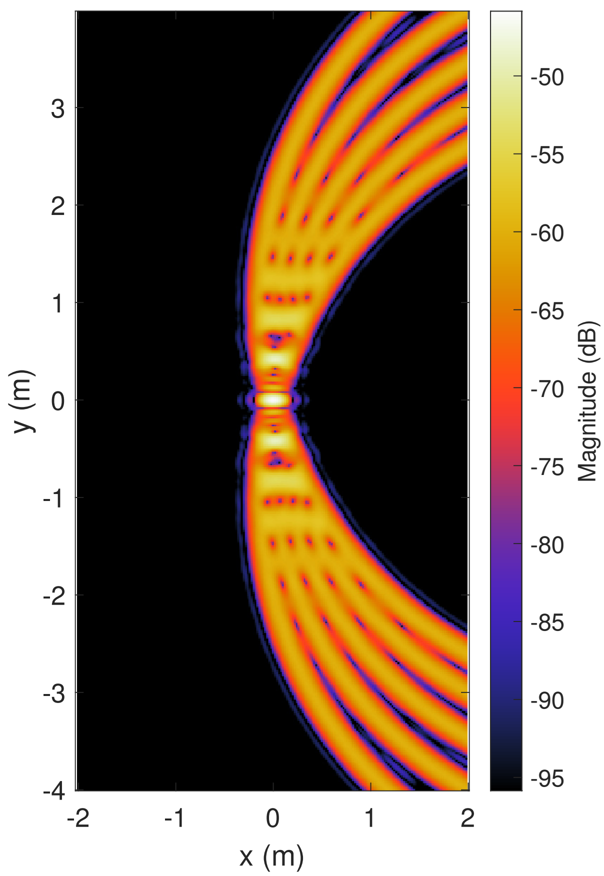

Figure 2.24. Image formed using undersampled linear aperture.

Fig. 2.25 shows a comparison between a slice of this PSF at $x = 0$ m and the analytical PSF. The close match between the simulated and analytical target response were already demonstrated in Fig. 2.16. Here, the grating lobes and sidelobes are examined. In the analytical PSF, the pattern repeats with no deviations. This is due to the assumption that the aperture and bandwidth are both narrow. This simulation uses both a wide aperture and a wide bandwidth, so the grating lobes do not follow the same pattern. As the image sampling point gets further from the target, the width of the grating lobe peaks spread in both range and cross-range, while their amplitudes decrease.

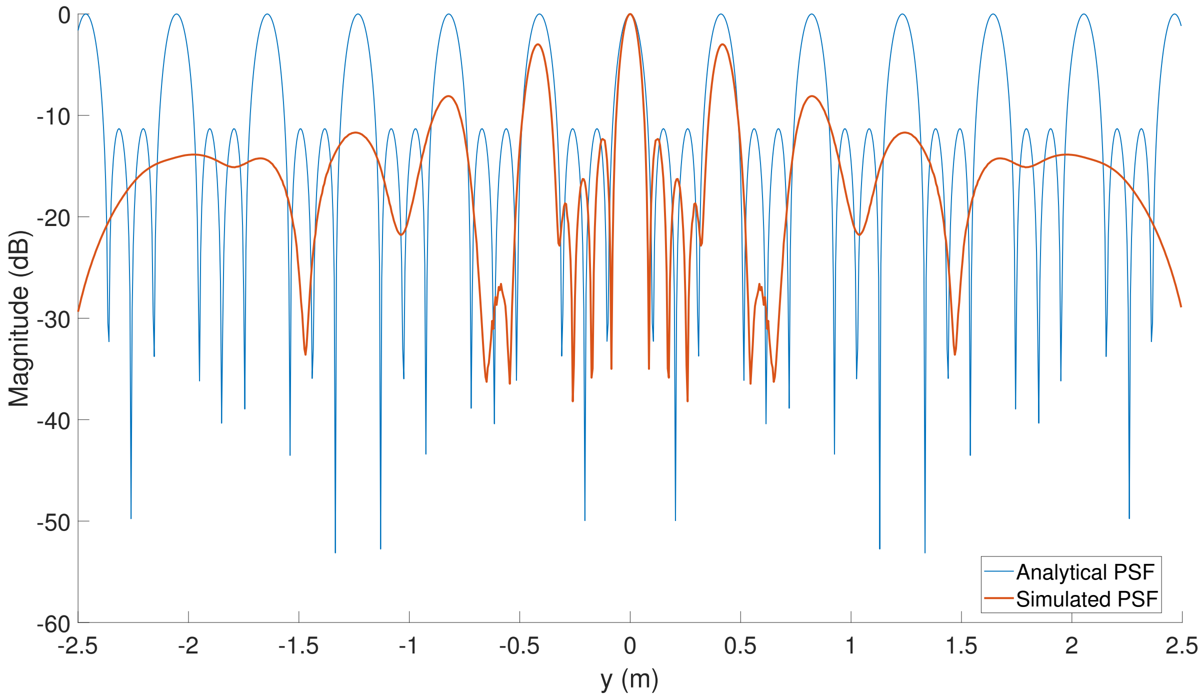

Figure 2.25. Comparison between an analytical and simulated PSF for an undersampled linear aperture in the cross-range direction.

The error in peak location is shown in Table 2.1. The PSF is symmetrical because the target is centered with respect to the aperture, so only the grating lobes on one side of the target are considered. Grating lobes of the same order have the same values. The error in the peak position is extremely small for the grating lobes considered here.

Table 2.1. Grating lobe position and position error for a simulated undersampled linear aperture.

Peak Order	Analytical Location (m)	Simulated Location (m)	Error (m)
1	0.41	0.42	0.01
2	0.82	0.825	0.005
3	1.23	1.245	0.015

The main differences between the simulated and analytical data are the peak value and the grating lobe width. In the analytical PSF, each grating lobe has the same magnitude and width as the mainlobe. The magnitude of the mainlobe peak is normalized to 0 dB, and the nominal image cross-range resolution is $\delta_z = 0.105$ m. Table 2.2 shows the simulated peak magnitude and grating lobe width for the first three grating lobes. The the first grating lobe has half the power of the mainlobe. The power drops off greatly from there. Also, the resolution of the first grating lobe is very close to the mainlobe resolution.

Table 2.2. SCR in imagery created using grid aperture and linear aperture.

Peak Order	Simulated Peak Magnitude (dB)	Simulated Peak Width (m)
0	0	0.084
1	-2.99	0.1125
2	-8.10	0.1950
3	-11.69	0.2150

For the vertical grid aperture, grating lobes are now resolved to specific heights depending on where the sampling occurs. The same principles apply to the grating lobes for the grid aperture. Grating lobes farther from the target response have lower peaks and are more dispersed. The slant angle from the center of the aperture will cause a slight tilt to the response. Fig. 2.26 shows a sparse vertical grid aperture and a point-target at $(x_\o, y_\o, z_\o) = (0, 0, 1.5)$ m. The aperture lengths of the aperture are $A_y = 0.8$ m and $A_z = 0.8$ m, while the aperture sample spacings are $\Delta y = 0.4$ and $\Delta z = 0.4$ m.

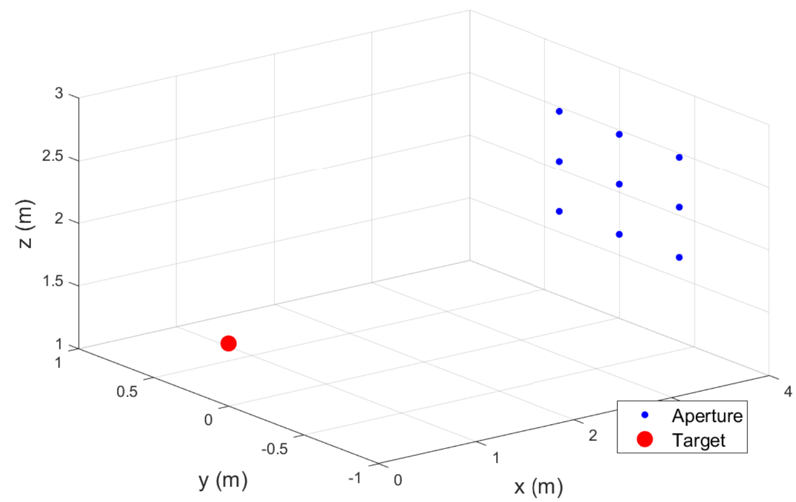

Figure 2.26. Undersampled grid aperture and a point-target.

The resulting image is shown in Fig. 2.27.

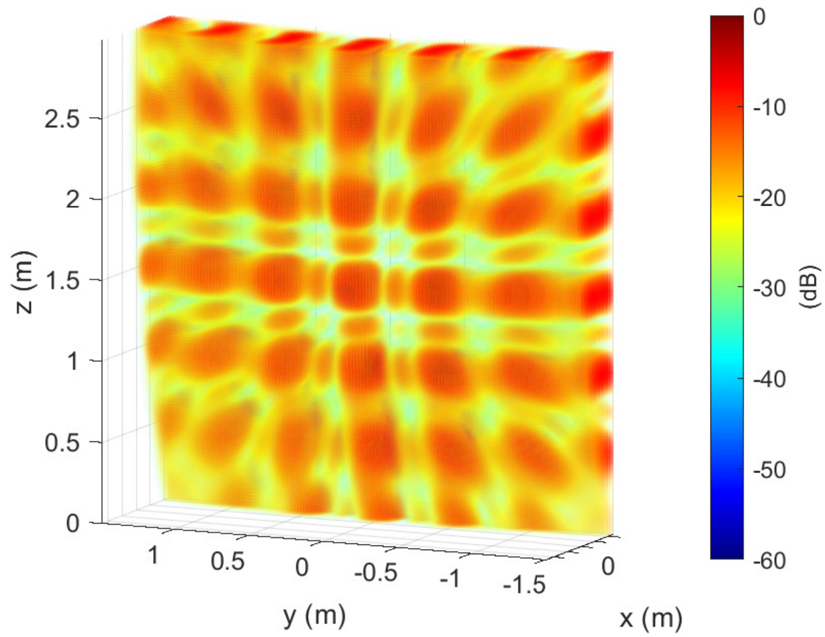

Figure 2.27. 3-D image formed using an undersampled grid aperture.

A plot through the target in the y-direction is plotted in Fig. 2.28. The same pattern is present as in the linear aperture. The width and magnitude of the grating lobe are similar to those of the mainlobe at the target location, and the third grating lobe is more diffused.

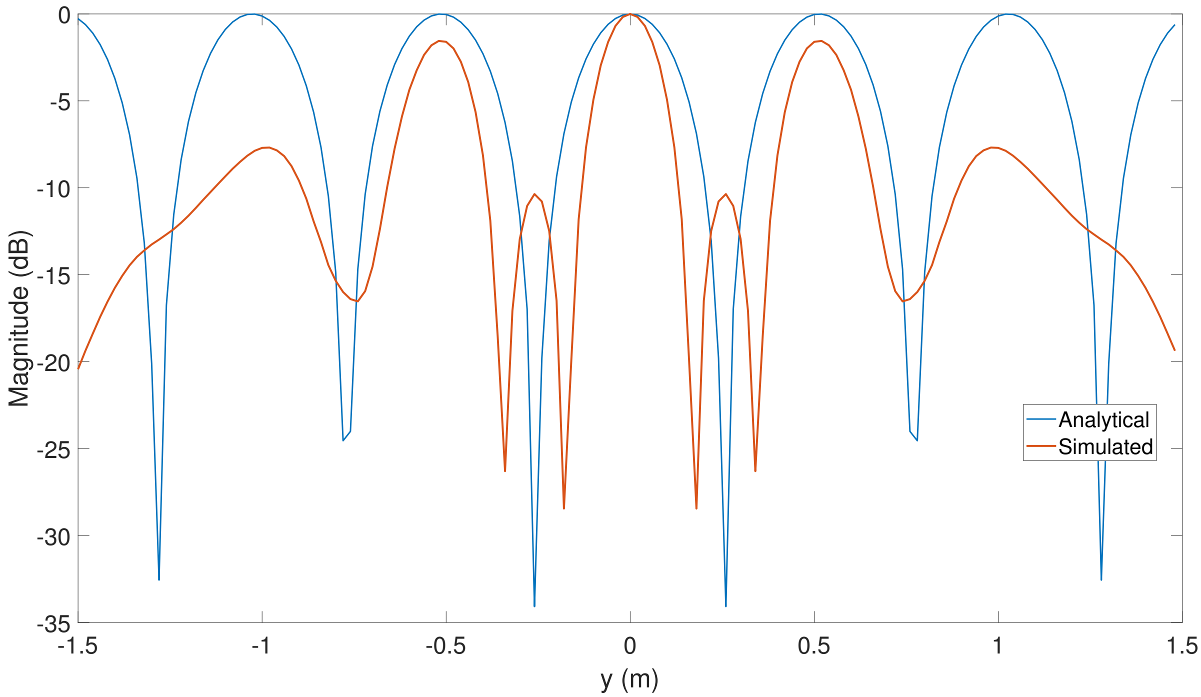

Figure 2.28. A plot along the y-axis through a point-target.

A plot through the target in the z-direction is shown in Fig. 2.29. Again, the resolution of the simulated PSF is finer than the analytical PSF. The simulated PSF in this direction is asymmetrical due to the slant angle from the aperture to the target. This disperses the energy below the target quickly. The grating lobes above the target remain strong.

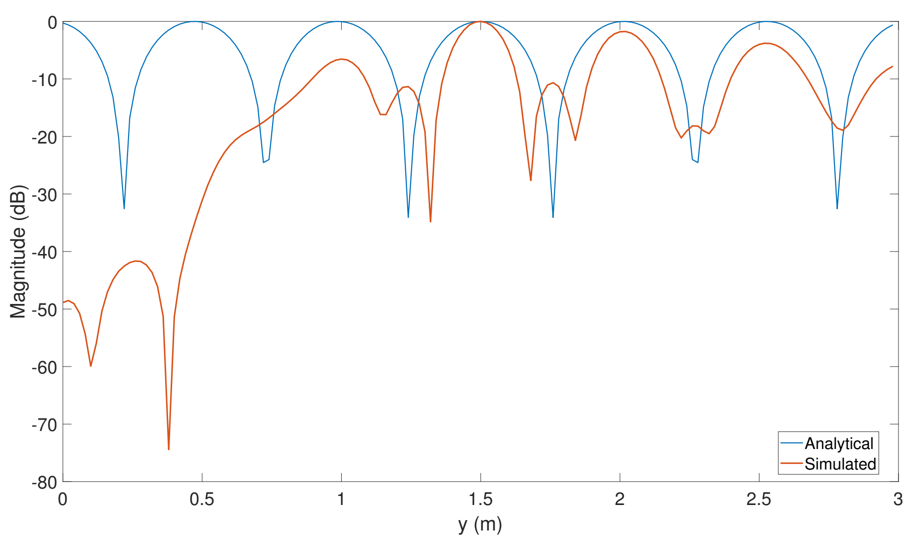

Figure 2.29. A plot along the z-axis through a point-target.

In this section, simulated PSFs were compared with the analytical PSFs in Eqs. 2.12 and 2.14. The analytical expressions were derived using a set of assumptions that were not satisfied by the investigated SAR configuration; however, by comparing these expressions with rigorous numerical simulations, it was shown that the analytical expressions provided accurate estimates of important SAR parameters such as resolution and grating lobe spacing. This is an important result for expediting the process of estimating SAR system performance, as well as establishing a baseline for the system design. Analytical expressions provide a much quicker method of calculation than numerical simulations, with a negligible difference in accuracy, and they play an important role in the analysis presented in Chapters 3 and 4.

2.5 Experimentation

In this section, the concept of vertical resolution is investigated further using measured radar data. A radar was placed on a linear scanning system, shown in Fig. 2.30a. This consists of both a horizontal and vertical linear scanner, which is able to step through positions to generate a desired aperture.

The observed test scene is shown in Fig. 2.30b. Two surrogate metal landmines, with a diameter of 0.3454 m and a height of 0.09 m, are used. The landmines are placed 4 m in ground range from the scanner axis. They are labeled Target 1 and Target 2, with Target 1 placed at a height of 1.4 m and Target 2 at a height of 0.7 m. This experiment is designed to demonstrate the resolution afforded by the vertical grid aperture. Furthermore, it is used to demonstrate the importance of vertical resolution in imaging objects above the ground.

(a) (b)

Figure 2.30. a) Scanner at ARL facility capable of both vertical and horizontal scanning. b) Two landmines stacked vertically using styrofoam blocks.

The radar used to collect the data uses a Xilinx RF system-on-a-chip digital back-end paired with a custom RF front end. The operating band of this system is 2.2 to 3.7 GHz. A stepped-frequency waveform with a 1.5-MHz frequency step-size is used. The grid aperture was sampled with an along track spacing of 0.006 m and a vertical spacing of 0.05 m. The across-track position of the scanner remains at 0 m.

The two apertures are shown in Fig. 2.31. In the first experiment, data were collected with a linear aperture at a height of 2 m. Since the linear aperture does not achieve vertical resolution, the imagery is formed in the ground plane. Data collected with a vertical grid aperture have vertical resolution. Thus, a 3-D image can be created. Imagery is shown as slices through the 3-D volume.

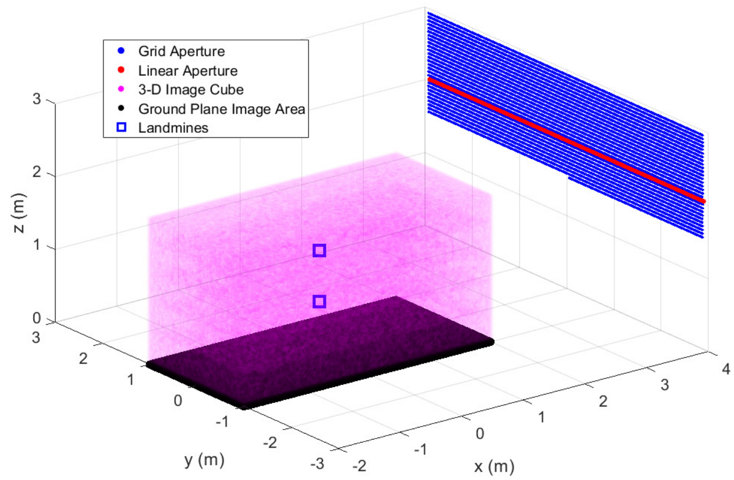

Figure 2.31. Linear aperture, two landmines, and the image area.

The ground plane image created using the linear aperture is shown in Fig. 2.32. Energy from objects at all heights are projected onto the ground plane. Thus, even though these two targets are at different heights, it is difficult to distinguish them from one another in the ground plane image. Furthermore, all clutter in the surrounding environment that may be at different heights is projected into this area.

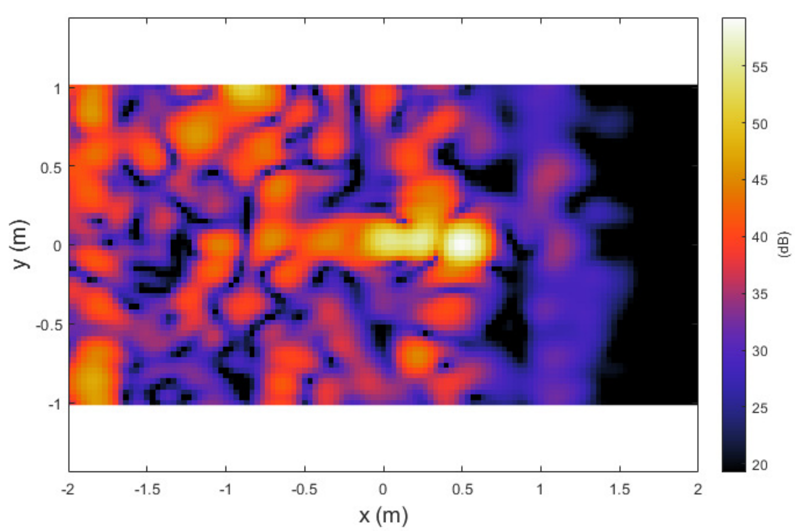

Figure 2.32. Ground plane image of the test scene using data collected with a linear aperture.

The images of the targets obtained with the 3-D imaging system, in horizontal planes at $z = 0.7$ m and $z = 1.4$ m, are shown in Fig. 2.33

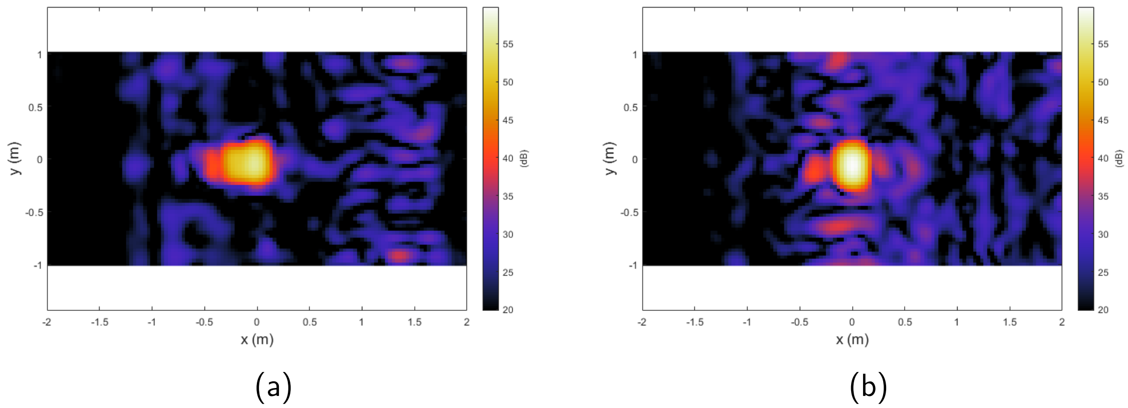

Figure 2.33. Horizontal slices of 3-D image containing vertically displaced landmines at (a) $z = 0.7$ m and (b) $z = 1.4$ m.

The ability to detect targets in these images can be determined using SCR. This ratio is defined as the ratio of the peak of the target to the mean of the pixel/voxel power. Table 2.3 shows a list of SCR values for both of the landmine targets from the images created using the linear aperture and vertical grid aperture. A circle of radius 0.3 m is used to remove the landmine from the calculation of the mean clutter power. For the linear aperture, the image was created in the ground plane, so the target and clutter values were taken from the same image for both Target 1 and Target 2. In general, the images generated using the vertical grid apertures had better SCRs, resulting from the spatial separation of the clutter. The SCR improvement using a grid aperture was 10.8 dB for Target 1 and 11.9 dB for Target 2. Part of why the SCR was smaller when using a linear aperture was because Target 1 was included in the clutter mean for the SCR calculation for Target 2, and vice versa. Spatially separating these targets would improve the SCR.

Table 2.3. SCR in imagery created using grid aperture and linear aperture.

Target	Aperture	Peak (dB)	Mean (dB)	SCR (dB)
Target 1	Linear	59.3	34.3	25.0
Target 2	Linear	55.9	34.3	24.7
Target 1	Grid	59.8	24.1	35.8
Target 2	Grid	55.7	22.2	33.6

Fig. 2.34 shows a comparison between a yz-slice of the image created using a vertical grid at the cross-range position containing the targets. A model was created using the same geometry and set of frequencies using the ARL finite-difference time-domain (AFDTD) electromagnetic modeling software [43]. A simplified landmine model was used to represent the target scene. There is excellent agreement between the images created by the measured data and the modeled data. This shows that most of the artifacts present in the experimental image are signals and sidelobes created by the targets themselves, rather than artifacts from clutter or the imaging procedure.

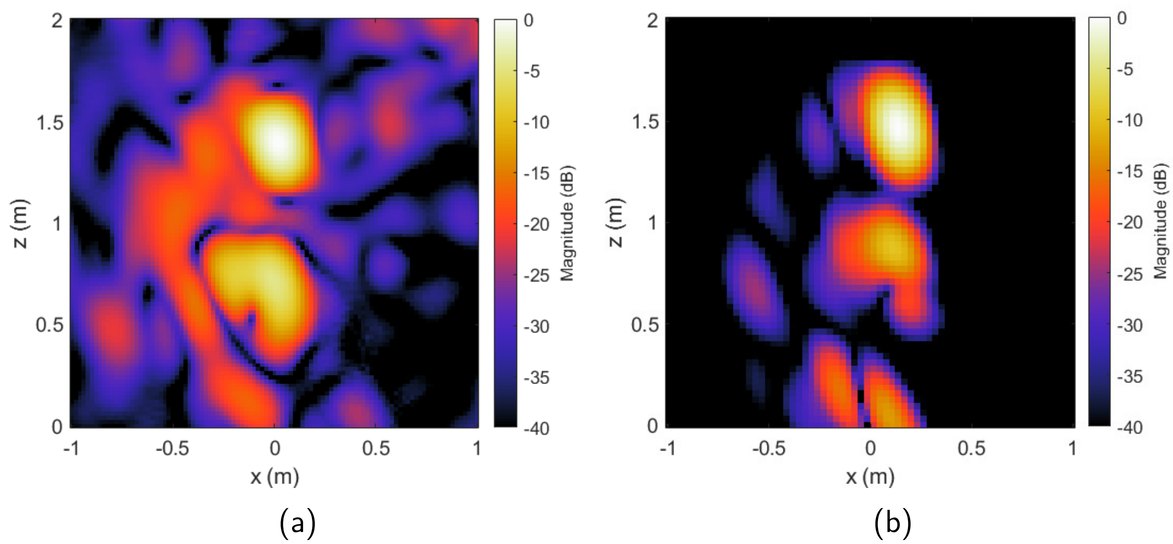

Figure 2.34. Comparison of imagery in an across-track-vertical slice of the 3-D image at the along track position of the landmine targets between (a) experimental data and (b) modeling data.

Finally, Fig. 2.35 shows a 3-D image created using the 3-D data volume from the grid aperture data. The data are rendered by varying the opacity of the image proportionally with the voxel strength. The strongest voxels are the most opaque and the weakest voxels are transparent, and each dB correlates to 5% of transparency. A 20-dB dynamic range is used for this representation so that the targets are displayed clearly; however, with this representation the two targets are easily identified and localized in 3-D space.

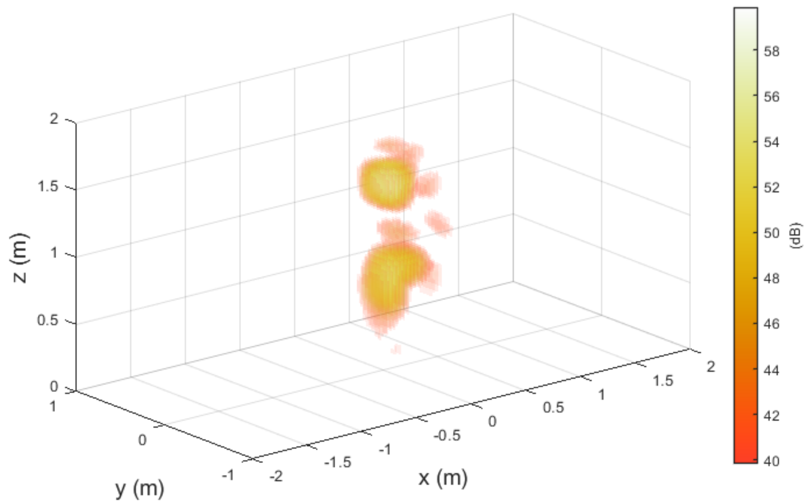

Figure 2.35. 3-D image of landmines.

Chapter 3
Imaging Artifacts and the Recursive Sidelobe Minimization Technique

In Chapter 2, 3-D images were generated using a vertical grid aperture. The aperture samples were uniformly spaced at an interval less than a quarter of a wavelength, resulting in well-organized sidelobes that can be efficiently suppressed using an aperture window. The strict sampling requirements necessary to avoid grating lobes leads to a large set of aperture samples, which places a great strain on the experimental system. Small UAV platforms have limited battery life, which restricts the number of aperture samples that can be collected in a single flight. The ability to form imagery from a single pass of a scene, rather than passing the scene many times to form a vertical grid aperture, would allow the radar to scan and image much larger areas. This motivates the need for a method of imaging using sparse apertures to reduce the number of necessary aperture samples.

By reducing the number of aperture samples, the sample spacing increases beyond the quarter-wavelength requirement. This creates either large random sidelobes or grating lobes depending on the aperture sampling. Regular sampling in the aperture creates grating lobes, which are coherent replicas of the target response that occur at periodic spacings from the target position. It is shown that grating lobes are avoided if the spacing between aperture samples is irregular. The resulting sidelobes are removed using the RSM algorithm, which is an iterative apodization method used to suppress noncoherent artifacts in an image. This technique does not remove grating lobes when applied to a uniform aperture. However, the RSM is coupled with irregularly sampled apertures as a method of sparse aperture 3-D imaging.

3.1 Synthetic Aperture Radar Ambiguities

The expressions in Eq. (2.14) describe the PSF using a regularly sampled aperture. The spacing of grating lobes is tied to aperture sample spacing. No analytical expression is available for irregularly sampled apertures, so simulations are performed to characterize PSFs for these cases.

Three apertures, shown in Fig. 3.1, are used to investigate the artifacts generated using irregularly sampled apertures. The first aperture, a zig-zag aperture, is periodically sampled along a curve, rather than in the horizontal or vertical direction. The second aperture is sampled at irregular intervals. Finally, a uniformly sampled aperture is used for comparison.

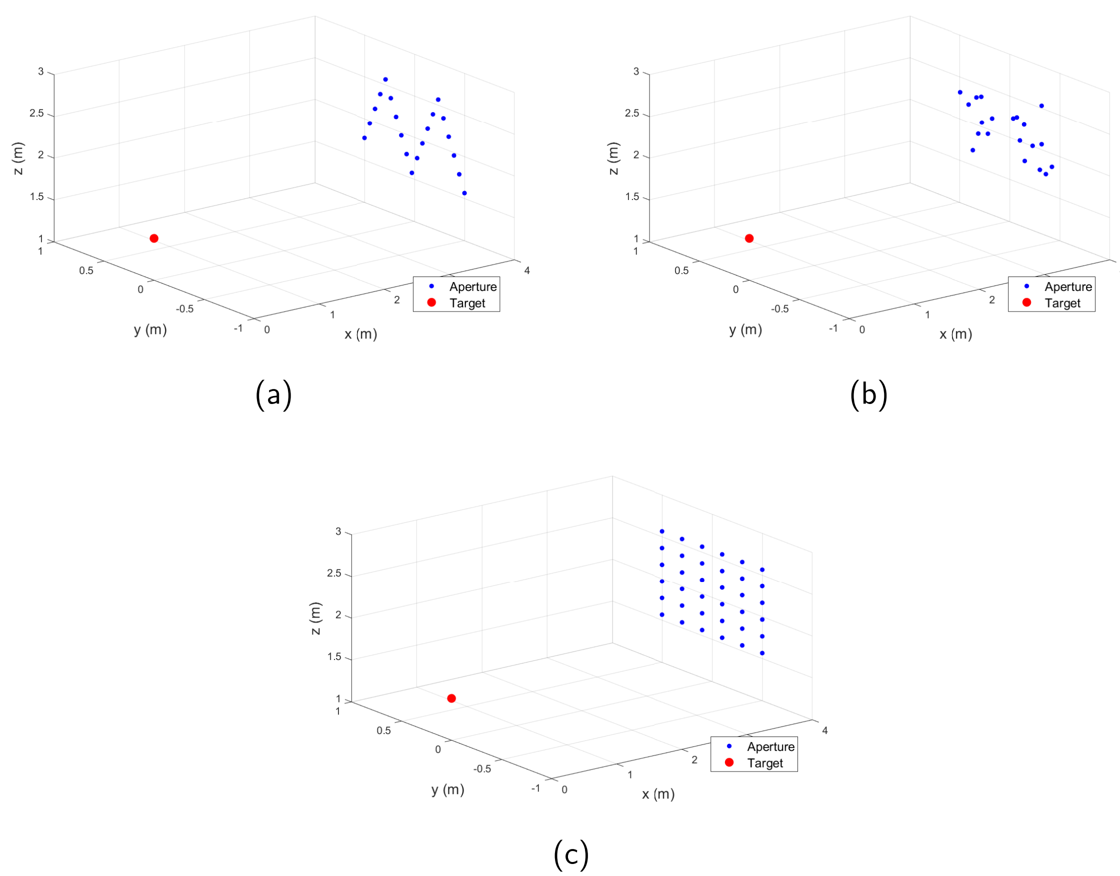

Figure 3.1. Simulated point target for (a) a zig-zag aperture, (b) an irregularly sampled aperture, and (c) a uniformly sampled aperture.

The resulting PSFs are plotted in Fig. 3.2. In the image generated using the zig-zag aperture, there are sidelobes fanning out from the target response in the horizontal direction. This entire response is repeated above and below the target. The periodicity indicates that the central responses that emulate the main target response are grating lobes. For the aperture with irregular sampling, the artifacts are dispersed randomly with no discernible pattern. These are labeled as sidelobes. For the uniformly sampled aperture, the ambiguities are periodic in both the horizontal and vertical directions. These peaks are grating lobes.

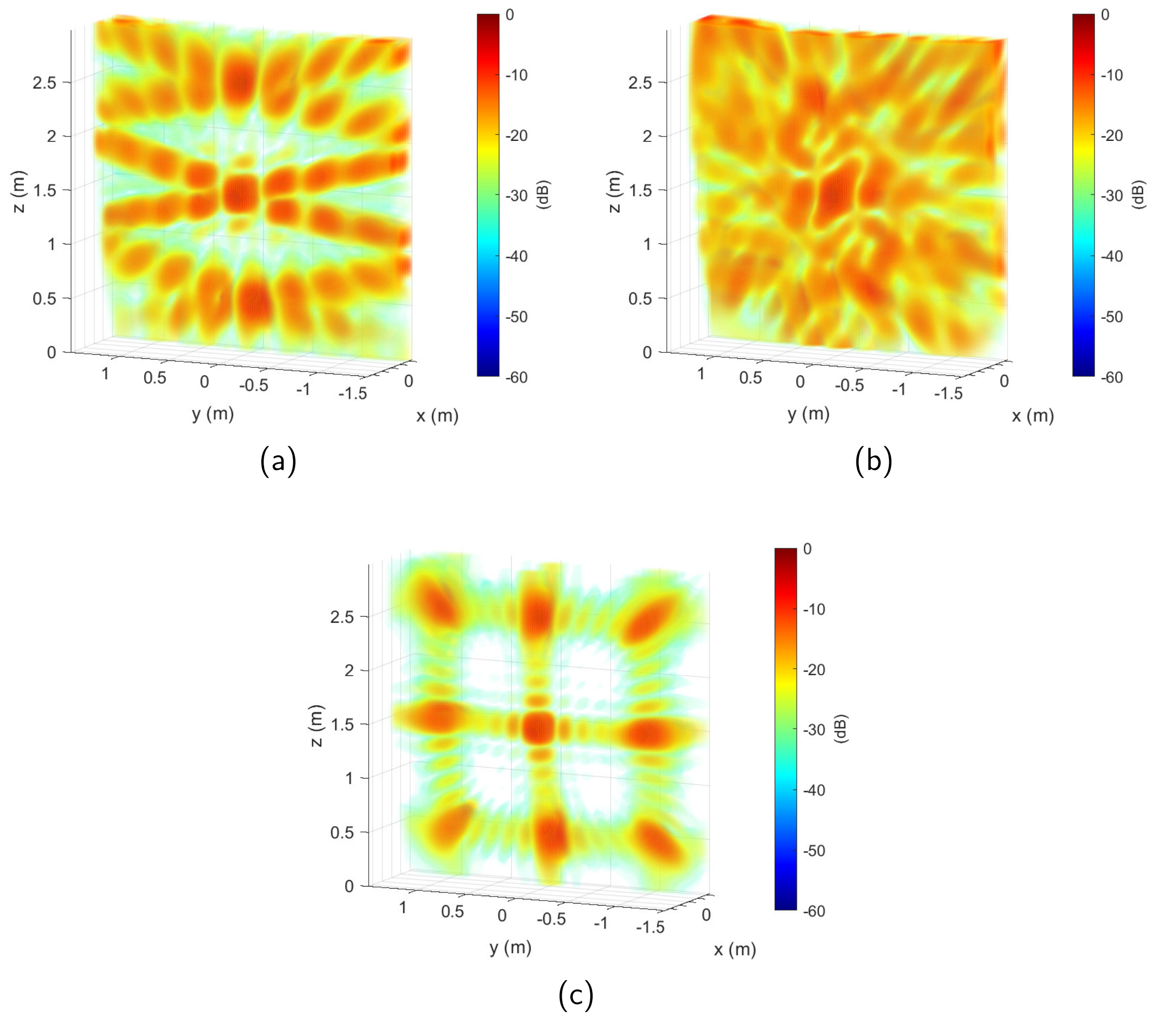

Figure 3.2. Simulated PSFs for (a) a zig-zag aperture, (b) an irregularly sampled aperture, and (c) a uniformly sampled aperture.

It was shown in this section that uniform sampling in the aperture domain generates grating lobes in an image, while irregular aperture sampling avoids grating lobes. Furthermore, even a pattern like the zig-zag aperture which is not periodic in the cross-range or vertical direction creates grating lobes. In the next section, the RSM technique is introduced. The RSM technique is used to remove sidelobes, but does not reduce grating lobes. It will be applied to the images presented here, and the results are analyzed.

3.2 Recursive Sidelobe Minimization

The RSM technique was designed to suppress multiplicative noise in SAR imagery. A point target is simulated at the origin using the linear aperture shown in Fig. 2.13. Fig. 3.3a shows an image of a point target formed using a randomly sub-sampled aperture, where 20% of the elements of the linear aperture are randomly removed. The image is formed in the ground plane without windowing to preserve the sidelobes for better visualization. The sidelobes in this image are elevated due to gaps in the aperture sampling, but the target response is unchanged despite these removed samples. Fig. 3.3b shows an image formed using a different randomly sub-sampled aperture. These two images highlight the fundamental principles underlying the RSM technique. First, the target response is coherently integrated and normalized, so the choice of random subsets do not change it. Second, energy is added noncoherently outside the target location in the image to form sidelobes. These sidelobes change depending on the aperture points used to form the image. Since the target response remains the same while the sidelobes change, a minimum can be taken between the two images at each pixel which preserves the target response and reduces sidelobe energy. Fig. 3.3c shows the resulting minimum between the two images. The sidelobes in this figure are slightly lower than in the other two images. To make this algorithm effective, hundreds or thousands of iterations are required.

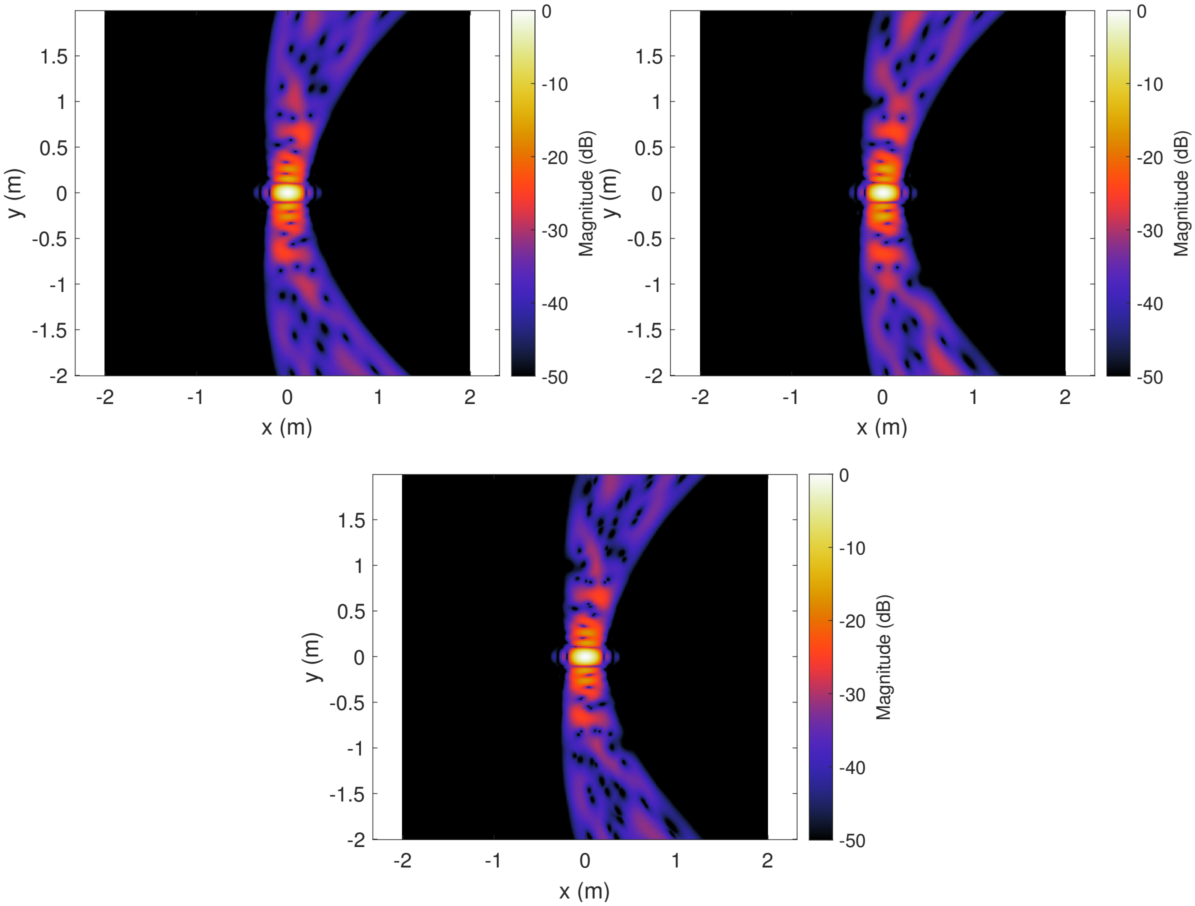

Figure 3.3. Images formed using (a) a random subset of a linear aperture, (b) a different random subset of a linear aperture, and (c) the minimum between the two images.

The steps of the RSM are as follows:

1. Radar data are collected over L frequencies at M aperture positions;
2. An initial image I_1 is formed on a set of N image cells, using all M aperture positions;
3. The RSM image Im_q is initialized as $\mathrm{Im}_1 = I_1$;
4. A random subset of the aperture is selected, and used to form an image I_2;
5. The RSM image for Iteration 2 is set by $\mathrm{Im}_2 = \min\left(\mathrm{Im}_1, I_2\right)$;
6. This process is repeated for Q iterations, where at each iteration a random subset of the aperture elements is selected and used to form the image I_q. Then, the next image is found by taking $\mathrm{Im}_q = \min\left(\mathrm{Im}_{q-1}, I_q\right)$.

The RSM algorithm is applied to the apertures in Fig. 3.1 using completely random subsets of the aperture. Fig. 3.4 shows the PSFs after 2000 iterations of the RSM. Although a majority of the sidelobes in each image have been removed non-target responses are still visible in the image obtained with the periodic aperture. An important result is that the random aperture does not have any remaining artifacts after application of the RSM algorithm. The reason for this difference is that the artifacts in the image formed by the periodic apertures are a combination of sidelobes and grating lobes, whereas the image created by the random aperture only contained sidelobes. This distinction is important because the RSM algorithm applied to a uniform aperture cannot remove grating lobes. **The combination of pseudo-random aperture sampling and the RSM technique can be used to generate sparse images with minimal artifacts.**

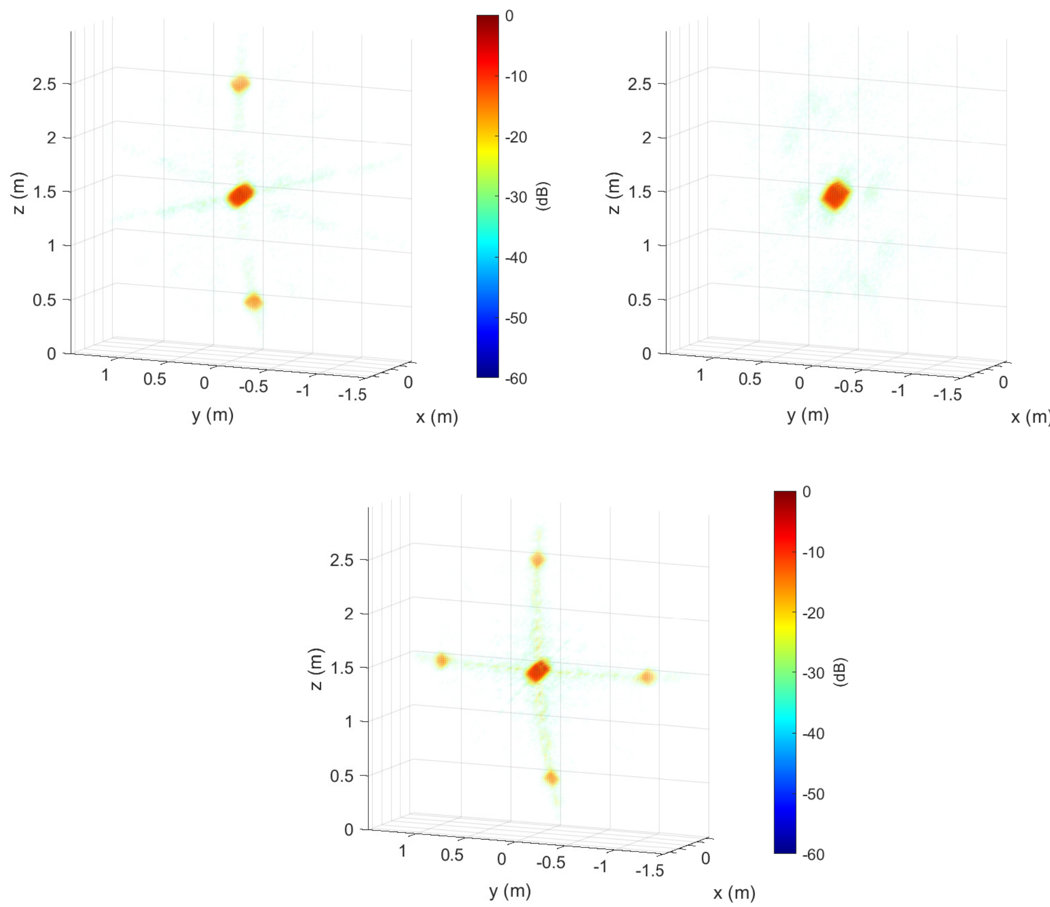

Figure 3.4. PSFs after 2000 iterations of RSM for a) a zig-zag aperture, b) a random aperture, and c) a periodic aperture.

3.2.1 RSM Subaperture Selection

The RSM algorithm can be computationally intensive, particularly as the number of aperture samples and the image size increase. For an aperture containing M samples, one can form $2^M - 2$ possible subapertures, in which each sample is either selected or left out. Thus, a 24-element aperture has 16,777,214 subapertures. This is too large to allow the application of every combination of subapertures through the RSM algorithm, so it is important to find a method of selection that can produce the largest improvement in image quality for a given number of iterations.

To determine valuable subsets of the aperture, the image quality is assessed at each iteration of the RSM algorithm. Two metrics are used to determine image quality. The first metric is the peak artifact (PA), which measures the ratio of the target peak to the peak artifact. This measurement is an indicator of grating lobes. The second metric is the mean artifact (MA), which measures the mean artifact in the image referenced to the target peak. The MA finds the general sidelobe level throughout the image. To calculate these metrics, the image is split into two regions: the target region and the artifact region. The target region is estimated by an ellipsoid whose radiuses are given by the PSF resolution in each direction of Eq. (2.18). The ellipsoid is given by

$$\frac{(x - x_{\o})^2}{\delta_x^2} + \frac{(y - y_{\o})^2}{\delta_y^2} + \frac{(z - z_{\o})^2}{\delta_z^2} = 1. \tag{3.1}$$

The responses outside the ellipsoid are considered imaging artifacts. The MA for the three apertures above are plotted over 2000 RSM iterations in Fig. 3.5. The image associated with the periodic aperture had the best MA at −56.7 dB, the image resulting from the zig-zag aperture had the second best MA at −55.0 dB, and the image formed using a random aperture had the worst MA at −54.2 dB. This is explained by the fact that sidelobes are increased by irregular sampling. The uniformly sampled aperture generated the image with the lowest MA, but the image has four grating lobes. Grating lobes have a negligible effect on MA because their response is only present in a small fraction of the total number of image voxels. The image formed using a zig-zag aperture also has grating lobes but a better MA than the image formed using a randomly sampled aperture. Grating lobes generate false alarms and cannot be ignored in characterizing a set of SAR parameters, so a metric for indicating grating lobes most also be used.

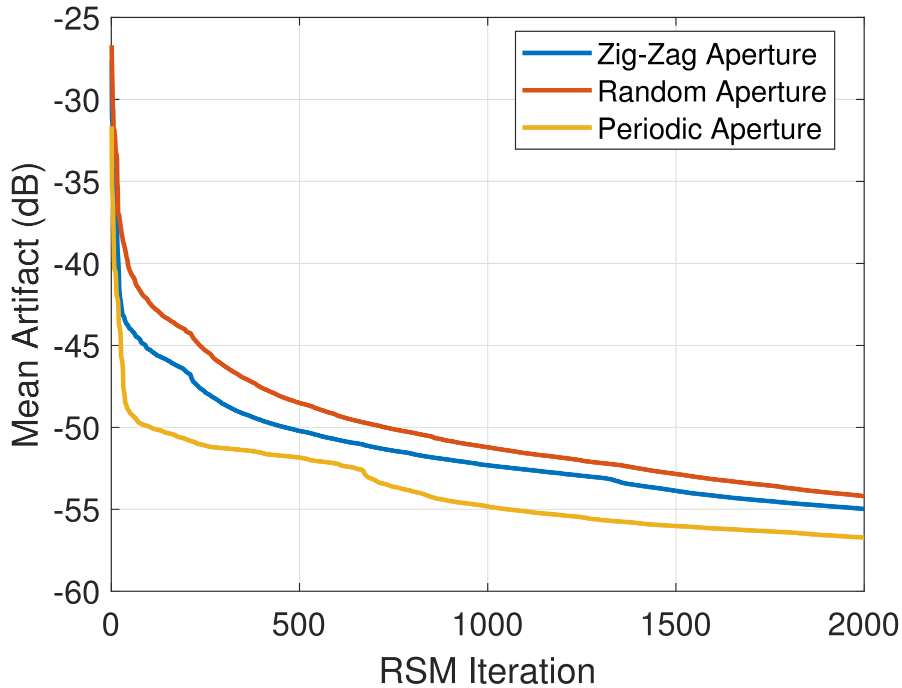

Figure 3.5. The MA plotted for the zig-zag aperture, the random aperture, and the periodic aperture.

The PA, which measures the peak artifact power referenced to the peak of the target, is useful for detecting grating lobes. The PA for the three apertures in Fig. 3.2 are plotted over 2000 RSM iterations in Fig. 3.6. The image generated using a randomly sampled aperture had the best PA, with a value of -23.2 dB. The PA was about -11 dB in the images formed using zig-zag and periodically sampled apertures, indicating the presence of grating lobes.

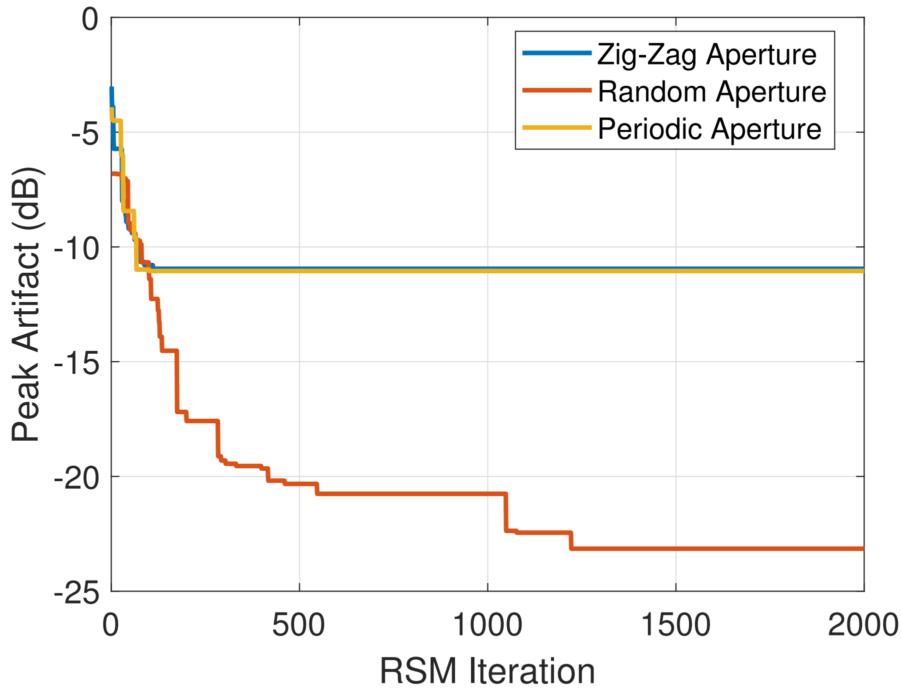

Figure 3.6. The PA plotted for the zig-zag aperture, the random aperture, and the periodic aperture.

It should be noted that, as opposed to the MA, the PA is not strictly decreasing. The PA only decreases when the peak artifact is reduced specifically, which requires the placement of a null at or near the peak artifact. This may only occur for a small set of subapertures, so the PA is often constant until one of those specific subapertures is selected.

The MA and PA are be used in conjunction to characterize the quality of an image based on its artifacts. By tracking these metrics at each RSM iteration, it can be determined which subapertures improve the image quality the most. A set of simulations using the RSM technique are performed, where the subapertures are grouped by number of elements. Group 1 has all one-element subapertures, Group 2 has all two-element subapertures, and so on. This is tested for the 10-element aperture shown in Fig. 3.7. The extents of the aperture are $A_y = 0.457$ m and $A_z = 0.5$ m.

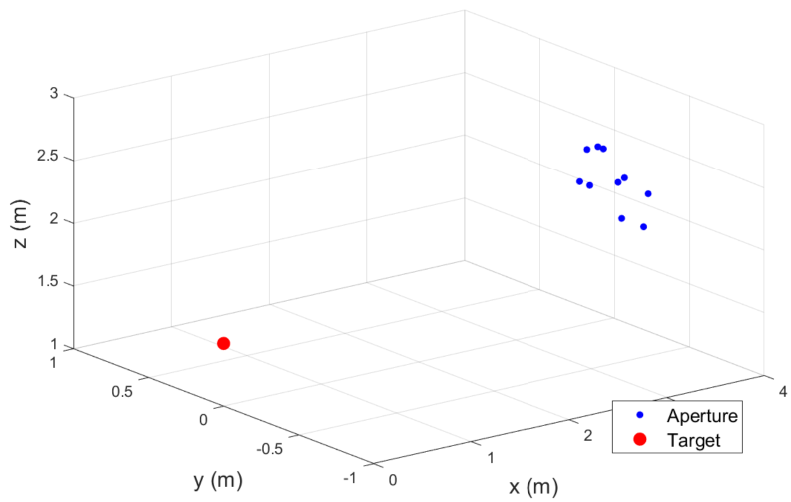

Figure 3.7. Ten-element random aperture.

The set of all subapertures is split into groups containing every subaperture of a given length. Group 1 contains all $\binom{10}{1} = 10$ single-element subapertures, Group 2 contains all $\binom{10}{2} = 45$ two-element subapertures, and so on, where $\binom{n}{k} = \frac{n!}{k!(n-k)!}$. Group 10 is excluded. An RSM simulation is performed separately for each group of subapertures. The mean ambiguity is plotted in Fig. 3.8. The plots are split into two graphs to avoid overcrowding. The MA increases most quickly in the lowest group and most slowly in the highest group. This shows that the number of elements used in the subapertures should be minimized to improve the speed of improvement when using the RSM technique. It should be noted that the most total improvement occurs from Group 4.

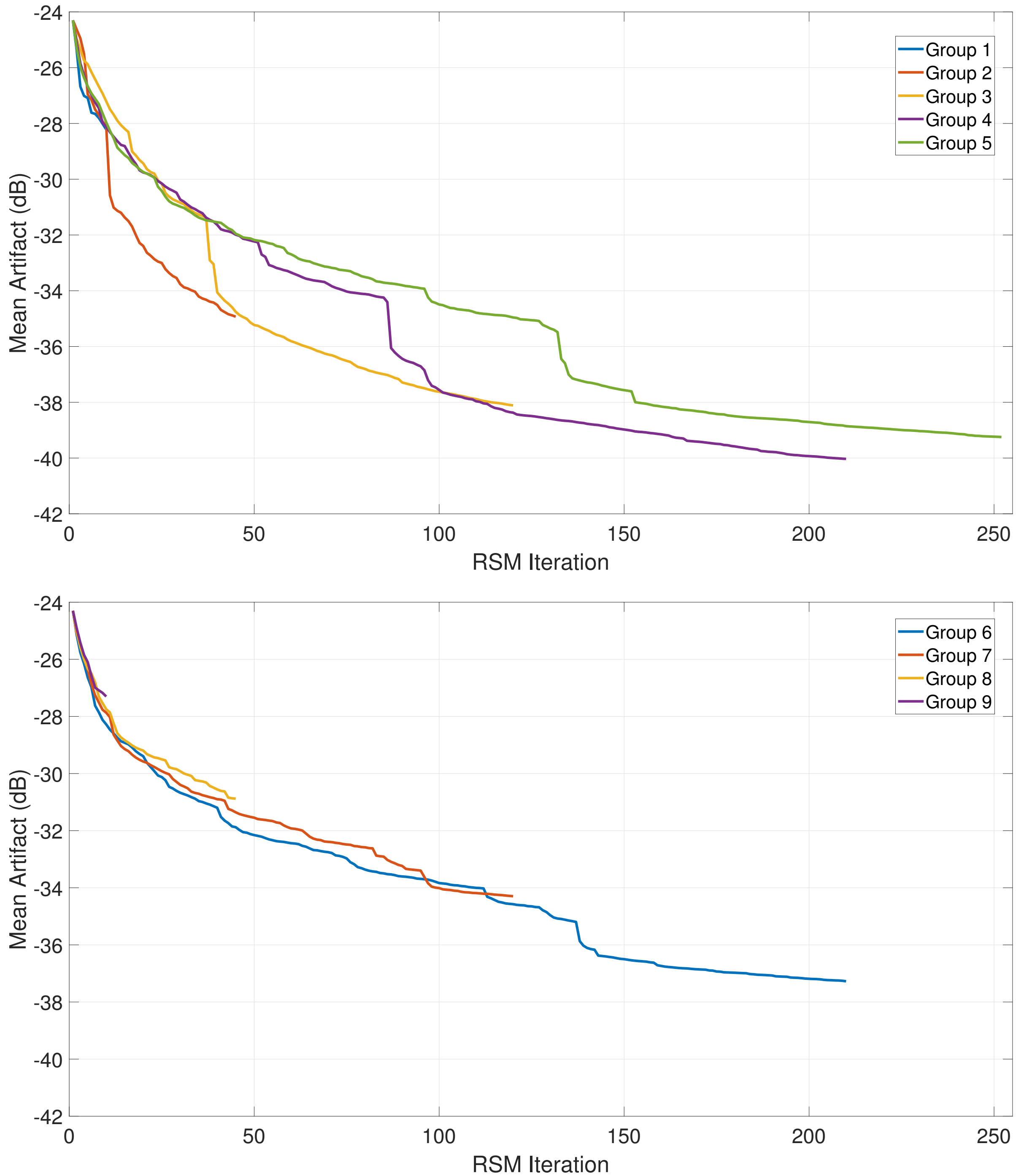

Figure 3.8. Mean ambiguity plotted for each group of subapertures: (a) subaperture groups 1–5 (b) subaperture groups 6–9.

Next, the PA is plotted in Fig. 3.9. Group 1 did not improve the peak response at all. However, for Group 2 and beyond, the PA did not improve as much as the number of elements increased. Thus, lower groups had the biggest impact on reducing grating lobes.

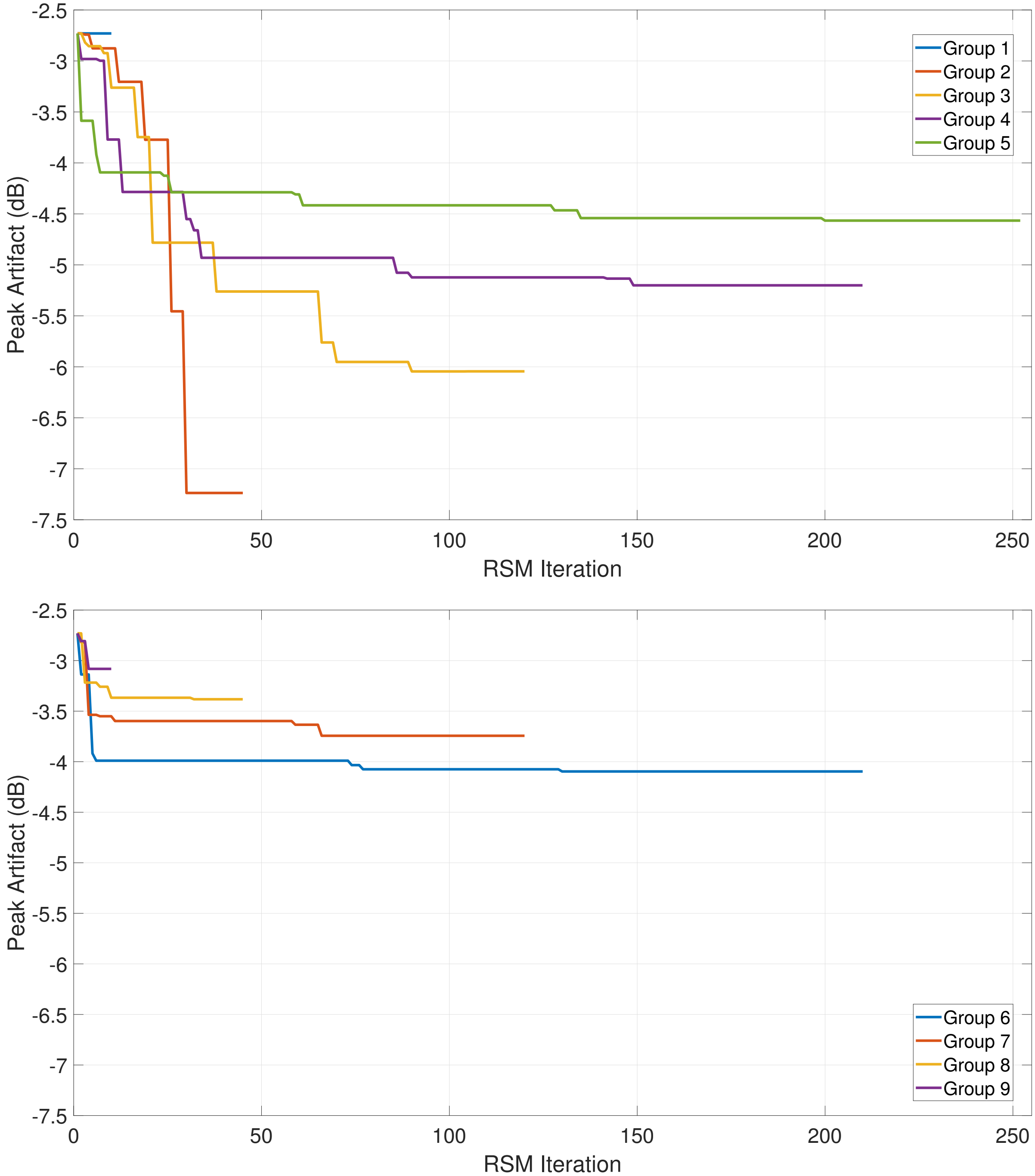

Figure 3.9. Peak ambiguity plotted for each group of subapertures: (a) subaperture groups 1–5 (b) subaperture groups 6–9.

The low-element subapertures had the fastest improvement to the image. To improve the speed of the RSM technique it is proposed that subapertures containing the minimum number of elements be prioritized. For the fastest convergence, the subelements should be selected in order of group. In the proposed method, all subapertures from Group 1 are used, then all subapertures from Group 2, and so on. This is tested in a simulation against a random selection of subaperture elements. A comparison of the MA and PA using the organized method of subaperture selection and the random method of subaperture selection are plotted in Fig. 3.10. The organized method leads to a faster rate of convergence. The set of subapertures is finite, so eventually these two methods result in the same image. However, as the number of elements in an aperture increases, the number of subapertures becomes large and it would be too computationally inefficient to use every subaperture. For this reason subaperture selection is important.

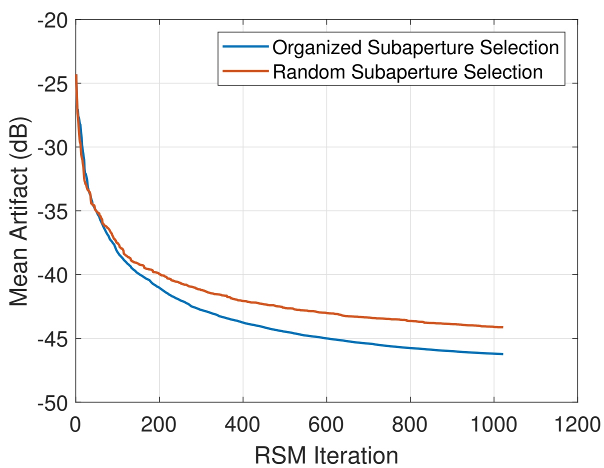

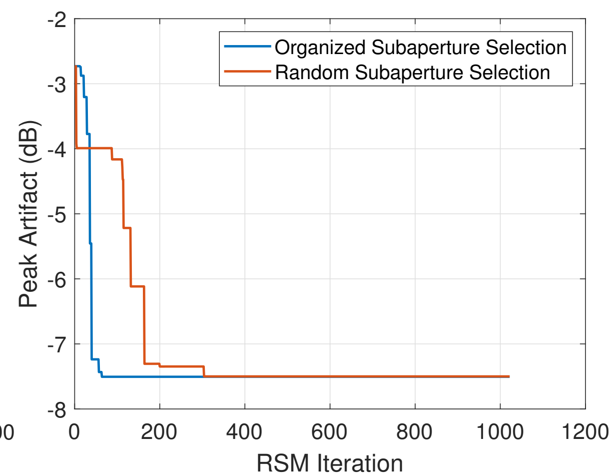

Figure 3.10. Comparison of (a) MA and (b) PA using organized and random subaperture selection in the RSM algorithm.

In this section, metrics were presented for analyzing the quality of an image. These metrics were used to determine the collections of subapertures that led to the biggest improvement in image quality during the RSM algorithm. It was determined that subapertures with the least number of elements removed sidelobes more quickly. Furthermore, it was shown that low-element subapertures decreased the power of grating lobes the most. Subapertures with one element were an exception to this rule, as they had no effect on the strongest grating lobes. A new method of RSM subaperture selection was presented that organized subapertures based on the the number of elements, prioritizing low element numbers. It was shown that this method of subaperture selection led to better image quality metrics in fewer RSM iterations. This method will be crucial for apertures with more elements where it is not feasible to use all combinations of subapertures.

3.2.2 Monte Carlo Simulation

The irregularly sampled aperture presented in Fig. 3.1 provides anecdotal evidence that random apertures can be paired with the RSM algorithm to generate imagery with minimal artifacts; however, there is a variance between images formed using different random apertures. The demonstration of this technique on a single instantiation of a random aperture does not guarantee the effectiveness of this technique for any given random aperture.

A Monte Carlo simulation was performed to generalize the performance of this technique for the set of randomly sampled, twenty-element aperture within a 1×1 m plane. In the following simulation, aperture samples are randomly selected from a uniform grid with 6 mm sample spacing in both the y- and z-directions. Fig. 3.11 shows the grid aperture of potential sample points, a randomly sampled twenty-element aperture, and a point target.

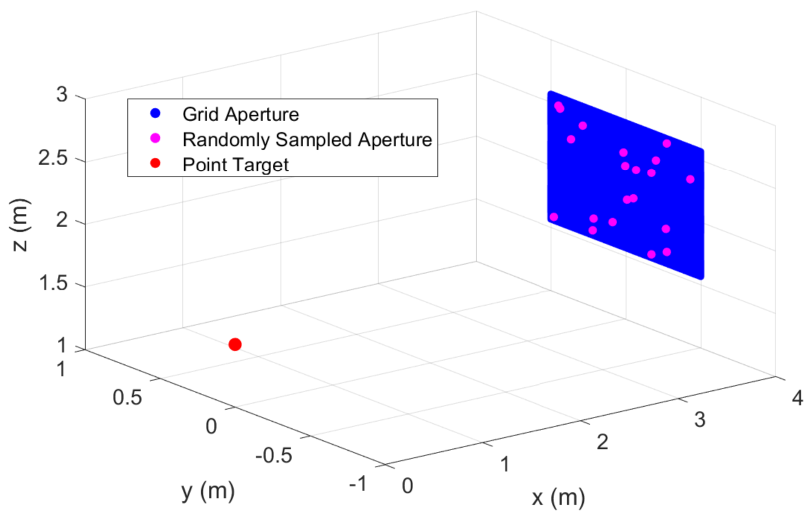

Figure 3.11. A grid aperture of potential sample points, a randomly sampled, twenty-element aperture, and a point target.

For each random aperture, an image is formed and 2000 RSM iterations are performed. The PA is calculated for each aperture at each RSM iteration to determine the performance of each aperture. From these values, the maximum, mean, and minimum PA at each RSM iteration are determined to provide an estimate and bounds of performance given twenty aperture elements sampled in a 1×1 m grid.

The PA for each aperture is plotted in Fig. 3.12a. In Fig. 3.12b, the minimum, mean, and maximum of the PA over all apertures are plotted at each iteration of the RSM technique. The mimimum and maximum PA represent the best and worst cases, respectively. The mean is used to estimate performance given a number of elements. The maximum PA in this case is -16.3 dB. This is an outlier from the general trend; however, this demonstrates that a collection of randomly sampled aperture points exists for which this technique is not effective. The mean PA after 2000 iterations is -23.4 dB. This result shows that, on average, this technique effectively removes artifacts. The minimum PA is -26.3 dB.

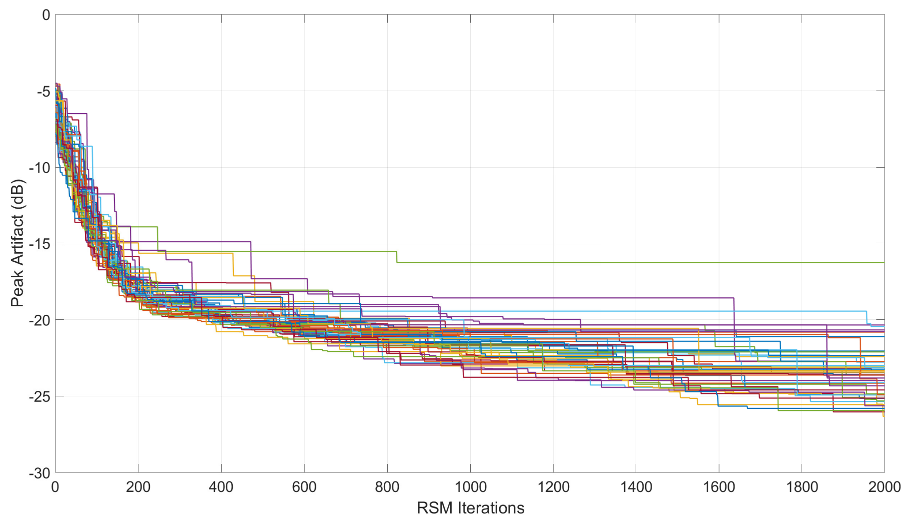

(a)

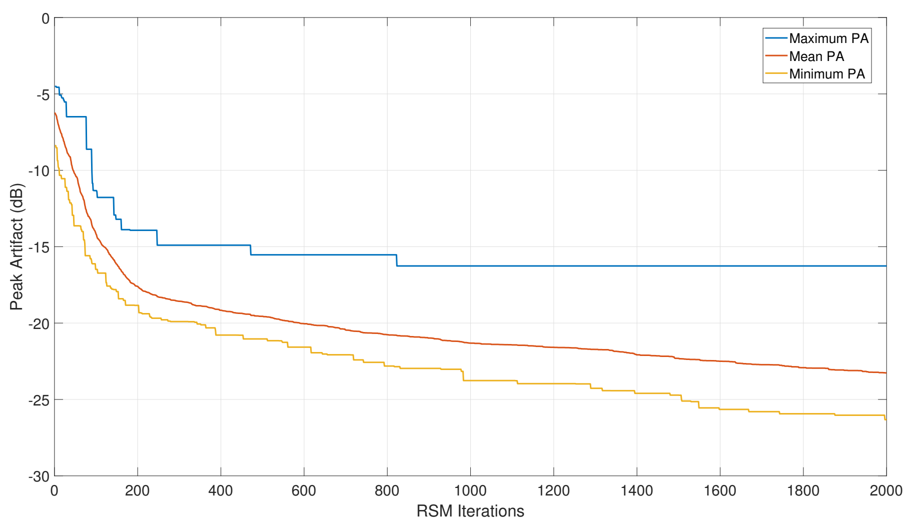

(b)

Figure 3.12. (a) PA from 50 Monte Carlo simulations with twenty-element apertures. (b) Maximum, mean, and minimum PA for a Monte Carlo simulation using random twenty-element apertures.

To demonstrate the importance of aperture sample density, this Monte Carlo simulation was repeated using randomly sampled apertures with fifteen elements. The minimum, mean, and maximum are plotted in Fig. 3.13. The maximum PA from the fifteen-element simulation is much higher than that of the twenty-element simulation. The mean PA of the 15-element simulation is also higher, which confirms that, generally, this technique performs better when using apertures with higher element densities. An interesting result is that the minimum PA is lower in the fifteen-element simulation. This demonstrates the variance in performance that is present when randomly selecting elements. Increasing the sample density does not guarantee better PA performance. However, on the average, a larger number of aperture samples does provide lower artifact levels in the RSM-processed image.

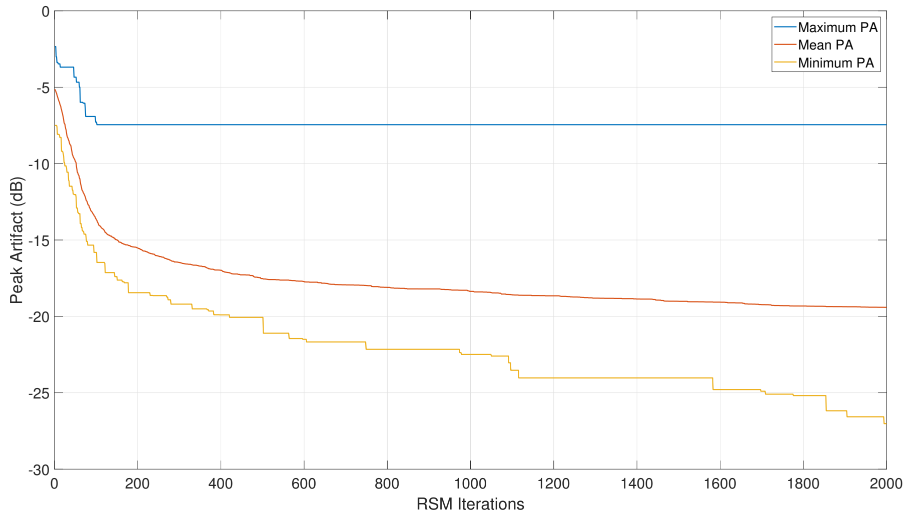

Figure 3.13. Maximum, mean, and minimum PA for a Monte Carlo simulation using random fifteen-element apertures.

3.3 Model Data

In Section 3.2, it is demonstrated that a sparse pseudo-random aperture can be paired with the RSM technique to produce imagery with minimal artifacts. This was demonstrated using a point target. The problem is more complicated in the case of extended targets. One new development is the presence of additional scattering centers. The previous simulations were performed on a point target, which consists of a single scattering center. In modeled data, the target response is dependent on practical effects such as target radar cross-section (RCS), target range, and antenna pattern. The inclusion of physical phenomenology in the simulation impacts the ability of the algorithm to remove imaging artifacts without affecting the target response.

A model was generated using the AFDTD software [43] to test if the RSM technique using random apertures can be applied to extended targets. A metal cylinder with a diameter of 0.3 m and a height of 0.15 m is simulated at $(x, y, z) = (0.15, 0.5, 1.5)$ m. Data are simulated for the frequency band from 2.2 to 3.7 GHz with a 15-MHz frequency step size. Data are simulated for random and periodic apertures. The random aperture is a set of x points sampled from a grid aperture, where $x_m = 4$ m, $y_m \in [-1.5, 1.5]$ m, and $z_m \in [1.4, 2.6]$ m. The periodic aperture has $x_m = 4$, m, $y_m \in [-1.08, 1.78]$ m, and $z_m \in [1.53, 2.58]$ m. The spacing of the periodic aperture samples is $\Delta y = 0.71$ m and $\Delta z = 0.35$ m. The data are simulated using horizontal dipoles for radar antennas placed in a quasi-monostatic configuration. The apertures and the target are plotted together in Fig. 3.14.

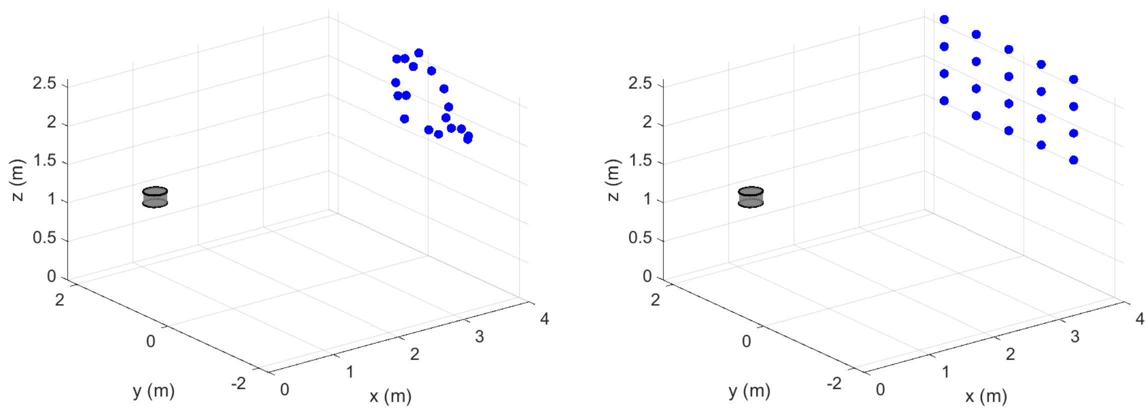

Figure 3.14. (a) Random aperture and (b) periodic aperture with target overlaid.

A 2-D image in the plane $z = 1.5$ m formed using a fully populated linear aperture is plotted in Fig. 3.15. The linear aperture is 2 m long, oriented in the y direction, with its center at $x_a = 4$ m and $z_a = 2.5$ m. The primary response results from the target, whereas the secondary responses result from creeping waves, which travel around the circumference of the target before traveling back to the radar. This image is used as a baseline for comparison with the simulated 3-D images. The responses present in this image result from modeled electromagnetic phenomena. Responses that occur in the 3-D image that do not coincide with the responses in this image are considered imaging artifacts. The landmine is overlaid on the picture in translucent light green.

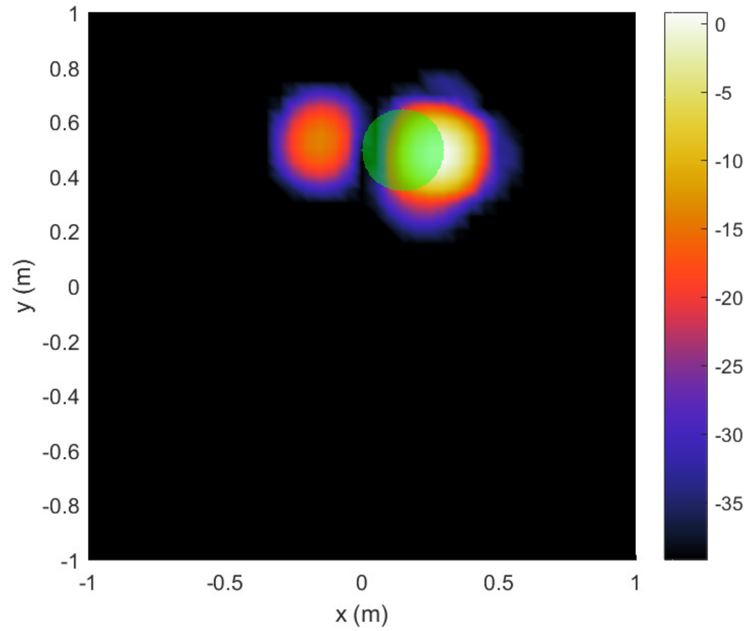

Figure 3.15. Image of a short metal cylinder formed using a linear aperture. The target contour is represented by the green circle.

The images of the cylinders using the random and periodic apertures without RSM are shown in Fig. 3.16. The energy is more randomly dispersed in the image generated using the random aperture, whereas the energy focuses at periodic intervals in the image generated using the periodic aperture. These images confirm that the random aperture produces large sidelobes, whereas the periodic aperture produces grating lobes.

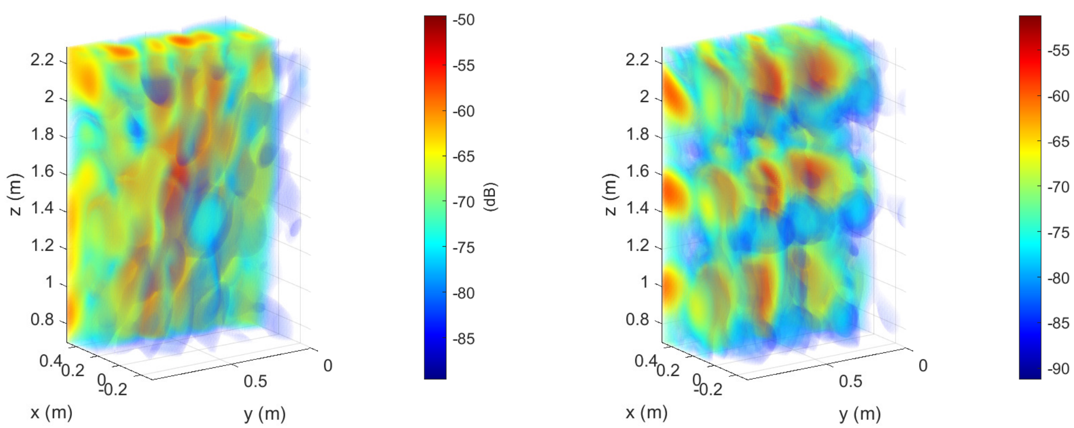

Figure 3.16. Images using standard SAR imaging with (a) a random aperture and (b) an undersampled periodic aperture.

First, the recursive sidelobe minimization algorithm is demonstrated. Fig. 3.17 shows the previous images after 2000 iterations of RSM. RSM completely removes the sidelobes from the image formed using the random aperture. In the image formed using the periodic aperture, the sidelobes are removed, the grating lobes are still present at a spacing of $\Delta y = 0.280$ m and $\Delta z = 0.555$ m. According to the PSF formed using a grid aperture the grating lobe spacing would be $\Delta y = 0.272$ m and $\Delta z = 0.556$ m. Thus, the analytical PSF expression accurately predicts the grating lobe spacing. These images confirm through modeling that by using a random aperture we can ensure that artifacts in the image are sidelobes, which can be removed using the RSM algorithm. The resolution of the two images is also different due to different aperture extents, hence the target appears larger in the random aperture.

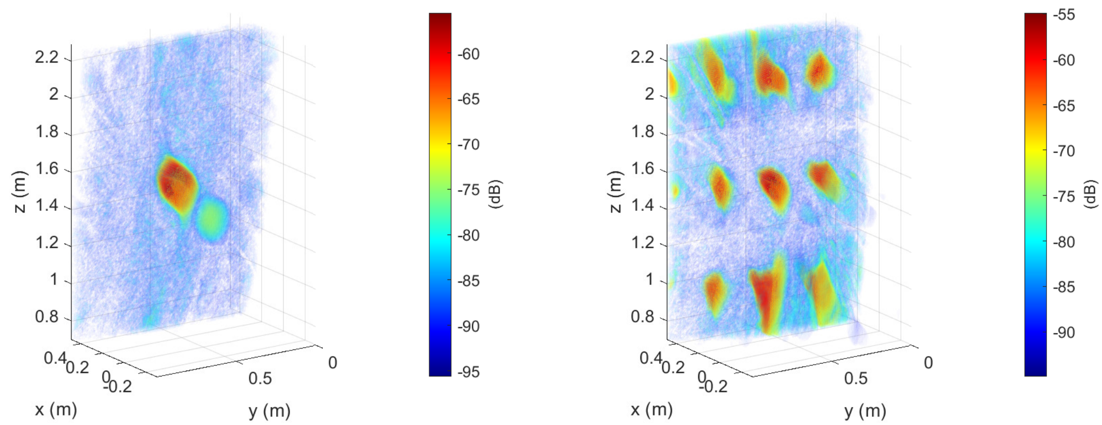

Figure 3.17. Images of a metal cylinder in HH polarization after 2000 iterations of RSM generated using (a) a random aperture and (b) a periodic aperture.

The peak artifact is plotted in Fig. 3.18. The peak for the image formed using a random aperture drops to 19.6 dB, while the peak artifact in the image formed using the periodic aperture is 3.5 dB. The PA shown below is not monotonic, in contrast to the PAs shown in Section 3.2. This discrepancy results from the inclusion of signal amplitude characteristics in the model data. The target response magnitude varies at each aperture sample due to differences in path loss, radar cross section (RCS), and antenna gain. Images formed using different subapertures have different peaks based on these factors, which can reduce the peak in the image. When the peak image value decreases but the peak artifact value does not, then the PA increases. The MA will also increase if the peak image value decreases more than the mean artifact power. The PA and MA are also non-monotonic when using experimental data. In Section 3.2, the signals have unit amplitude at all aperture samples, so the peak never changes.

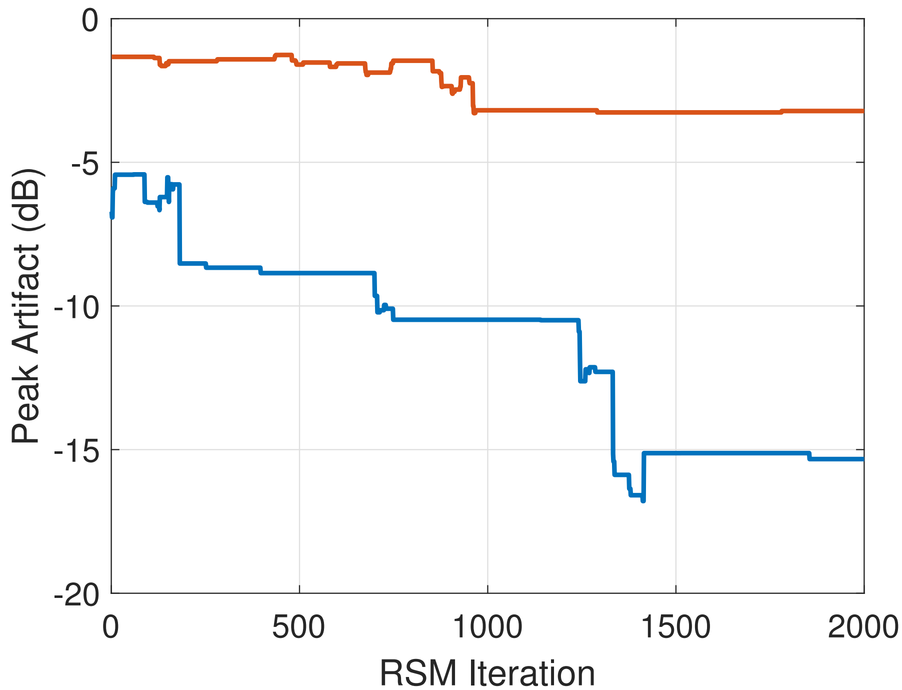

Figure 3.18. Peak artifact plotted at each RSM iteration for the images of a metal cylinder formed using the random and periodic apertures.

The modeled data include magnitude information that was ignored in the point target response considered in Section 3.2 . The radar range equation describes the factors that affect the received power of a bistatic system [39]:

$$P_r = \frac{P_t G_t G_r \lambda^2 \sigma}{(4\pi)^3 R_t^2 R_r^2}. \tag{3.2}$$

where P_t is the transmitted power, G_t is the gain of the transmit antenna, G_r is the gain of the receive antenna, λ is the wavelength at the center frequency of the transmitted band, σ is the RCS of the target, r_t is the range from the target to the transmit antenna, and r_r is the range from the target to the receive antenna. In this model, the antennas are assumed to be monostatic. The antennas also have the same gain, which is a function of frequency and look angle. This allows for the simplification $G(f_l, \Theta) = G_t = G_r$. Second, the RCS of the target is a function of both frequency and look angle, so it is denoted by $\sigma(f_l, \Theta)$. Finally, the transmit and receive ranges are approximately equal: $r \approx r_t \approx r_r$. The resulting receive power is

$$P_r = \frac{P_t G^2(f_l,\Theta)\lambda^2\sigma\,(f_l,\Theta)}{(4\pi)^3 r^4}. \tag{3.3}$$

Thus, each aperture position will have a different receive power depending on the angle to the target, the range to the target, and the operating frequency. The received power from a given scattering center can vary greatly across the aperture. This is demonstrated in Fig. 3.19a. The left-most range profile shows the target from the lowest aperture positions, whereas the right-most range profile shows the target from the highest aperture positions. The response is strongest when the target is aligned with boresight of the antennas. As the aperture sample gets farther away from this position in cross-range, the power of the received signal decreases. The variation in magnitude is more drastic in the vertical dimension. The variation in the signal magnitude across the horizontal dimension is between 0.3 dB (at the top row of samples) and 2.3 dB (at the bottom row of samples), whereas the variation in the signal magnitude in the vertical dimension is 13.2 dB. The circular symmetry in the azimuthal dimension reduces the variation of the response from the target as a function of the horizontal aperture sample position. However, the target is not symmetrical in the vertical dimension, and the response is extremely angle dependent.

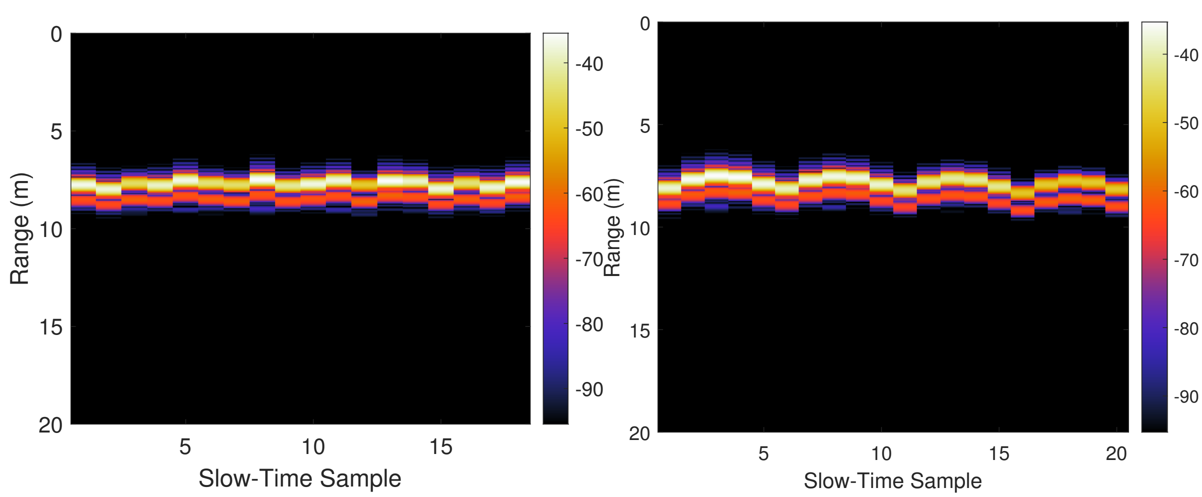

Figure 3.19. B-scan from (a) a random aperture and (b) a periodic aperture.

Another major challenge that results from the model data is the number of scattering centers. The simulations that were used to demonstrate this algorithm in Section 3.2 were performed on a point target, which consists of one scattering center. However, in real radar applications, targets contain numerous scattering centers leading to many different types of responses from a single target. Different scattering centers are stronger at different angles. The RSM operates by forming images with different subapertures and taking the minimum over many iterations. If different scatterers are emphasized at different angles, then the use of the full aperture can lead to a reduction in the strength of the primary scattering center. A strong coherent target response is important for detection. By reducing the aperture extent, the scattering centers of a target are grouped into a single resolution cell, reducing the risk of lowering the target peak.

Two random apertures are plotted in Fig. 3.20. A narrow aperture is compared with a wider aperture to demonstrate the effect of a wide aperture on the RSM algorithm. The first aperture has a horizontal extent of 1.596 m and a vertical extent of 0.933 m, while the second aperture has a horizontal extent of 4.603 m and a vertical extent of 1.4 m.

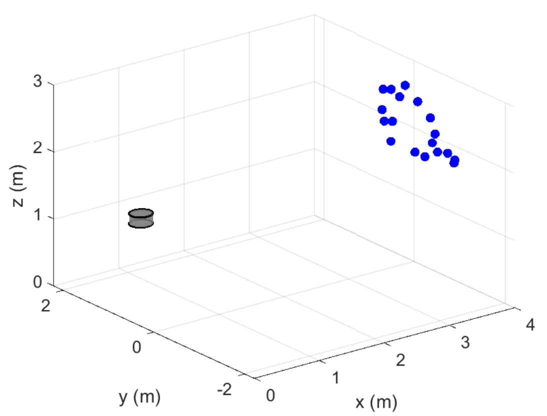

Figure 3.20. Two random apertures for comparison.

B-scans of a metal cylinder for these two apertures are shown in Fig. 3.21. The magnitude variation across the peaks of the bscans is 12.7 dB for the narrow aperture and 19.1 dB for the wide aperture.

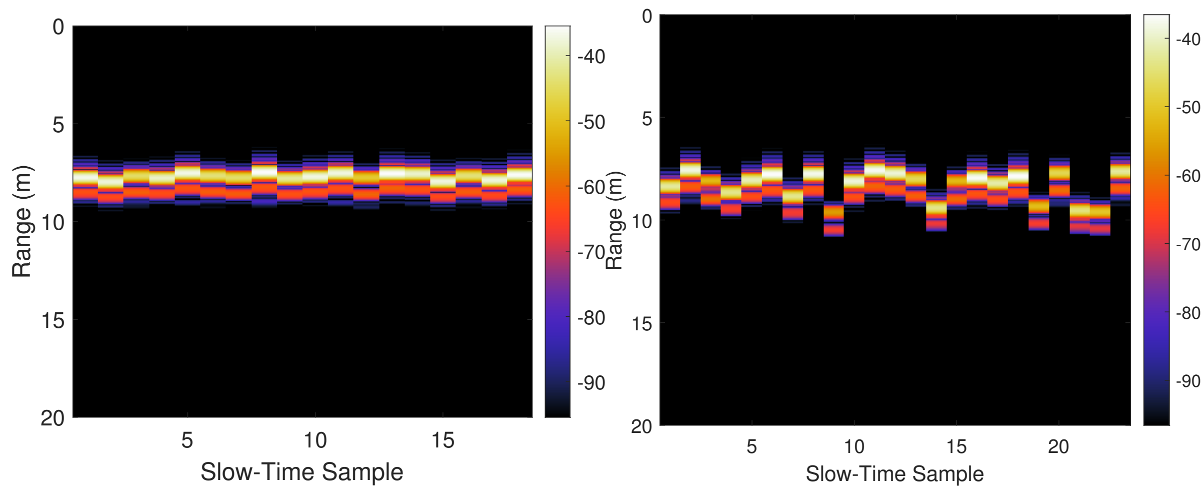

Figure 3.21. B-scans of metal cylinder for (a) a narrow random aperture and (b) a wide random aperture.

These variations in magnitude can reduce the peak magnitude as shown in Fig. 3.22. The images are comparable in terms of removing the artifacts. The image formed with a wider aperture has better resolution, but this image also has a lower target peak. Due to the lack of variation across the aperture samples, the narrow aperture better preserves the target response. The narrow angle has a peak of -0.2 dB, whereas the wide angle has a peak of -4.5 dB. The difference of 4.3 dB is inconsequential in an ideal environment with one target. However, in a practical image with discrete clutter, this would have a large impact on target detection.

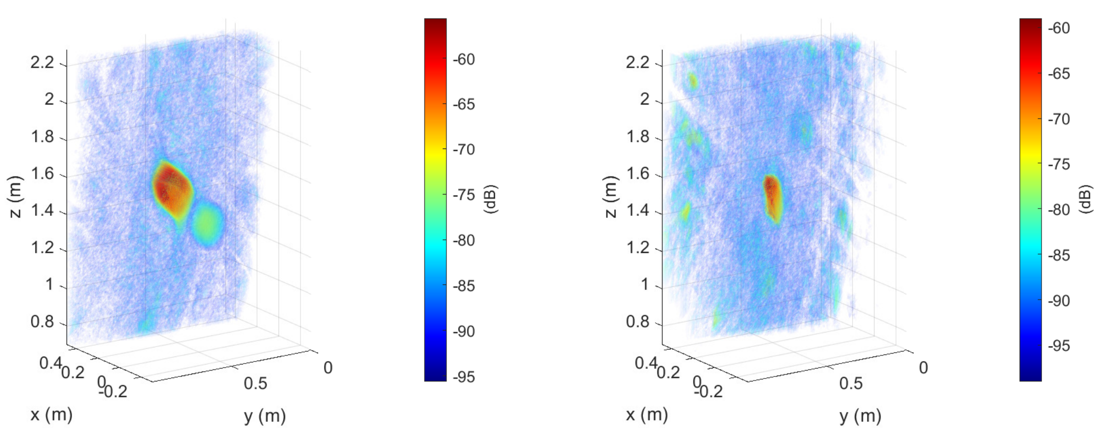

Figure 3.22. Image of a metal cylinder formed using (a) a narrow and (b) a wide aperture.

3.4 Experimentation

Practical experimentation presents the most difficult test to this technique. Any errors in the signal phase reduce coherence at the target. Also, interference between a target response and ambiguities can reduce the target response over thousands of RSM iterations. There are many sources of error in a practical experiment. These include system noise, antenna position estimate error, experimental calibration error, and ambient interference. Data from an experiment with a trihedral are used to verify this algorithm.

Fig. 3.23 shows a trihedral placed on a styrofoam block and a mechanical scanner that is used to collect radar data. The scanner is able to scan in the cross-range and vertical dimension. The antennas are vertically polarized and separated by 0.45 m in the cross-range direction. The x direction is across-track, the y direction is along track on the scanner, and the z direction is vertical on the scanner. The same radar hardware as in Section 2.5 is used. The trihedral is at the position $(x_{\text{tri}}, y_{\text{tri}}, z_{\text{tri}}) = (-0.06, -0.16, 0.88)$ m.

Figure 3.23. (a) Trihedral on a styrofoam block. (b) Scanning platform with antennas mounted.

Measurements were taken along a grid in the yz plane at $x = 4.3$ m. A representation of this grid is plotted in Fig. 3.24 using bistatic phase centers between the transmit and receive antenna elements. The bistatic phase center is the midpoint between these two elements in the aperture plane. This aperture has extents of $A_y = 6$ m and $A_z = 1.4$ m, and the sampling spacing is $\Delta y = 0.0012$ m and $\Delta z = 0.05$ m.

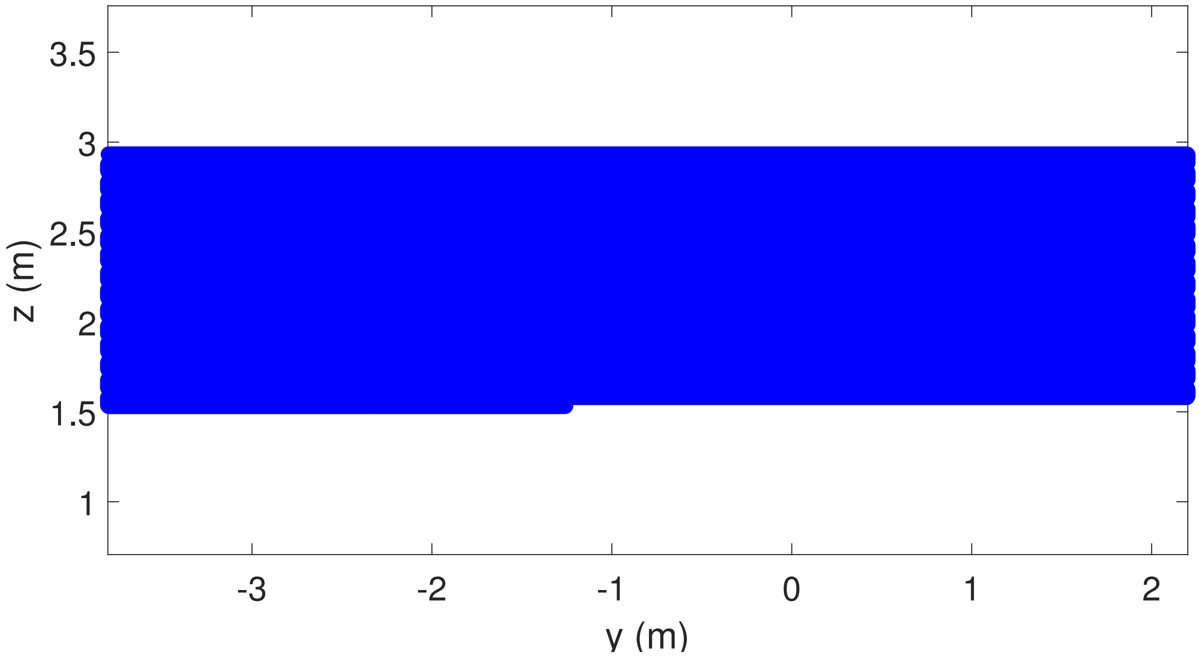

Figure 3.24. Bistatic phase centers from experimental data.

To form imagery, these data are downsampled to the desired aperture shape. First, an image is generated using a square 1-m-by-1-m grid. In terms of bistatic phase center, the center of this grid is at $(x_a, y_a, z_a) = (4.33, 0, 1.982)$ m. The resulting grid of bistatic phase center samples is plotted with a marker indicating the location of the trihedral in Fig. 3.25.

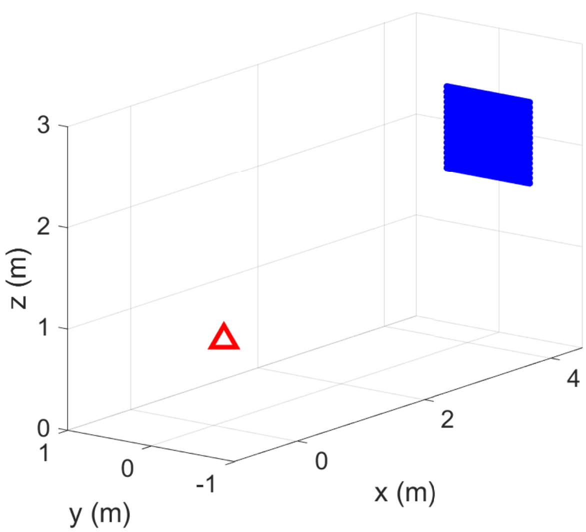

Figure 3.25. Grid aperture and measured trihedral.

The resulting image is shown in Fig. 3.26. No window is used to form this image, so there are sidelobes about 13 dB below the peak. This image shows that the imaging system has good coherence.

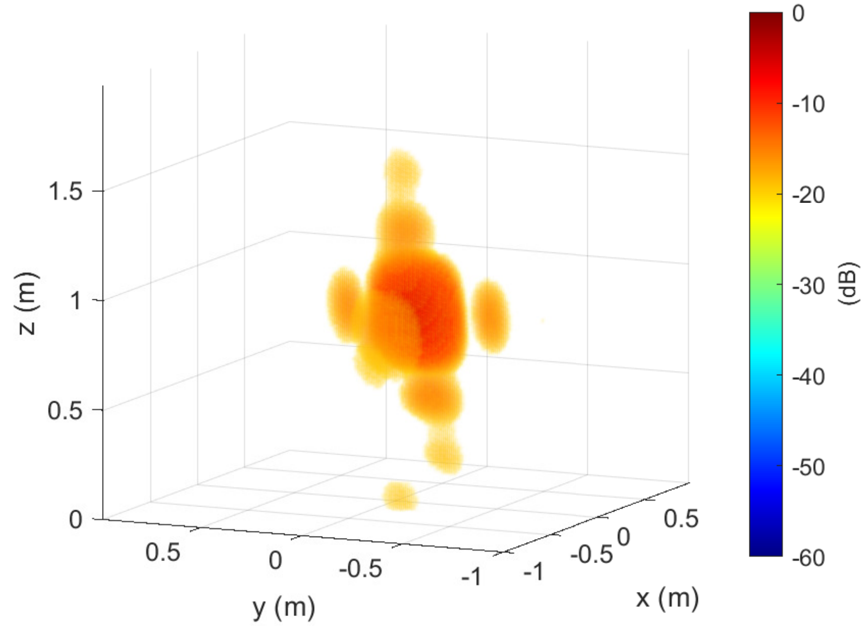

Figure 3.26. 3-D image of a trihedral formed using a grid aperture.

Next, a random aperture is tested. The random narrow aperture from Fig. 3.14 is used to select indices from grid aperture. This is accomplished by matching the aperture positions in the simulated aperture to bistatic phase center positions from the physical aperture. The antenna positions corresponding to those bistatic phase centers are then used to form the image. The bistatic phase centers corresponding to the simulated aperture are shown in Fig. 3.27.

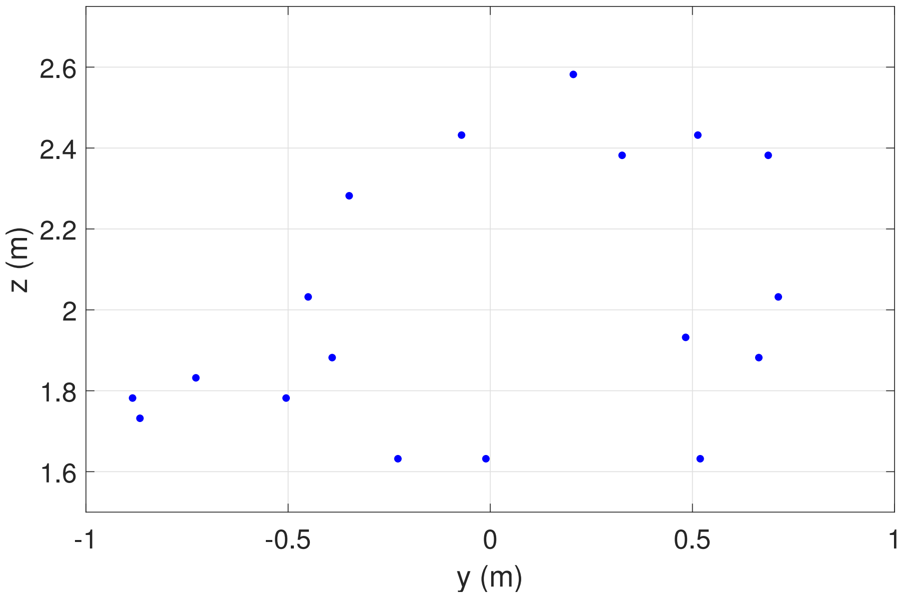

Figure 3.27. Random narrow aperture.

The image formed using this aperture with the RSM technique is shown in Fig. 3.28.

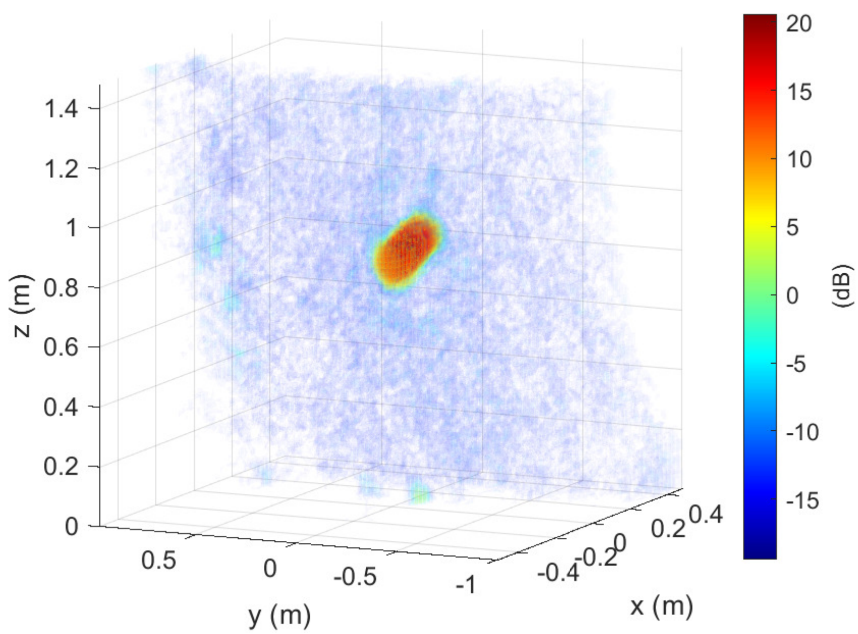

Figure 3.28. Image of a trihedral formed using a random aperture and the RSM algorithm.

The PA is plotted in Fig. 3.29. The grating lobes are successfully removed, with the peak artifact at −20.0 dB after iterating through. This confirms that sparse random apertures can be paired with the RSM algorithms to generate radar imagery free of artifacts.

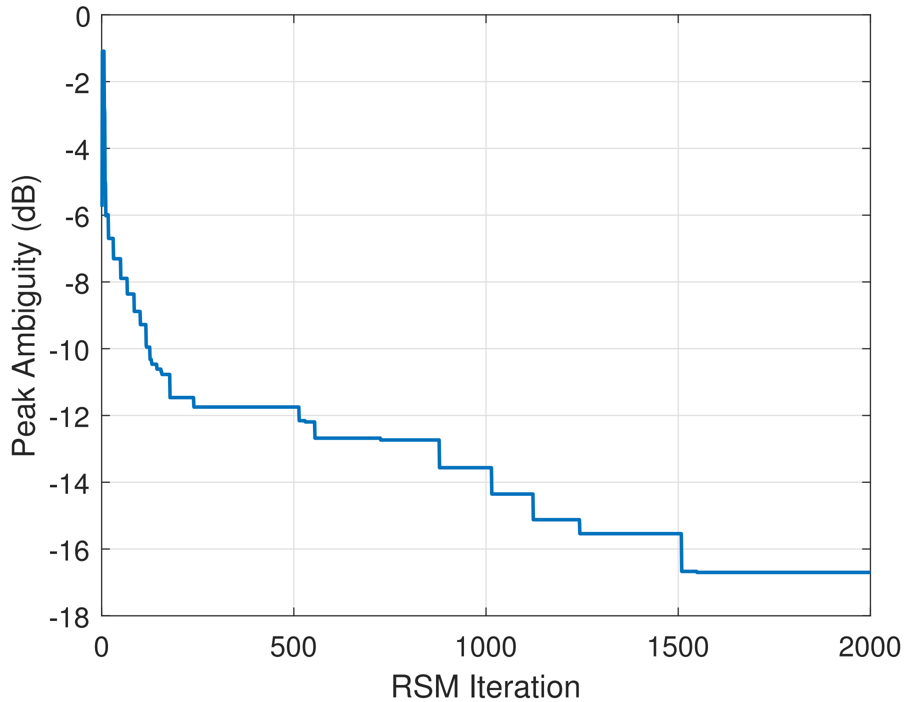

Figure 3.29. PA for image formed using random aperture.

Next, a wide random aperture is used. The plot of bistatic phase centers shown in Fig. 3.30 is derived from the aperture in Fig. 3.20b.

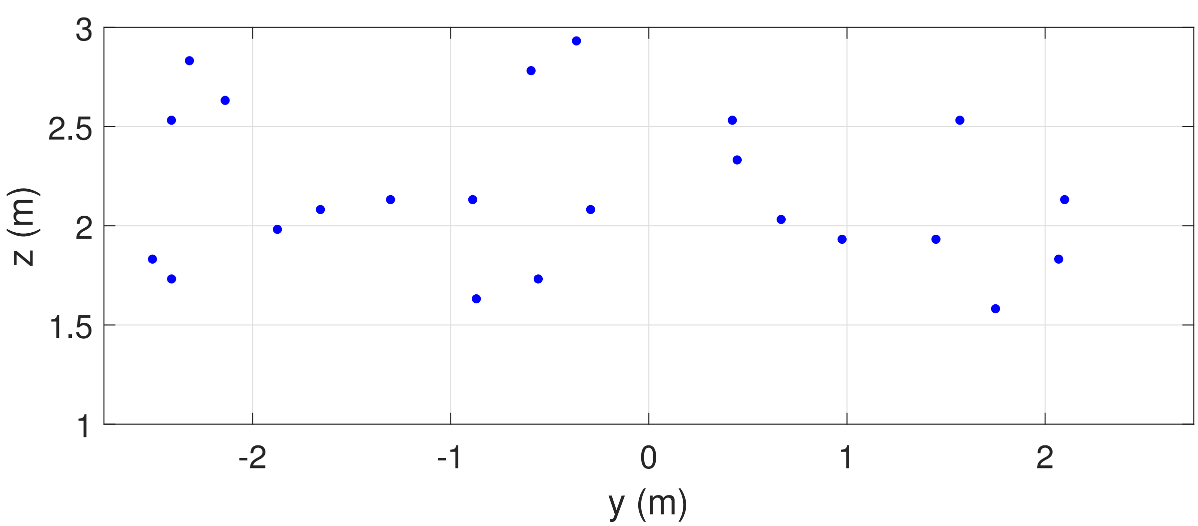

Figure 3.30. Wide random aperture.

The resulting image is shown in Fig. 3.31. In this image, the target is visible and there are minimal artifacts distributed around it after 2000 iterations of the RSM technique.

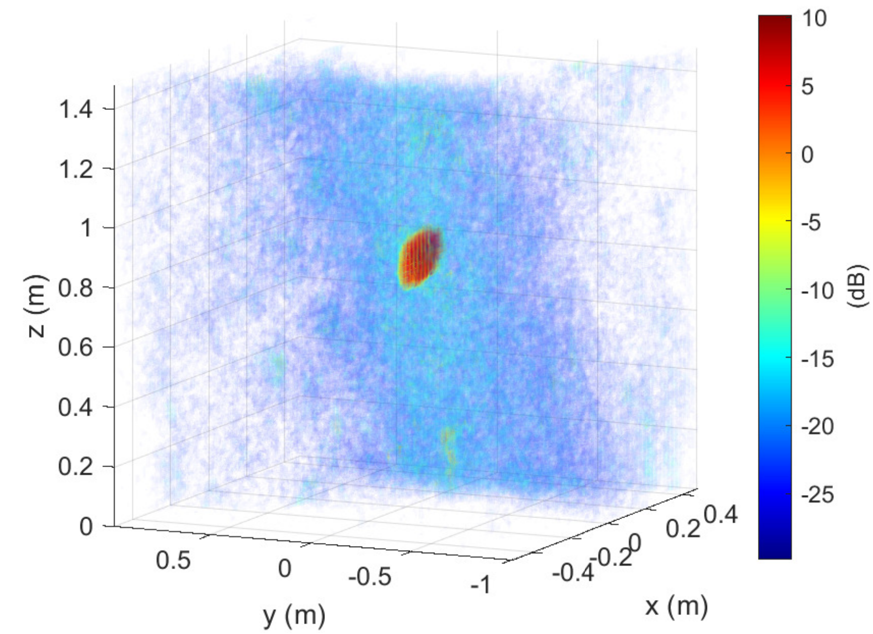

Figure 3.31. Image of trihedral formed using a wide random aperture and the RSM technique.

The PA is plotted in Fig. 3.32. The maximum ambiguity is 13.5227 dB below the peak, which is about the level of an unwindowed sidelobe. This is a reasonable sidelobe level; however, the peak has dropped 9.5096 dB below the original peak. This is a large degradation for the target. In a single scatterer case, the maximum pixel value is not important because it is not competing with other scatterers. However, in a more complicated scene, this may present problems for target detection.

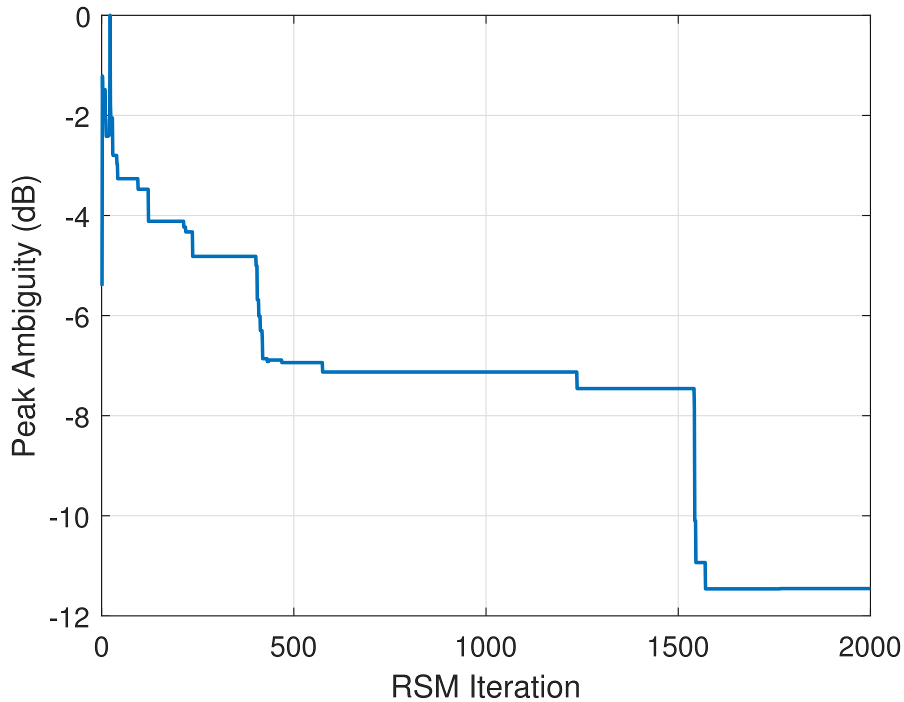

Figure 3.32. PA from an image formed using a wide random aperture with the RSM technique.

Chapter 4 Modified RSM: Center Frequency Randomization

In Chapter 3, it is demonstrated that an undersampled aperture that is periodically sampled generates imagery with grating lobes. The RSM technique cannot remove grating lobes, so a sparse periodic aperture cannot be paired with the RSM technique to generate unambiguous radar imagery. However, the relationship between center frequency and grating lobe spacing can be exploited to remove grating lobes in this case. In this chapter, a modification to the RSM technique is proposed that allows for the use of a periodic, undersampled aperture with no ambiguity in the resulting imagery. These techniques are demonstrated on modeling and experimental data.

4.1 Point Target Simulations

For undersampled periodic apertures, grating lobes result in the cross-range and vertical dimensions. It is assumed that the frequency step size is small enough that grating lobes are not generated in the range dimension within the desired image depth. Grating lobe spacings in the cross-range and vertical dimensions are given by $D_y^u = \frac{r_\text{ø}\lambda_c}{2\Delta y}$ and $D_z^u = \frac{r_\text{ø}\lambda_c}{2\Delta z}$, respectively. In each case, the spacing is proportional to the signal wavelength at the center of the frequency band. The RSM technique applies iterative minimizations, so any artifacts that change location from one iteration to another are removed. By applying the RSM over aperture while randomizing center frequency (RSM-AFC), the grating lobes are shifted and removed.

The RSM technique has been applied in the frequency domain before [19]; however, it has not been applied in a manner that sufficiently randomizes center frequency for grating lobe removal. The RSM technique has, also, never been applied for the purpose of removing grating lobes. Typically, the RSM technique with random frequency selection (RSM-F) is applied by setting random frequency samples to 0 throughout the band at each iteration. It is assumed here that the randomly selected frequency samples are selected according to a uniform distribution. This does not sufficiently randomize the center frequency of the band formed by the remaining frequency samples.

The following process is used in this dissertation to select frequency bands at each iteration of the RSM while randomizing the center frequency. First, a random center frequency $f_{c,i}$ is selected from the operating bandwidth according to the uniform distribution, where i is the RSM iteration index. This guarantees that center frequency is randomized. The list of available center frequencies is

$$\left\{f_c - \frac{B}{2}, f_c - \frac{B}{2} + \Delta f, ..., f_c + \frac{B}{2}\right\},$$

where $\Delta f = 15$ MHz. Then a bandwidth B_i is randomly selected at iteration i from the list of available bandwidths:

$$\left\{0, \Delta f, ..., 2\min\left(f_{c,i} - \left(f_c - \frac{B}{2}\right), \left(f_c + \frac{B}{2}\right) - f_{c,i}\right)\right\}.$$

The minimum bandwidth (0 MHz) occurs when $f_{c,i} = f_c - \frac{B}{2}$ or $f_{c,i} = f_c + \frac{B}{2}$. When $f_{c,i} = f_c$, the list of available bandwidths is determined; $B_i \in \{0, \Delta f, ..., B\}$. The resulting distribution of center frequencies is shown in Fig. 4.1. In this case, the center frequency is uniformly distributed. This is enforced by the selection process.

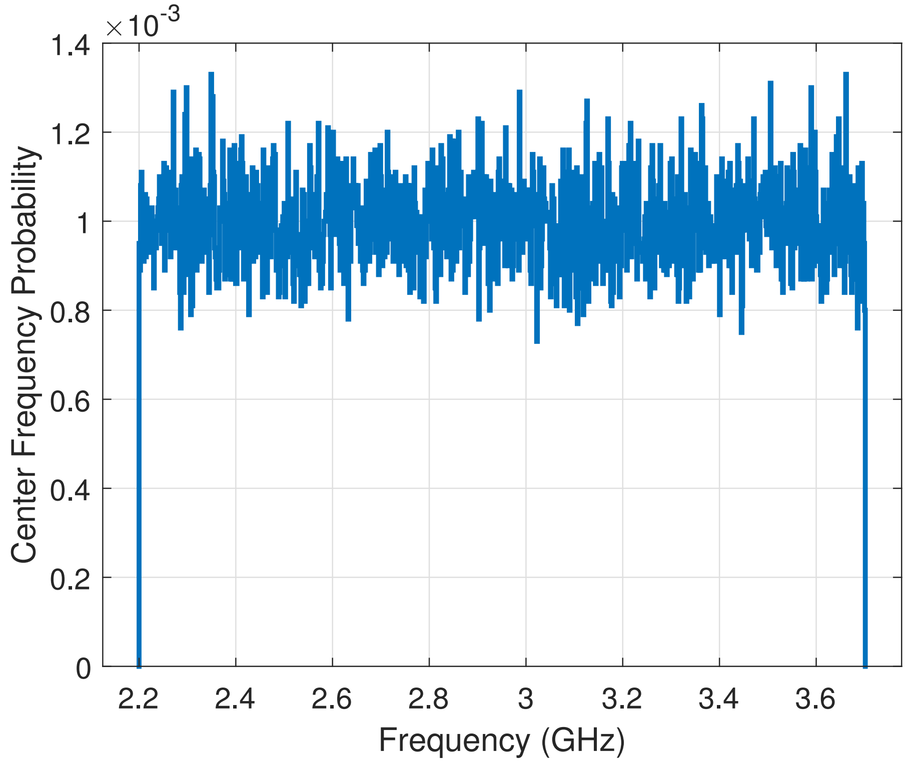

Figure 4.1. Center frequency distribution using the new method of frequency selection.

For this new RSM process to completely remove the grating lobes, their locations must be shifted enough that their nulls reach their original peak. Although the image is formed in the near field, the apertures considered here are relatively narrow, so it is assumed that the resolution of the grating lobe is approximately equal to the resolution of the target. The peak of the grating lobe is at $\frac{r_{\o}\lambda_c}{2\Delta y}$, while the nulls around the grating lobe occur at $\frac{r_{\o}\lambda_c}{2\Delta y} - \frac{r_{\o}\lambda_c}{2A_y}$ and $\frac{r_{\o}\lambda_c}{2\Delta y} + \frac{r_{\o}\lambda_c}{2A_y}$. The grating lobes are shifted by using subbands with different center frequencies within the operating bandwidth. The maximum and minimum frequencies of the bandwidth generate grating lobes with the most displacement from the original grating lobe. To shift the grating lobe towards the target, the maximum frequency is used. To shift the grating lobe away from the target, the minimum frequency is used. To shift the grating lobes beyond the point where their null coincides with the peak of the original grating lobe, we must have

$$\frac{r_{\o}c}{2f_{\max}\Delta y} < \frac{r_{\o}c}{2f_c\Delta y} - \frac{r_{\o}c}{2f_cA_y} \tag{4.1}$$

and

$$\frac{r_{\o}c}{2f_{\min}\Delta y} > \frac{r_{\o}c}{2f_c\Delta y} - \frac{r_{\o}c}{2f_c A_y}. \tag{4.2}$$

Simplifying this expression yields

$$\frac{f_c}{f_{\max}} < 1 - \frac{\Delta y}{A_y} \tag{4.3}$$

and

$$\frac{f_c}{f_{\min}} > 1 + \frac{\Delta y}{A_y}. \tag{4.4}$$

In the z direction, we have

$$\frac{f_c}{f_{\max}} < 1 - \frac{\Delta z}{A_z}, \tag{4.5}$$

$$\frac{f_c}{f_{min}} > 1 + \frac{\Delta z}{A_z}. \tag{4.6}$$

This property is explored in the following simulation. This problem is approached from an aperture design perspective, with the frequency band fixed from 2.2 to 3.7 GHz with a 15–MHz step size. First, a 1-m-by-1-m aperture is considered at the range $x = 4$ m. Since the aperture length and the band are fixed, we can solve Eqs. (4.3 – 4.6) for Δy and Δz. In the y-direction, $\Delta y < 0.203$ and $\Delta y < 0.341$. Each of the inequalities correspond to moving the grating lobes in a specific direction. If either of the two inequalities is satisfied, then a null will be placed on the original peak and it will be removed. As a result, the grating lobes are canceled for the maximum condition when $\Delta y < 0.341$. The problem is identical in y and z, so the same step size requirement is used in the z direction. A second aperture, with $A_y = 0.8$ m, $A_z = 0.8$ m, and $x_a = 4$ m is considered. The sampling conditions for this frequency band and these aperture extents are $\Delta y < 0.2727$ m and $\Delta z < 0.2727$ m. Here, Δy and Δz are set to 0.4 m so that the condition is not satisfied. Fig. 4.2 shows these two apertures and a simulated point target.

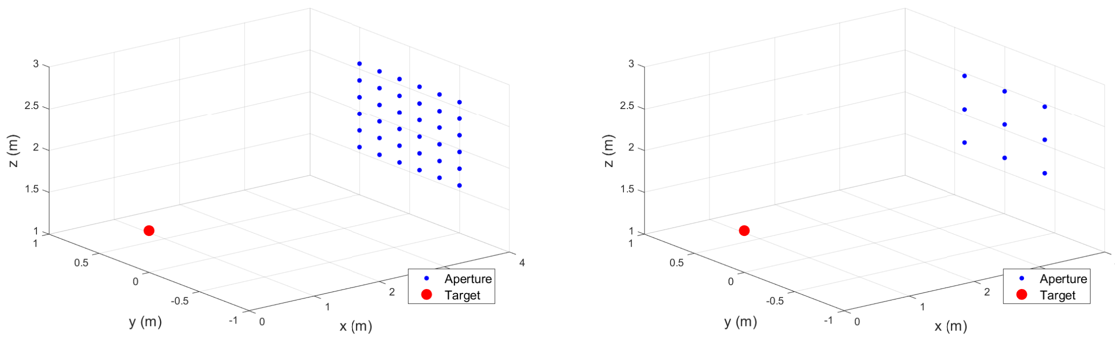

(a) (b)

Figure 4.2. (a) An aperture that satisfies that sampling requirement for removing grating lobes, and (b) an aperture that does not satisfy the sampling requirement for removing grating lobes.

The resulting imagery, obtained by applying this modified version of RSM, is shown in Fig. 4.3, displaying the strongest 40 dB. As expected, the image with tighter spacing had no visible artifacts. The image that did not satisfy the requirement for removing grating lobes did have extremely low grating lobes despite not satisfying this requirement. Even though the null from the grating lobe did not pass completely over the original grating lobe peak, it is shifted enough that a new minimum is taken at a greatly reduced level from the original grating lobe strength. The grating lobe pattern is still visible about 20 dB lower than the original pattern. This demonstrates that this technique is effective even when the aperture sampling condition is not satisfied. The resulting peak corresponds to the point on the grating lobe that can be shifted to line up with the original grating lobe peak. In this case it is not a null, but it is 16.6208 dB below the original peak.

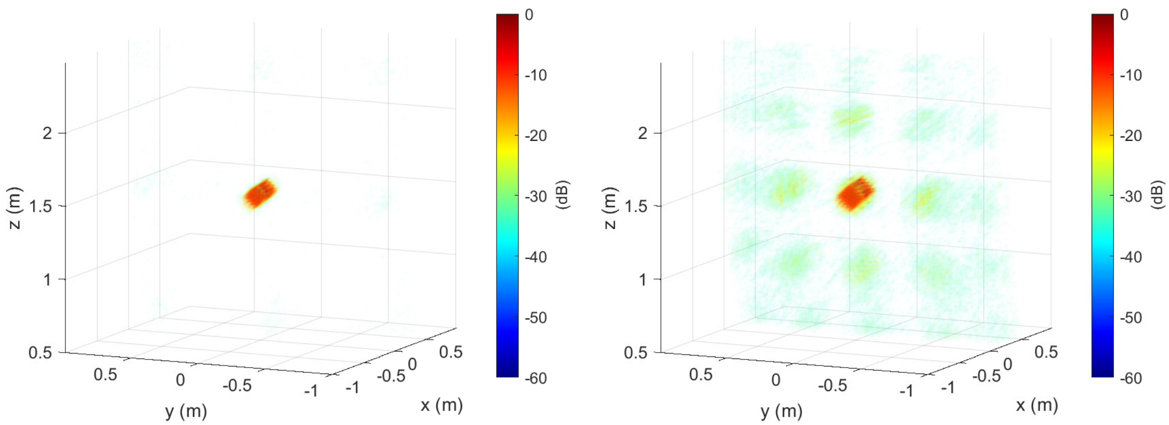

(a) (b)

Figure 4.3. Images formed with the aperture that (a) satisfies the sampling requirement to remove grating lobes and (b) does not satisfy the sampling requirement.

The peak artifacts in these two simulations are plotted with respect to RSM iteration in Fig. 4.4. The PA for the sufficiently sampled aperture is 24.9 dB, whereas the insufficiently sampled aperture is 16.6 dB. Both peak artifacts are well below the target. This shows that, even for an extremely sparse aperture, this technique can greatly reduce grating lobes in an image. It is important to note that this technique benefits greatly from a wide bandwidth, which allows for larger movement of the grating lobe location. It is desirable for the artifacts to be greater than 20 dB below the target though, so it is still recommended that the conditions in Eqs. 4.3 – 4.6 are satisfied.

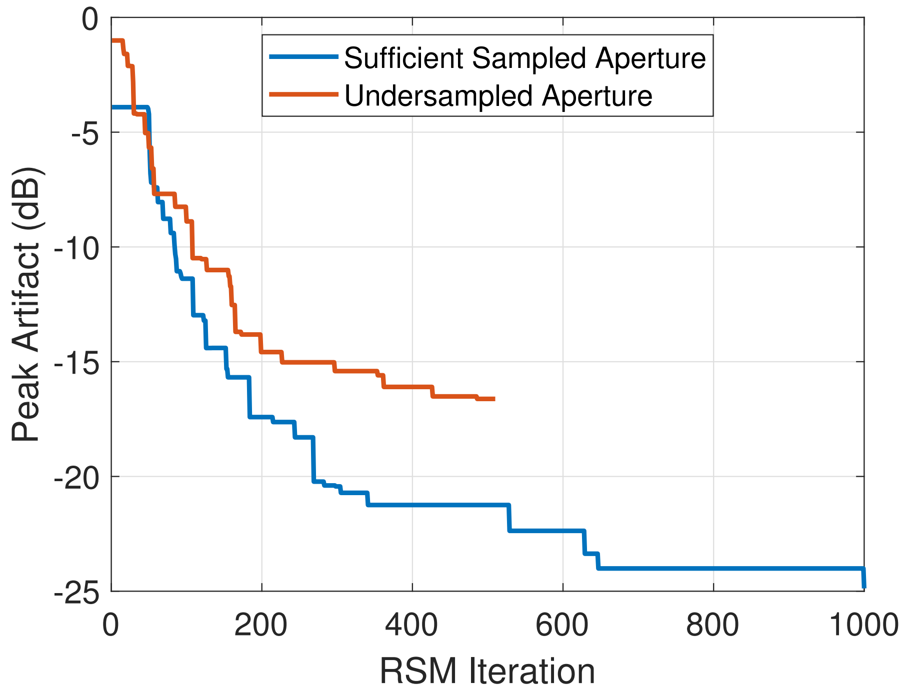

Figure 4.4. PA comparison between an aperture that satisfies the grating lobe condition and an aperture that does not satisfy the grating lobe condition.

In this section, a modification to the RSM technique was presented that removes grating lobes. By randomizing center frequency in each iteration of the RSM, grating lobe spacing is randomized and grating lobes can be removed. This technique was demonstrated using a simulation of a point target. A relationship between aperture parameters and frequency parameters was also derived that guarantees grating lobe suppression. This concept was also demonstrated using simulations of a point target.

4.2 Modeling

In Section 4.1, a new technique was demonstrated that removes grating lobes in an image formed from an undersampled, periodic aperture. In this section, this technique is validated for extended targets. As in Section 3.3, a cylinder is simulated using horizontally polarized dipoles. This model is simulated with the periodic aperture shown in Fig. 4.5.

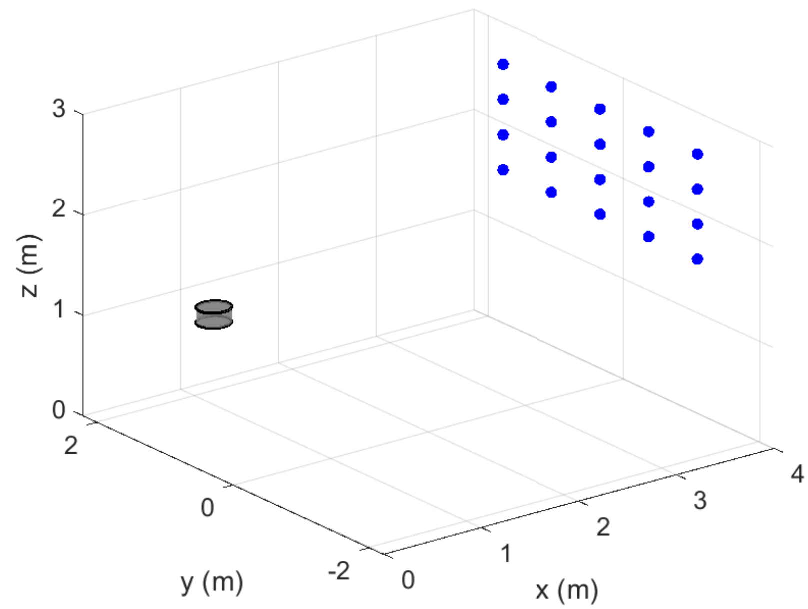

Figure 4.5. Periodic aperture.

Fig. 4.6 shows imagery formed using this aperture. Fig. 4.6a shows imagery formed using traditional RSM, while Fig. 4.6b shows imagery formed using RSM with frequency center randomization. For the RSM technique, the grating lobes are not removed. However, as in the simulations, randomizing center frequency throughout the RSM algorithm reduces grating lobes.

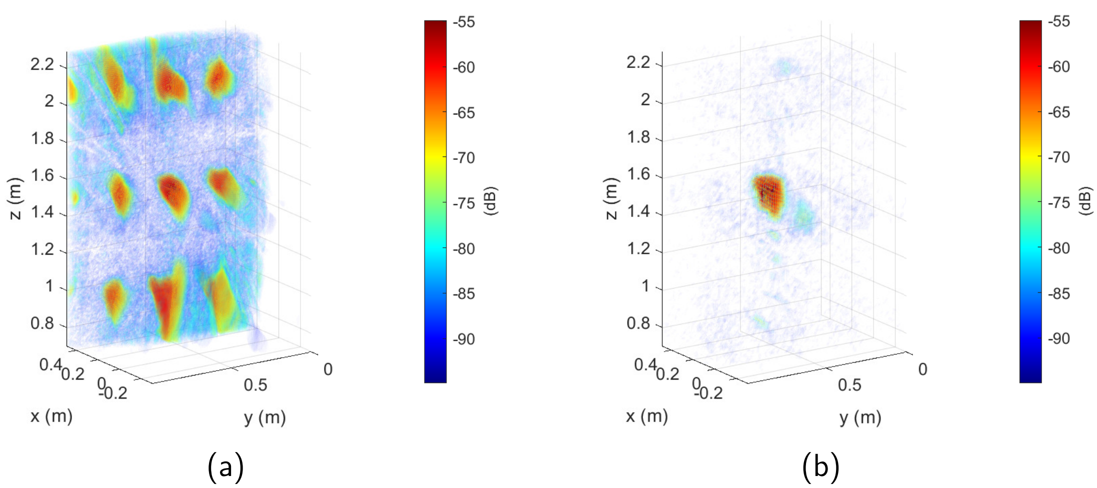

Figure 4.6. Image formed using (a) the RSM technique and (b) the RSM-AFC technique.

The PA for both cases is plotted in Fig. 4.7. The PA is 3.5 dB using the RSM algorithm and 25.4 dB using the RSM-AFC algorithm. When applying the conventional RSM technique, the grating lobe level remains elevated to almost the same strength as the target. The RSM-AFC technique lowers the grating lobes to the point that they do not generate false alarms.

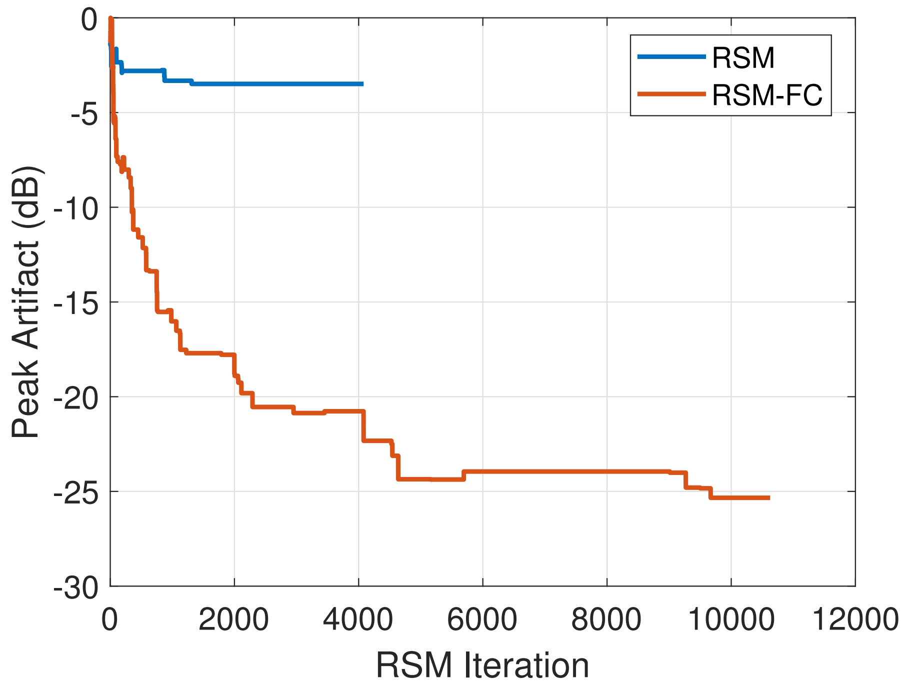

Figure 4.7. PA for images formed using the RSM technique and the RSM-AFC technique.

4.3 Experimentation

The RSM-AFC algorithm is tested here using experimental data. Model data does not consider practical effects such as system noise, filter roll-off, and interference. In order for the algorithm to work in this environment, it needs to be changed so that it is more robust to these challenges. An experiment is considered using a single trihedral placed on a styrofoam block, shown in Fig. 4.8. The antenna elements and scanning platform are also shown. The data are measured in a quasi-monostatic with the antennas separated in y by 0.45 m.

(a) (b)

Figure 4.8. (a) Trihedral on a styrofoam block. (b) Scanning platform with antennas mounted.

Measurements were made along a grid varying in the y and z directions. This grid is shown in Fig. 4.9. The plotted points come from the bistatic phase center, which is the geometric center of each transmit and receive antenna pair. Apertures from the simulation and modeling sections are found by downsampling this grid.

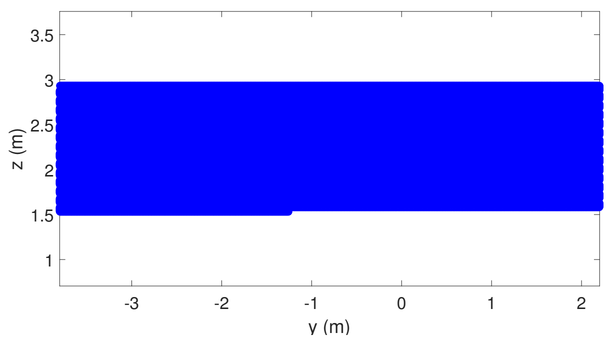

Figure 4.9. Bistatic phase centers from experimental data.

First, the spectrum of the scattered radar signal is analyzed. Fig. 4.10 shows the spectrum when the aperture is at $(x, y, z) = (4.33, -0.16, 1.882)$ m. At this position, the aperture is at the same cross-range position as the target. It is not guaranteed that a target response will have a strong SCR at a given frequency. When the RSM-AFC technique was used in the modeling and simulation sections, frequency randomization included the possibility of using a single frequency. However, the use of a single frequency makes this technique more susceptible to problems like noise, interference, and low-RCS responses.

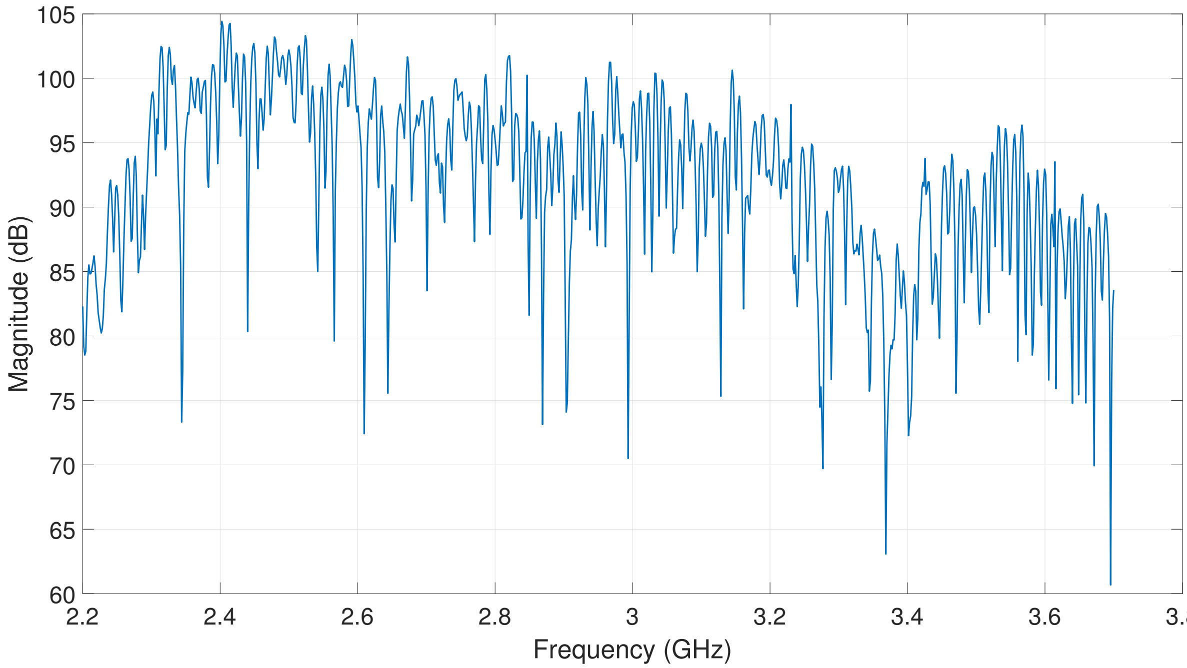

Figure 4.10. Received spectrum at a single aperture position.

An experiment is carried out to demonstrate the impact of practical effects on this algorithm. First, the aperture in Fig. 4.2a is used. As demonstrated in Sections 4.1 and 4.2, this aperture is narrow enough to avoid resolving multiple scattering centers and meets the requirements for completely reducing grating lobes. In the simulation and modeling sections the apertures are monostatic. For the experimental measurements, the antennas are quasi-monostatic. The antenna elements for this experiment are selected by mapping the simulated/modeled aperture to the closest phase center and using the corresponding elements. The resulting antenna phase centers are shown in Fig. 4.11. This aperture is 1 m by 1 m and fixed at $x = 4.3$ m. The aperture spacing is 0.2 m in both the y and z directions.

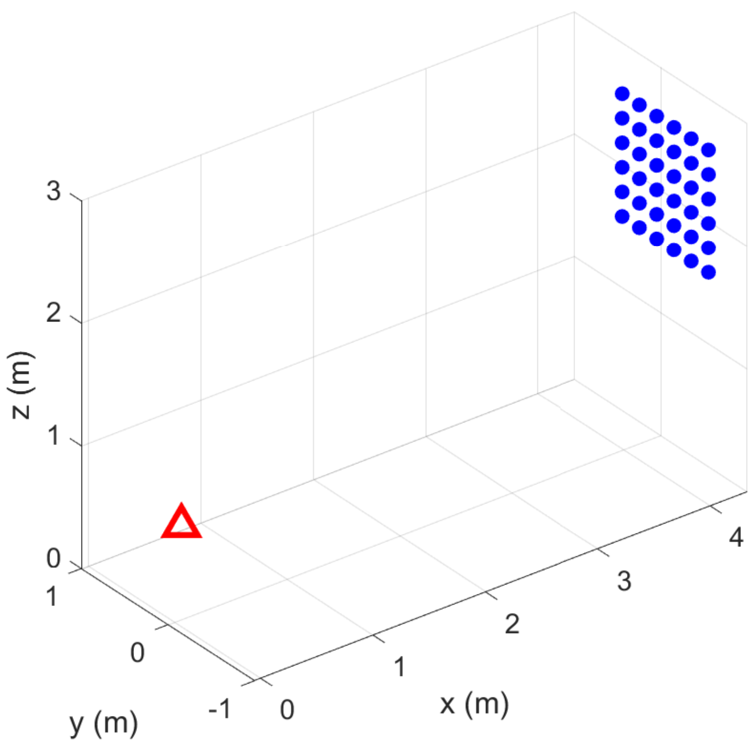

Figure 4.11. Periodic aperture and trihedral.

Fig. 4.12 shows an image formed using the aperture above and the RSM-AFC technique. The artifacts trace the locations where grating lobes and sidelobes originated. The maximum sidelobe of the image is 10.9 dB below the peak. This is not an acceptable sidelobe level in an image. Furthermore, the peak itself has been reduced to -14.4 dB.

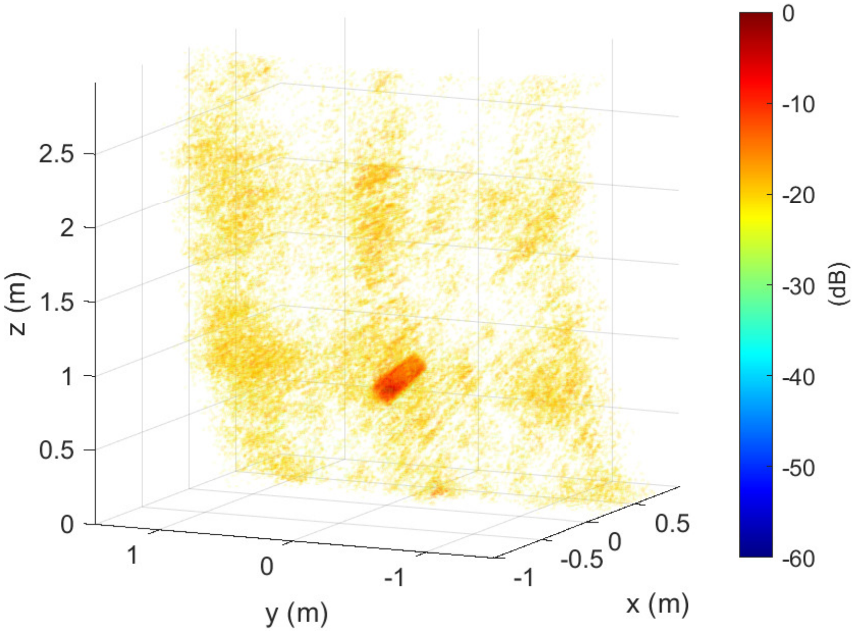

Figure 4.12. Image of trihedral after RSM-AFC algorithm.

To make the algorithm more robust, a minimum bandwidth for the subbands in each iteration is employed. Using a frequency band improves processing gain and averages the target response over that band. In the following simulation, a minimum bandwidth of 200 MHz is used. Fig. 4.13 shows the resulting image. With the introduction of required bandwidth, the span of allowable center frequencies is reduced. The span of center frequencies in this simulation is 1.3 GHz, ranging from 2.3 to 3.6 GHz. With this new set of frequencies the sampling requirement is given by $\Delta y = \Delta z < 0.2826$. The aperture considered here satisfies the sampling requirements. This is confirmed in the Fig. 4.13.

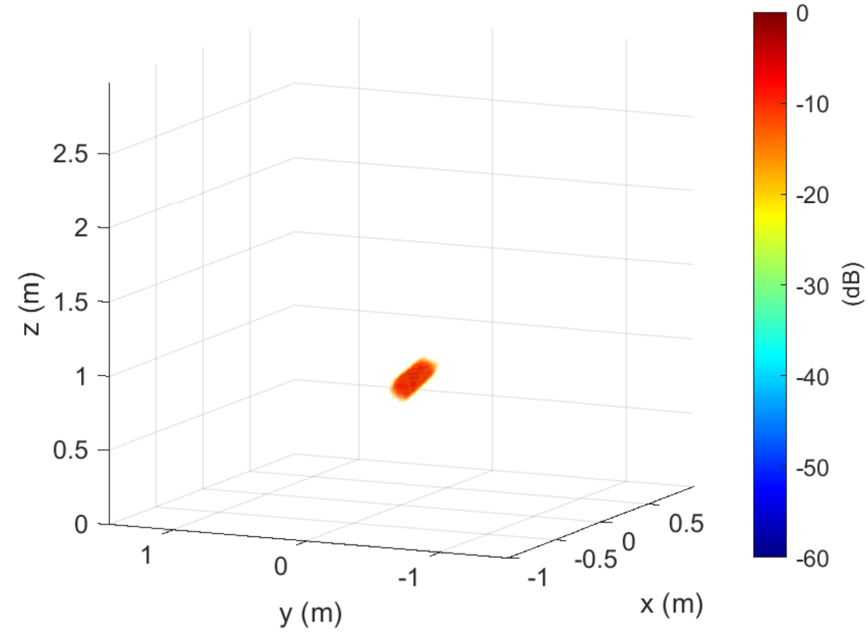

Figure 4.13. Image of a trihedral after RSM-AFC algorithm with a minimum bandwidth at each iteration.

Next, an aperture that does not meet the sampling requirements (the aperture in Fig. 4.2b), is obtained by downsampling the experimental aperture. The bistatic phase centers are plotted in Fig. 4.14. The aperture is 0.8 by 0.8 m, with each sample fixed at $x = 4.33$ m. The sample spacing is $\Delta y = \Delta z = 0.4$ m.

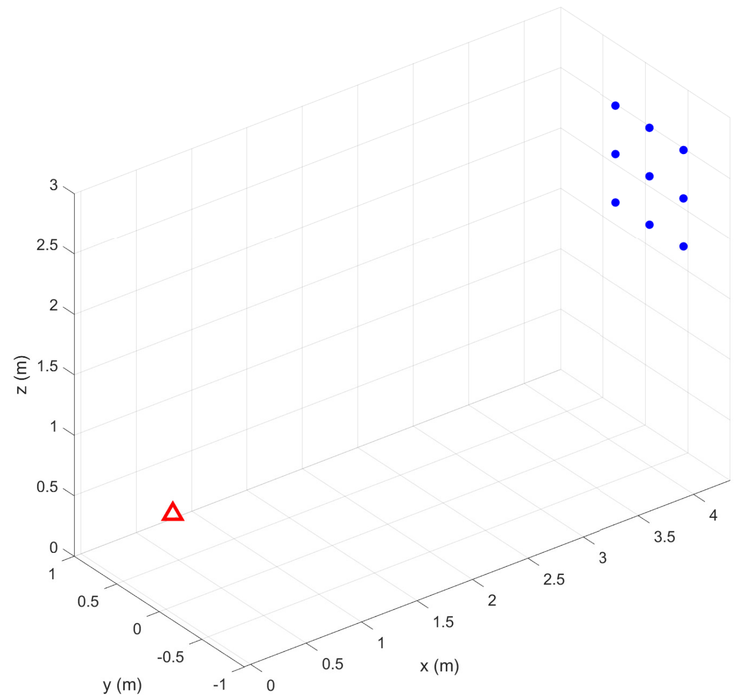

Figure 4.14. Undersampled aperture that does not satisfy the sampling conditions for grating lobe removal.

The sampling requirement for complete grating lobe removal is not met in this case. The resulting image is shown in Fig 4.15. After applying the RSM-AFC with a minimum bandwidth constraint, the grating lobes are still present. This experimentally confirms that the conditions in Eqs. 4.3 – (4.6) are required for complete grating lobe removal.

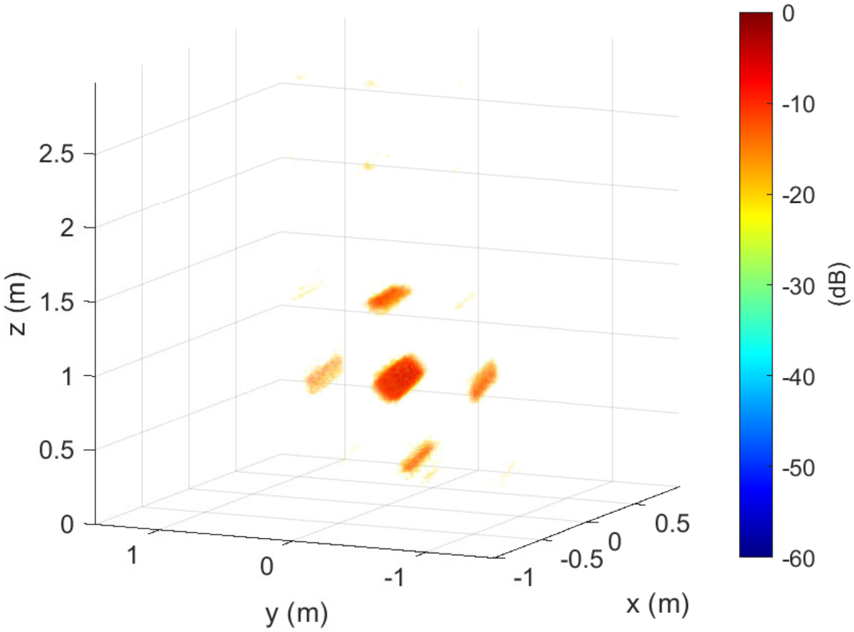

Figure 4.15. Image of a trihedral after RSM-AFC algorithm for an aperture that does not meet the sampling conditions to remove grating lobes.

Chapter 5
Conclusion and Future Work

5.1 Summary

This dissertation presented new techniques for SAR imaging applications that use sparsely sampled synthetic apertures. The emphasis in designing the data collection geometries and the signal processing algorithms is on suppressing the sidelobes and grating lobes in 3-D radar imagery, with a reduced number of aperture samples.

In Chapter 2, analytical PSFs have been derived for linear and grid aperture geometries. Many of the assumptions used in the closed-form PSF derivation are not valid in near-field side-looking imaging scenarios, but simulated data show that the analytical PSF closely estimates the mainlobe response. The analytical PSFs also accurately estimate grating lobe spacings for undersampled apertures. They accurately estimate grating lobe width in cases of extreme undersampling, where the grating lobe is close to the mainlobe response. Experimental data were collected for two vertically displaced metal cylinders using a linear aperture and a planar aperture. The benefits of 3-D resolution are shown by comparing SCR for the two images.

Subsequently, images created with various sparse apertures were investigated in Chapters 3 and 4. The RSM algorithm was applied to reduce sidelobes, and it was shown that random apertures only generate sidelobes. This allows for sparse random apertures to be used with the RSM algorithm to generate 3-D imagery with minimal artifacts. A periodic undersampled aperture was shown to generate grating lobes, which cannot be reduced using the RSM algorithm. An organized method of subaperture selection was also introduced, which improved the convergence time of the RSM algorithm when compared with random subaperture selection. This technique was then applied to modeled data of a cylinder. The combination of a random aperture and the RSM technique successfully imaged the cylinder, but it was shown that the target response can be affected by magnitude variation and aspect-dependent responses from different scattering centers when a wide aperture is used. Aperture extent was limited for the rest of the dissertation as a result. The combination of a random aperture with the RSM algorithm was also applied to measured radar data of a corner reflector successfully.

Finally, the RSM-ACF algorithm was introduced to remove grating lobes from images generated using undersampled, periodic apertures. By employing frequency subbands with randomized center frequencies at each iteration of the RSM algorithm, the grating lobe spacings are moved around, which allows them to be reduced. A necessary condition for grating lobe removal was also derived for the SAR system parameters. The RSM-ACF technique was applied to modeled radar data for a cylinder target and was shown to be effective. The same technique was subsequently applied to experimental radar data obtained from a corner reflector. Sub-bands of at least 200 MHz were used during the center frequency randomization to make the algorithm more robust to interference and variations in the target frequency response.

The techniques introduced in this study should have important applications to 3-D imaging of difficult targets concealed in heavily cluttered environments, including buried objects. They should be particularly suited to practical SAR implementations on UAV platforms with high mobility, that allow flexible data collection geometries, but present stringent SWAP requirements. These techniques were demonstrated at S-band frequencies, which were selected as a trade-off between good penetration through media and good cross-range and vertical resolution. For a fixed resolution, the aperture can be scaled to apply this technique in a different frequency band for different applications. It can also be applied to different radar processing techniques in addition to SAR. In Reference [44], the technique using the RSM algorithm with a random aperture distribution is applied to the problem of long-range surveillance in tracking radars.

5.2 Future Work

This dissertation applied fundamental imaging concepts to create new approaches to sparse aperture imaging. Simulated examples were implemented on a point target and a modeled cylinder before applying these techniques to measured data of a corner reflector. This research opens the door to a long list of potential new techniques, scenarios, and applications.

5.2.1 Aperture Design

Extension of this work would study the effect of individual aperture samples on the success of this algorithm. This is rooted in the use of the random aperture. Simulations should be performed to determine a minimum sample density to avoid the generation of grating lobes. This would involve the study of individual aperture positions and null placement for different subapertures. These principles could be extended to on-the-fly aperture design for minimizing the number of samples and RSM iterations necessary to generate a radar image with no grating lobes.

5.2.2 Modeling

So far, this algorithm was only applied to metal cylinders in HH polarization. This work should be extended to a variety of targets and polarizations to determine its behavior for targets with different scattering centers. Modeling should also be performed with multiple targets in the same scene to investigate how phenomena like multipath are processed through the RSM and RSM-ACF. Finally, the impact of distributed clutter on both the target response and the algorithm performance must be tested.

5.2.3 Experimental Data

This algorithm must be tested in more challenging scenarios with more challenging targets. Distributed clutter, like foliage, should also be introduced. The algorithm would need to adapted to low SCR scenarios where the target signal is not obvious or even present at some aperture positions.

5.2.4 UAV Platform

The use of random apertures lends itself to SAR system implementation on a UAV platform. The apertures in this dissertation were considered as flight paths of a single quasimonostatic sensor. In the computer models, the apertures were typically randomly distributed, which would prove difficult to construct in practice. An aperture synthesis procedure should be developed which treats the aperture more as a spatial path to be flown rather then a random set of points. Also, these realistic flight trajectories should be tested on an sUAV platform for proof of concept.

As an alternative to constructing these apertures using the flight path of a single, quasimonostatic sensor, these apertures could be constructed using a distributed set of quasimonostatic sensors operating in a coordinated manner. Two methods of sparse imaging were presented in this dissertation. In the first method, random aperture samples are paired with the RSM algorithm to generate low-artifact imagery. The considered apertures represented flight paths constructed using a single quasi-monostatic platform. It should be noted that these apertures could also be realized using multiple radar platforms operating in a distributed manner. The use of multiple platforms would greatly simplify the flight paths that each individual platform would need to fly. If coherence is established across the platforms, then they can theoretically operate in a multistatic mode. In multistatic radar, each platform transmits an orthogonal waveform, and each waveform is received on all platforms. With N platforms operating coherently, there are a maximum of $N(N+1)/2$ independent channels as opposed to N independent channels when the different platforms are not coherent. A coherent set of apertures can synthesize an aperture much more quickly, and the resulting aperture is significantly less sparse.

The second technique applies a modified version of the RSM algorithm to uniformly sampled apertures. In practice, these uniformly sampled apertures would be realized using a vertical antenna array rather than as the flight path of a quasi-monostatic platform. An antenna array could be replaced by a set of quasi-monostatic platforms flown in an organized vertical pattern. This would be used to reduce the SWAP burden on an individual radar platform. If SWAP is not an issue, then a set of platforms could be stacked vertically in which each platform has a vertical array. This would increase both the number of aperture samples and the aperture length, which would improve the resolution in the resulting imagery.

5.2.5 Distributed Radar

A potential application for the techniques presented in this dissertation is distributed radar. In distributed radar, a network of transmitters and receivers are geographically separated, providing a wide set of observation angles for a region of interest [45]. This leads to a naturally sparse aperture for imaging. Most targets of interest are anisotropic scatterers, and the wide set of observation angles leads to a large variety of responses from the target. This renders coherent processing extremely difficult, requiring complicated rephasing of the received signals to maximize coherence at a known target location. This technique assumes a point-like target, as well as a priori information on the target location, so it is extremely difficult to implement in practice. However, it does provide an upper bound to performance. A more reasonable implementation uses incoherent processing to combine information from each of the distributed sensors. Future work should test the algorithms presented in this dissertation for noncoherent processing.

Appendix A
Derivation of the Range Approximation

For the monostatic geometry in Fig. 2.1, the range from aperture sample m to the point target at $\vec{\boldsymbol{r}}_{\boldsymbol{o}}$ is approximated by the length of the difference between their position vectors:

$$
\begin{aligned}
|\vec{\boldsymbol{r}}_{\boldsymbol{o}} - \vec{\boldsymbol{r}}_{\boldsymbol{m}}| &= \sqrt{(x_o - x_a)^2 + (y_m - y_o)^2 + (z_m - z_a - z_o + z_a)^2} \\
&= \sqrt{(x_o - x_a)^2 + y_m^2 + y_o^2 - 2y_o y_m + (z_o - z_a)^2 + z_m^2 - z_a^2 - 2z_m z_o + 2z_o z_a} \\
&= \left(1 + \frac{y_m^2 + (z_m^2 - z_a^2) + 2z_o z_a}{r_o^2} - \frac{2\,(y_o y_m + z_o z_m)}{r_o^2}\right)^{1/2}.
\end{aligned}
\tag{A.1}
$$

For further simplification, it is assumed that the aperture is small in the horizontal and vertical directions with respect to the range from the target to the aperture center, with $|y_m| << r_o$ and $z_m^2 - z_a^2 << r_o^2$. Furthermore, it is assumed that the point target is close to the origin, with $2z_o z_a << r_o^2$. Applying these assumptions the range is approximated as

$$
|\vec{\boldsymbol{r}}_{\boldsymbol{o}} - \vec{\boldsymbol{r}}_{\boldsymbol{m}}| \approx r_o \left(1 - \frac{2\,(y_o y_m + z_o z_m)}{r_o^2}\right)^{1/2}. \tag{A.2}
$$

The function $f(x)$ can be evaluated at a by the Taylor series:

$$
f(x) = \sum_{n=0}^{\infty} \frac{f^{(n)}(a)}{n!}\,(x - a)^n\,, \tag{A.3}
$$

where $f^{(n)}(a)$ denotes the nth order derivative of f evaluated at a. A function can be estimated by truncating this series. In this case, the function $f(x) = (1+x)^{\frac{1}{2}}$ is estimated at $a \approx 0$, using a second order Taylor series approximation:

$$(1+x)^{\frac{1}{2}} \approx 1 - \frac{y_o y_m + z_o z_m}{r_o^2}. \tag{A.4}$$

This is inserted in Eq. (A.2), resulting in the range approximation:

$$|\vec{\boldsymbol{r}}_{\boldsymbol{o}} - \vec{\boldsymbol{r}}_{\boldsymbol{m}}| \approx r_o - \frac{y_o y_m + z_o z_m}{r_o} \tag{A.5}$$

Bibliography

[1] UN. Secretary General (2023) *Assistance in mine action: report of the Secretary-General*, *Tech. Rep. A/78/259*, Inter-Agency Coordination Group on Mine Action.

[2] Bradley, M. R., T. R. Witten, R. McCummins, M. Crowe, S. Stewart, and M. Duncan (1999) "Mine detection with a multichannel stepped-frequency ground-penetrating radar," in *Detection and Remediation Technologies for Mines and Minelike Targets IV* (A. C. Dubey, J. F. Harvey, J. T. Broach, and R. E. Dugan, eds.), vol. 3710, International Society for Optics and Photonics, SPIE, pp. 953 – 960. URL `https://doi.org/10.1117/12.357115`

[3] Bradley, M. R., T. R. Witten, R. McCummins, and M. Duncan (2002) "Mine detection with ground penetrating synthetic aperture radar," in *Detection and Remediation Technologies for Mines and Minelike Targets VII* (J. T. Broach, R. S. Harmon, and G. J. Dobeck, eds.), vol. 4742, International Society for Optics and Photonics, SPIE, pp. 248 – 258. URL `https://doi.org/10.1117/12.479095`

[4] Chambers, D. H., D. W. Paglieroni, J. E. Mast, and N. R. Beer (2013) *Real-Time Vehicle-Mounted Multistatic Ground Penetrating Radar Imaging System for Buried Object Detection*, *Tech. Rep. LLNL-TR-615452*, Army Research Laboratory, Livermore, CA, USA.

[5] Paglieroni, D. W., D. H. Chambers, J. E. Mast, S. W. Bond, and N. Reginald Beer (2015) "Imaging Modes for Ground Penetrating Radar and Their Relation to Detection Performance," *IEEE Journal of Selected Topics in Applied Earth Observations and Remote Sensing*, **8**(3), pp. 1132–1144.

[6] Kositsky, J. and P. Milanfar (1999) "Forward-looking high-resolution GPR system," in *Detection and Remediation Technologies for Mines and Minelike Targets IV* (A. C. Dubey, J. F. Harvey, J. T. Broach, and R. E. Dugan, eds.), vol. 3710, International Society for Optics and Photonics, SPIE, pp. 1052 – 1062. URL `https://doi.org/10.1117/12.356986`

[7] Kositsky, J. (2000) "Results from a forward-looking GPR mine detection system," in *Detection and Remediation Technologies for Mines and Minelike Targets V* (A. C.

Dubey, J. F. Harvey, J. T. Broach, and R. E. Dugan, eds.), vol. 4038, International Society for Optics and Photonics, SPIE, pp. 1077 – 1087.
URL `https://doi.org/10.1117/12.396193`

[8] Kositsky, J., R. Cosgrove, C. A. Amazeen, and P. Milanfar (2002) "Results from a forward-looking GPR mine detection system," in *Detection and Remediation Technologies for Mines and Minelike Targets VII* (J. T. Broach, R. S. Harmon, and G. J. Dobeck, eds.), vol. 4742, International Society for Optics and Photonics, SPIE, pp. 206 – 217.
URL `https://doi.org/10.1117/12.479091`

[9] Bradley, M. R., T. R. Witten, M. Duncan, and R. McCummins (2003) "Mine detection with a forward-looking ground-penetrating synthetic aperture radar," in *Detection and Remediation Technologies for Mines and Minelike Targets VIII* (R. S. Harmon, J. H. H. Jr., and J. T. Broach, eds.), vol. 5089, International Society for Optics and Photonics, SPIE, pp. 334 – 347.
URL `https://doi.org/10.1117/12.487054`

[10] Liu, G., Y. Wang, J. Li, and M. R. Bradley (2003) "SAR imaging for a forward-looking GPR system," in *Detection and Remediation Technologies for Mines and Minelike Targets VIII* (R. S. Harmon, J. H. H. Jr., and J. T. Broach, eds.), vol. 5089, International Society for Optics and Photonics, SPIE, pp. 322 – 333.
URL `https://doi.org/10.1117/12.485687`

[11] Bradley, M. R., T. R. Witten, M. Duncan, and R. McCummins (2004) "Anti-tank and side-attack mine detection with a forward-looking GPR," in *Detection and Remediation Technologies for Mines and Minelike Targets IX* (R. S. Harmon, J. T. Broach, and J. H. H. Jr., eds.), vol. 5415, International Society for Optics and Photonics, SPIE, pp. 421 – 432.
URL `https://doi.org/10.1117/12.543939`

[12] Ressler, M., L. Nguyen, F. Koenig, D. Wong, and G. Smith (2007) "The Army Research Laboratory (ARL) synchronous impulse reconstruction (SIRE) forward-looking radar," in *Unmanned Systems Technology IX* (G. R. Gerhart, D. W. Gage, and C. M. Shoemaker, eds.), vol. 6561, International Society for Optics and Photonics, SPIE, p. 656105.
URL `https://doi.org/10.1117/12.719688`

[13] Phelan, B. R., K. I. Ranney, K. A. Gallagher, J. T. Clark, K. D. Sherbondy, and R. M. Narayanan (2017) "Design of Ultrawideband Stepped-Frequency Radar for Imaging of Obscured Targets," *IEEE Sensors Journal*, **17**(14), pp. 4435–4446.

[14] Fransson, J., F. WaLter, and L. Ulander (2000) "Estimation of forest parameters using CARABAS-II VHF SAR data," *IEEE Transactions on Geoscience and Remote Sensing*, **38**(2), pp. 720–727.

[15] Reigber, A. and A. Moreira (2000) "First demonstration of airborne SAR tomography using multibaseline L-band data," *IEEE Transactions on Geoscience and Remote Sensing*, **38**(5), pp. 2142–2152.

[16] Hajnsek, I., F. Kugler, S.-K. Lee, and K. P. Papathanassiou (2009) "Tropical-Forest-Parameter Estimation by Means of Pol-InSAR: The INDREX-II Campaign," *IEEE Transactions on Geoscience and Remote Sensing*, **47**(2), pp. 481–493.

[17] Neumann, M., S. S. Saatchi, L. M. H. Ulander, and J. E. S. Fransson (2012) "Assessing Performance of L- and P-Band Polarimetric Interferometric SAR Data in Estimating Boreal Forest Above-Ground Biomass," *IEEE Transactions on Geoscience and Remote Sensing*, **50**(3), pp. 714–726.

[18] Binder, B., M. Toups, S. Ayasli, and E. Adams (1995) "SAR foliage penetration phenomenology of tropical rain forest and northern US forest," in *Proceedings International Radar Conference*, pp. 158–163.

[19] Phelan, B. (2016) *Theory, Design, Analysis, and Implementation of a Spectrally Agile Frequency-Incrementing Reconfigurable (SAFIRE) Forward Looking Ground Penetrating Radar*, Ph.D. dissertation, The Pennsylvania State University.

[20] Fasano, G., A. Renga, A. R. Vetrella, G. Ludeno, I. Catapano, and F. Soldovieri (2017) "Proof of concept of micro-UAV-based radar imaging," in *2017 International Conference on Unmanned Aircraft Systems (ICUAS)*, pp. 1316–1323.

[21] García-Fernández, M., Y. Álvarez López, A. Arboleya Arboleya, B. González Valdés, Y. Rodríguez Vaqueiro, F. Las-Heras Andrés, and A. Pino García (2018) "Synthetic Aperture Radar Imaging System for Landmine Detection Using a Ground Penetrating Radar on Board a Unmanned Aerial Vehicle," *IEEE Access*, **6**, pp. 45100–45112.

[22] García-Fernández, M., Y. Á. López, and F. L.-H. Andrés (2020) "Airborne Multi-Channel Ground Penetrating Radar for Improvised Explosive Devices and Landmine Detection," *IEEE Access*, **8**, pp. 165927–165943.

[23] Schartel, M., R. Burr, W. Mayer, N. Docci, and C. Waldschmidt (2018) "UAV-Based Ground Penetrating Synthetic Aperture Radar," in *2018 IEEE MTT-S International Conference on Microwaves for Intelligent Mobility (ICMIM)*, pp. 1–4.

[24] Dill, S., E. Schreiber, M. Engel, A. Heinzel, and M. Peichl (2019) "A drone carried multichannel Synthetic Aperture Radar for advanced buried object detection," in *2019 IEEE Radar Conference (RadarConf)*, pp. 1–6.

[25] Dogaru, T. V., B. Phelan, and C. Kelly (2022) "Analysis of buried target and clutter signature in ground penetrating radar imaging," in *Radar Sensor Technology*

XXVI (K. I. Ranney and A. M. Raynal, eds.), vol. 12108, International Society for Optics and Photonics, SPIE, p. 1210804.
URL `https://doi.org/10.1117/12.2621021`

[26] Kelly, C., T. Dogaru, K. Gallagher, C. Le, B. Phelan, and R. Narayanan (2023) "Clutter and Ambiguity Reduction Using 3-Dimensional Side-Looking Synthetic Aperture Radar," *Progress In Electromagnetics Research B*, **102**, pp. 115–130.

[27] Swenson, G. and Y. Lo (1961) "The University of Illinois radio telescope," *IRE Transactions on Antennas and Propagation*, **9**(1), pp. 9–16.

[28] Andreasen, M. (1962) "Linear arrays with variable interelement spacings," *IRE Transactions on Antennas and Propagation*, **10**(2), pp. 137–143.

[29] Harrington, R. (1961) "Sidelobe reduction by nonuniform element spacing," *IRE Transactions on Antennas and Propagation*, **9**(2), pp. 187–192.

[30] Unz, H. (1956) *Linear Arrays with Arbitrarily Distributed Elements*, *Tech. Rep. series 60, no. 168*, Electronics Research Lab., University of California, Berkeley.

[31] King, D., R. Packard, and R. Thomas (1960) "Unequally-spaced, broad-band antenna arrays," *IRE Transactions on Antennas and Propagation*, **8**(4), pp. 380–384.

[32] Ishimaru, A. (1962) "Theory of unequally-spaced arrays," *IRE Transactions on Antennas and Propagation*, **10**(6), pp. 691–702.

[33] Ishimaru, A. and Y.-S. Chen (1965) "Thinning and broadbanding antenna arrays by unequal spacings," *IEEE Transactions on Antennas and Propagation*, **13**(1), pp. 34–42.

[34] Lo, Y. (1964) "A mathematical theory of antenna arrays with randomly spaced elements," *IEEE Transactions on Antennas and Propagation*, **12**(3), pp. 257–268.

[35] Chow, Y. (1965) "On grating plateaux of nonuniformly spaced arrays," *IEEE Transactions on Antennas and Propagation*, **13**(2), pp. 208–215.

[36] Nguyen, L. and R. Innocenti (2010) "Suppression of sidelobes and noise in airborne SAR imagery using the Recursive Sidelobe Minimization technique," in *2010 IEEE Radar Conference*, pp. 522–525.

[37] Li, D., G. Wei, B. Sun, and X. Wang (2020) "Recursive Sidelobe Minimization Algorithm for Back-Projection Imaging of Impulse-Based Circular Synthetic Aperture Radar," *IEEE Geoscience and Remote Sensing Letters*, **17**(10), pp. 1732–1736.

[38] Richards, M. (2012) *Principles of Modern Radar: Advanced Techniques*, SciTech Publishing, Inc., Raleigh, NC, USA.

[39] ——— (2010) *Principles of Modern Radar, Vol 1: Basic Priniples*, SciTech Publishing, Inc., Raleigh, NC, USA.

[40] Proakis, J. and D. Manolakis (1996) *Digital Signal Processing: Principles, Algorithms, and Applications*, 3rd ed ed., Prentice Hall, Inc., Upper Saddle River, NJ, USA.

[41] Carrara, W. (1995) *Spotlight Synthetic Aperture Radar*, Artech House, Boston, MA, USA.

[42] Dogaru, T. (2022) *Performance Analysis of Side-Looking Ground Penetrating Radar Imaging*, *Tech. Rep. ARL-TR-9388*, Army Research Laboratory, Adelphi, MD, USA.

[43] ——— (2010) *AFDTD user's manual*, *Tech. Rep. ARL-TR-5145*, Army Research Laboratory, Adelphi, MD, USA.

[44] Dogaru, T. and K. Ranney (Awaiting Publication) "Doppler processing with near-field arrays," in *Radar Sensor Technology XXVIII*, vol. 13048, International Society for Optics and Photonics, SPIE, p. tbd.

[45] Griffiths, H. D., C. J. Baker, P. F. Sammartino, and M. Rangaswamy (2009) "MIMO as a Distributed Radar System," in *MIMO Radar Signal Processing* (J. Li and P. Stoica, eds.), chap. 8, John Wiley and Sons, Inc., Hoboken, New Jersey.

Vita

Colin D. Kelly

Education

The Pennsylvania State University University Park, PA
Doctor of Philosophy, Electrical Engineering May 2024
Bachelor of Science, Electrical Engineering December 2016

Academic Research Experience

General Technical Services, LLC Adelphi, MD
Supporting the U.S. Combat Capabilities Development Command Army Research Laboratory
Electronics Engineer September 2018 – January 2019
Electronics Engineer October 2023 – Present

Oak Ridge Associated Universities Adelphi, MD
Supporting the U.S. Combat Capabilities Development Command Army Research Laboratory
Graduate Guest Researcher June 2015 – October 2017
Graduate Guest Researcher October 2020 – October 2023

The Pennsylvania State University University Park, PA
Radar and Communications Laboratory
Research Assistant January 2017 – August 2021